

Abstract of “Electrokinetic Current Driven by a Viscosity Gradient” by Benjamin Wiener, Brown University, May 2019.

Gradients of voltage, pressure, temperature, and salinity can transport objects in micro- and nanofluidic systems by well known mechanisms. Relatively little experimental work has previously been done to explore the behavior of particles in a viscosity gradient. This thesis presents observation, analysis, theory, and simulation of a new nanofluidic transport phenomenon whereby a gradient in liquid viscosity causes an ionic current to flow inside a glass nanofluidic channel.

We studied ionic transport inside nanofluidic devices in which we set up a controlled viscosity gradient by pumping fluids of known viscosity past either end of a channel with no applied voltage, pressure, or salinity gradient. We measured currents on the order of 10 to 100 pA flowing in the direction of lower viscosity through the 200 μm -long and 150 μm -wide channels using fluids with viscosities that varied from 1 to 5 mPa s. The nanofluidic devices enabled us to thoroughly characterize the current’s dependence on experimental parameters like the viscosities of the liquids, the length of the channel, the surface charge density, and the bulk salinity. The currents increased linearly with the gradient of the inverse viscosity and the channel’s surface charge density, but were insensitive to the bulk salinity. We propose a simple model of these viscosity-driven currents in which mobile counterions screening the channels’ surface charge drift with a speed equal to the gradient in their diffusivities. This model describes our data well and explains the microscopic origin of the effect.

Drift in a viscosity gradient is a consequence of multiplicative (state-dependent) noise, which refers to the dependence of a particle’s thermal fluctuations on its position. The mathematical Itô-Stratonovich dilemma arises because one must choose whether the size of each stochastic step corresponds to the viscosity at the beginning of the step (Itô convention), the middle of the step (Stratonovich convention), the end of the step (isothermal convention), or somewhere in between. This seemingly insignificant choice has measurable consequences, as only the isothermal convention explains the existence and direction of the currents we measured. We present simulations which illuminate this surprising fact and show how the drift of ions arises from particles taking larger average steps when they move in the direction of decreasing viscosity.

Electrokinetic Current Driven by a Viscosity Gradient

by

Benjamin Wiener

B. S., Brandeis University, 2011

Sc. M., Brown University, 2014

A dissertation submitted in partial fulfillment of the
requirements for the Degree of Doctor of Philosophy
in the Department of Physics at Brown University

Providence, Rhode Island

May 2019

© Copyright 2019 by Benjamin Wiener

This dissertation by Benjamin Wiener is accepted in its present form by
the Department of Physics as satisfying the dissertation requirement
for the degree of Doctor of Philosophy.

Date _____
Derek Stein, Director

Recommended to the Graduate Council

Date _____
Humphrey Maris, Reader

Date _____
Robert Pelcovits, Reader

Approved by the Graduate Council

Date _____
Andrew G. Campbell
Dean of the Graduate School

Vita

Education

- **Brown University**, Graduate Studies in Physics, Providence, RI
 - Candidate for Doctor of Philosophy, in Physics, January 2019
 - * **Thesis:** *Electrokinetic Current Driven by a Viscosity Gradient*
 - * **Adviser:** Derek Stein
 - Master of Science in Physics, May 2014
- **Brandeis University**, Undergraduate Studies, Waltham, MA
 - Bachelor of Science with Honors in Physics, May 2011
 - * **Honors Thesis:** *Determining the ATLAS muon momentum resolution from Z and high mass Drell-Yan events*
 - * **Adviser:** Craig Blocker

Awards

- Physics Faculty Prize, Brandeis University, May 2011
- First Year Fellowship, Brown University, September 2012
- Chateaubriand Fellowship, Embassy of France in the United States, November 2016

Conference Presentations

- APS March Meeting, March 2015
 - **Contributed Talk:** *Noise and Ionic Conductivity in Glass Nanochannels*
- Flow17 Conference, July 2017
 - **Poster:** *Brownian Motion in a Viscosity Gradient*
- APS March Meeting, March 2018
 - **Contributed Talk:** *Electrokinetic Current Driven by a Viscosity Gradient*

Publications

- Maulbetsch, W., Wiener, B., Poole, W., Bush, J., & Stein, D. (2016). Preserving the sequence of a biopolymer's monomers as they enter an electrospray mass spectrometer. *Physical Review Applied*, 6(5), 054006.
- Bush, J., Maulbetsch, W., Lepoitevin, M., Wiener, B., Mihovilovic Skanata, M., Moon, W., ... & Stein, D. (2017). The nanopore mass spectrometer. *Review of Scientific Instruments*, 88(11), 113307.
- Wiener, B., & Stein, D. (2018). Noise-Driven Drift in a Viscosity Gradient. arXiv preprint arXiv:1807.09106.

Acknowledgements

To my adviser, Derek Stein, thank you for sharing your knowledge and wisdom, for your infectious enthusiasm, and for generously giving your time whenever I asked for it.

To the rest of my thesis committee, Humphrey Maris and Robert Pelcovits, thank you for taking the time to read and consider this work.

To Liz Baessler, thank you for supporting me and believing in me, thank you for moving to Providence with me, and thank you for making my life outside of the lab bright and happy.

To Will Maulbetsch, thank you for being a great labmate and friend. Inside and outside the lab, you were always there to listen and give wise and honest advice.

To my wonderful friends at Brown, Philip Zucker, Declan Oller, Max King, Zoe Weiss, David Tersegno, Bobby Bretz, Jon Kurvits, thank you for filling my life with projects, trips, and games, and for giving me something to look forward to any night of the week.

To my brother, Matt Wiener, thank you for keeping us close while I was at Brown and CERN, for sharing your interests with me, and for taking up some of mine.

To my parents, Wendy Naidich, and Elliot Wiener, thank you for teaching me to enjoy learning and for always supporting me in any way I asked.

To my nanopore mass spectrometer labmates, Mathilde Lepoitevin, Joe Bush, Nick Drachman, Hannah Szapary, and Oliver Isik, thank you for letting me tag along. I greatly valued having a promising secondary project to work on when I was bogged down elsewhere.

To my labmates who taught me skills and helped mentor me when I was new in the lab Daniel Kim, Angus McMullen, Mirna Mihovilovic, thank you for giving me your time and advice.

To my other labmates, Shayan Lame, David Osterman, Kun Li, Bill Brockmueller, George Arauj, Xu Liu, thank you for making the lab and office a warm and fun place to be.

Contents

List of Tables	x
List of Figures	xi
1 Introduction	1
1.1 Electrokinetic phenomena	1
1.2 Applications and micro- and nanofluidics	2
1.3 Brownian motion	4
1.4 Stochastic processes	6
1.5 Previous Experiments	8
1.5.1 Diffusion in diffusivity gradients based on distance from a diffusion-inhibiting surface	8
1.5.2 Diffusion in diffusivity gradients caused by gelatin	10
1.5.3 Simulated diffusion in a viscosity gradient	11
1.6 Outline of the dissertation	13
2 Theoretical and experimental foundations	15
2.1 Theoretical background on Brownian motion and stochastic processes	16
2.1.1 Random walk	16
2.2 Multiplicative noise and the Itô-Stratonovich Dilemma	17
2.3 Connection to Fick's law	19
2.4 Experimental background – Electrokinetics and microfluidics	21
2.4.1 Flow in a pipe or channel	22
2.4.2 Surface chemistry and surface charge of glass	23

2.4.3	Electrophoresis	24
2.4.4	Electro-osmosis	25
2.4.5	Streaming current	26
2.4.6	Generalized forces and flows	27
2.5	Measuring drift in a viscosity gradient using glass nanocapillaries	27
2.5.1	Detecting drift using surface counterions	28
2.5.2	Electrokinetic rectification in glass nanocapillaries	29
2.5.3	Flow rate through glass nanocapillaries	30
2.5.4	Ionic current in a viscosity gradient	31
2.6	Conclusion	32
3	Electrokinetic Current Driven by a Viscosity Gradient	33
3.1	Experimental methods	33
3.1.1	Fabrication of chip-based fluidic devices	35
3.1.2	Fluid flow control system	36
3.2	Making the experimental liquids	37
3.2.1	Controlling conductivity and pH	37
3.2.2	Measuring liquid viscosity	38
3.2.3	Dependence of the viscosity on the composition of the liquid mixtures	39
3.3	Measuring surface charge density of nanofluidic channels	40
3.3.1	Conductance model for rectangular nano- and microscale channels	40
3.4	Width of the boundary layers at the ends of the mixing channel	42
3.5	Measurements of viscosity-driven currents in a nanofluidic channel	44
3.5.1	Typical experiment	44
3.5.2	Equivalent circuit and current forking ratio	45
3.5.3	Dependence of I_v on η_R and η_L	45
3.6	Discussion	47
3.6.1	Deriving a model of I_v	48
3.7	Other sources of current	50
3.7.1	Chemical potential gradient	51
3.7.2	Streaming current	53

3.7.3	Bernoulli effect	53
3.8	Conclusion	54
4	The mechanisms of diffusion in a viscosity gradient	56
4.1	Simulation design	57
4.1.1	Constant diffusivity	58
4.1.2	Diffusivity gradient	59
4.2	Results of simulations with diffusivity gradients	60
4.2.1	Using reflective boundary conditions	60
4.2.2	Using electrode boundary conditions	65
4.3	Mathematical analysis of the toy model	67
4.4	Comparison with experiment	69
4.5	Alternate derivation of $\eta(x)$ and interpretation of drift	72
4.6	Conclusion	75
5	Optical measurements of the drift of quantum dots	77
5.1	Introduction	77
5.2	Feasibility of measuring the drift of quantum dots driven by a viscosity gradient	79
5.2.1	Drift speed compared to diffusion	79
5.2.2	Number of photons expected at the CCD from a single quantum dot	80
5.2.3	Drop-out and blinking	80
5.3	Experimental methods	81
5.4	Number density	82
5.5	Tracking quantum dots and measuring diffusivity	83
5.5.1	Measuring quantum dot diffusivity by tracking individual particles	84
5.5.2	Measuring ensemble quantum dot diffusivity	85
5.6	Conclusion	87
6	Conclusion	89
	Bibliography	91

List of Tables

List of Figures

1.1	An illustration of a simplified DNA restriction mapping experiment using electrophoresis. a) The whole molecule moves a short distance. b) The molecule is cut in one place. The pieces move farther because they are smaller. c) The molecule is cut in a different place. The short piece moves farther. d) The molecule is cut in three places. Gel electrophoresis example image from a Washington University teaching lab [1].	3
1.2	Miniature gas chromatograph on a wafer. a) Carrier gas inlet. b) Sample gas inlet and outlet. c) Sample injection valve. d) 1.5 m separating column. e) Detector channel. f) Gas outlet. Image from James B. Angell <i>et. al.</i> [2].	5
1.3	Illustration of the coin-flip random walk. The walker holds a red flag for visibility. a) Close up, individual steps are discernible. b) Far away, only the motion resulting from multiple steps in the same direction can be seen.	6
1.4	a) A diagram of a particle of radius r diffusing a distance z from a surface. b) Diffusivity in units of bulk diffusivity as a function of distance from the solid surface in units of particle radii (blue). The gradient of the diffusivity in units of bulk diffusivity as a function of distance from the solid surface in units of particle radii (orange).	9
1.5	Cross-section of the cell showing the colloidal suspension confined between the spherical lens and the flat disk, separated by an elastic O-ring. The left view shows an enlargement of the center of the cell with the circular excluded volume and the observation frame ($65 \times 100 \mu\text{m}^2$). The round inset explains the two contributions to the change in diffusion coefficient when a particle moves a distance dx . Image and caption by Lançon <i>et al.</i> [3].	9

1.6	The top half shows the five experiments, consisting of flat vessels on a glass plate that were scanned on a flatbed scanner. Image scanned about 8 h after the start of the experiment. Note the sharp colour intensity difference between the top and the bottom half in experiments B and D, where the bottom half has a lower diffusion rate than the top half (the x-coordinate referred to in the text is upward in this picture). The colour intensity boundary is blurred in experiments C and E, where concentrations were different at the start of the experiment, but diffusion rates the same in top and bottom half. Bottom image series shows experiment D at different time intervals, showing the progressive diffusion of food colouring towards the slow diffusion gelatinous bottom half. Image and caption by van Milligen <i>et al.</i> [4].	10
1.7	a) A polymer straddles a nanopore separating two regions with different viscosities. b) Using overdamped Brownian dynamics, the polymer tends to move toward the side with higher viscosity. Using full Langevin dynamics, where momentum is included, the polymer tends to move toward the lower viscosity side. Image by deHaan and Slater.	12
2.1	Stochastic displacement models. Illustrations show leftward and rightward steps of random walks corresponding to (a) the Itô, (b) the Stratonovich rule, and (c) the isothermal rule.	22
2.2	Poiseuille flow in a wide channel.	23
2.3	Glass surface schematic. a) Chemical diagram of an ideal glass surface. Before dissociation, terminal silanol groups are protonated. When the pH of the solution is high, protons are in low concentration. Many protons dissociate from the glass surface, leading to a highly charged surface. When the pH is low, fewer protons dissociate, leaving a less charged solution. b) A cloud of positive counterions screening a negatively charged glass surface. Plotted line shows the electric potential, $\phi(x)$. This equilibrium is a balance between electrostatic forces drawing counterions toward the surface and thermal energy.	24

2.4	a) An electric field drives the electrophoretic motion of charged particles in a channel. The charged particles exert a viscous force on the fluid and cause electro-osmotic flow.	
	b) Hydrostatic pressure pushes fluid through a channel. The flow carries charged particles in the EDL, causing a streaming current.	25
2.5	Pulled glass nanocapillaries. a) The method used by the Sutter P-97 Micropipette Puller. b) A composite microscope image of a nanocapillary. c) An scanning electron microscope image of the opening of a nanocapillary	28
2.6	a) The tip of a glass nanocapillary inside a liquid with lower viscosity. Positive ions screen the negatively charged surfaces. An ammeter detects and new motion of ions.	
	b) Measured current plotted against glycerol fraction from a capillary experiment.	29
2.7	a) Current normalized by bulk conductivity plotted against applied voltage. b) When a positive voltage is applied inside the capillary, the tip is partially depleted of positive ions, decreasing the overall conductance. c) When a negative voltage is applied inside the capillary, the tip the concentration of positive ions inside the tip is enhanced, increasing the overall conductance.	30
2.8	The flow rate per unit pressure as a function of capillary inner diameter. Inset shows the bubble used to measure the flow rate of one device. The yellow line shows the truncated cone model. The less successful tube model will not be discussed here.	31
3.1	(a) Sketch of the mixing channel cross section showing counterions drifting in the direction of lower viscosity. (b) 3D sketch of the nanofluidic chip indicating w and L . The equivalent circuit diagram shows how I_v , modeled as a current source, is related to I_m , R_m , $R_{\mu L}$, and $R_{\mu R}$	34
3.2	Chip fabrication. The masks used to expose the microchannels for chips with a) 100 and b) 400 μm long nanochannels. The masks used to expose the c) 50 and d) 150 μm wide nanochannel. e) A 3D rendering of the finished chip.	35
3.3	Exploded view of chuck. Shows the chip, which (when assembled) is sealed to the chuck with o-rings and fastened to the chuck with an aluminum bracket and screws.	36
3.4	The conductivity of a solution of 50% water, 25% glycerol, 25% formamide with 100 mM KCl over time. Line shows best fit of an exponential function, equation 3.1.	38

3.5	Dependence of the viscosity of a mixture of two liquids on the volume fraction of the higher-viscosity component. Symbols show measured viscosity of a mixture containing 50 % water, $\phi_g \times 50$ % glycerol, and $(1 - \phi_g) \times 50$ % formamide. The solid line shows eq. 3.20, where $\eta_f = 1.11$ mPa s and $\eta_g = 5.96$ mPa s.	39
3.6	Measured current as a function of bulk solution conductivity. Red dashed lines show expected contributions from bulk ions, equation 3.6. Green dashed line shows expected contributions from ions screening the surfaces, equation 3.13.	42
3.7	Sketch of the mixing region extending into a microchannel.	43
3.8	Measuring viscophoresis in nanofluidic channels. Traces of (a) I_v and (b) η_L (orange dashed) and η_R (blue) from a typical viscophoresis measurement.	44
3.9	a) Equivalent circuit representing the experimental device. The viscosity gradient induced drift is treated as a constant current source. This current can fork back through the mixing channel or through the ammeter via the micro-channels. b) The time evolution of the ratio of I_m/I_v assuming bulk conductivity evolves as shown in figure 3.4a, according to the models in section 3.3.1	45
3.10	Experimental characteristics of viscophoresis. (a) Dependence of I_v on η_R for $\eta_L = 1.1$ (purple triangles), 1.5 (blue squares), 2.2 (red circles), and 3.4 mPa s (green diamonds) in a $L = 200$ μm channel. Lines show equation 3.29 with $\sigma = 200$ mC m ⁻² . (b) Dependence of $I_v \eta_L$ on η_R/η_L for the same measurements. Line shows equation 3.29 rescaled by η_L	46
3.11	The dependence of I_v on η_R is compared a) between channels with $L = 100$ (red circles) and 400 μm (blue squares); b) between measurements at pH 8 (red circles) and pH 5 (blue squares) in a single $L = 100$ μm channel; and c) between measurements at bulk KCl concentrations of 100 mM (red circles) and 500 mM (blue squares) in the same $L = 100$ μm channel. In all cases $\eta_L = 2.6$ mPa s and the lines show fits of equation 3.29 to the data, which obtained a) $\sigma = 400$ mC m ⁻² , b) $\sigma = 280$ mC m ⁻² for pH 8 and $\sigma = 50$ mC m ⁻² for pH 5, and c) $\sigma = 250$ mC m ⁻² . d) Dependence $I_v \eta_L L$ on η_R/η_L for measurements performed at pH 8 using various L and KCl concentrations, as indicated. The line shows equation 3.29 rescaled by $\eta_L L$ with $\sigma = 200$ mC m ⁻² . The experimental uncertainty in these figures is comparable to the size of the symbols. 46	

4.1	Simulated diffusion of 10^5 particles with reflective boundary conditions and spatially-constant diffusivity. a) Five sample particle trajectories. b) The distribution of particles after 10, 100, and 1000 time steps. Dashed lines show theoretical expectation according to equation 4.5.	58
4.2	a) A particle hopping into a reflective boundary condition. b) A particle hopping into a boundary condition designed to emulate an electrode.	61
4.3	Simulated diffusion of 10^5 particles with reflective boundary conditions using different integration conventions. Evolution of the particle distribution using a) the Itô convention and b) the isothermal convention. c) Diffusivity as a function of x	61
4.4	Evolution of the random walker with multiplicative noise for various values of α . (a) For $\alpha = 0$, the amplitude of each random step is a function of the initial state and is therefore symmetrically distributed; (b) example of a trajectory in state space; (c) probability density of the distributions at selected times. The corresponding results for $\alpha = 0.5$ and $\alpha = 1$ are shown in ((d)–(f)) and ((g)–(i)), respectively. In all cases, reflecting boundary conditions are imposed at $x = 0$ and $x = 100$. Note that the steady-state probability distribution is uniform only in the $\alpha = 1$ case, while in the other two cases it is peaked in the low-noise (small $\sigma(x)$) region. The steady-state probability distributions are calculated from 100 000 simulated trajectories. Figure and caption by Volpe and Wehr [5].	62
4.5	Simulated equilibrium particle densities in the a) Itô convention and b) isothermal convention. Dotted lines show the farthest positions, x_+ and x_- , from which particles can cross a test point, x' , from the left and right respectively. The areas of the shaded regions below the curve are proportional to the approximate number of particles that can cross x' from the left (orange) and the right (blue) in one step.	63

4.6	Simulated equilibrium particle density in the isothermal convention with electrode boundary conditions. a) Dotted lines show farthest positions from which particles can reach or cross a test point, x' , from the left and right. The areas of the shaded regions are proportional to the number of particles that can reach or cross x' from the left (orange) or right (blue) in one step. b) Dotted lines show the farthest positions from which particles can reach or cross the boundaries at $L = 0$ and $L = 100$. Area of the shaded regions is proportional the number of particles with a chance to hit the boundary at $x = 0$ (orange) or $x = 100$ (blue) in one step.	65
4.7	Simulated diffusion of 10^5 particles with electrode boundary conditions using the isothermal convention. a) Evolution of the particle distribution. b) Diffusivity as a function of x	66
4.8	a) Simulated distribution of 10^5 particles relaxing from peaked distribution to steady state distribution using the isothermal convention and electrode boundary conditions. Dashed line shows	69
4.9	a) The evolution of an initially flat particle distribution with the isothermal rule and electrode boundary conditions. b) The fractional absolute difference in flux at the center and at the boundaries for simulations with domain sizes of 100 and 200. . . .	70
4.10	Flux in simulations with several diffusivity ratios using the isothermal rule and electrode boundary conditions. a) Dependence of flux on $D(x = L)^{-1}$. b) Diffusivity profiles, color coded to match points in (a).	71
4.11	Flux in simulations with several domain lengths using the isothermal rule and electrode boundary conditions. a) Dependence of flux on L . b) Diffusivity profiles, color coded to match points in (a).	71
5.1	An illustration of a fluorescing quantum dot, imaged by a microscope drifting in a liquid viscosity gradient.	78
5.2	Quantum dots in a droplet of water. a) 8 nM, b) 8 pM.	82
5.3	a) A frame of video with a single quantum dot identified and circled. Red line shows the particle's trajectory. b) The mean squared displacement as a function of lag time. Red line shows is a power law fit.	83

5.4	a) A frame of video with quantum dots identified and circled. b) The ensemble mean squared displacement as a function of lag time. The blue line shows is a power law fit. Points in blue are included in the fit.	84
5.5	Frames from a video of fluorescing quantum dots in a glass chip. Before frame 1, a fluid flow pressed the dots against an electrostatic boundary at $x = 0$ a) The fluid flow is turned off and the dots can freely diffuse. They start in a sharply peaked distribution at $x = 0$. The red line shows the average pixel brightness. The green line shows equation 5.12 b) and c) The dots relax into a wider distribution. d) The brightness as a function of position for several different frames. e) The brightness as a function of position predicted by equation 5.12.	86

Chapter 1

Introduction

In this thesis, we present the measurement, theory, and analysis of a new nanofluidic transport process: ionic current driven by a gradient of liquid viscosity. The main set of experiments we will discuss are straightforward in concept. Inside a fluidic channel, we allowed two liquids of different viscosities to interdiffuse, creating a viscosity gradient. Then, we electrically measured the movement of ions in the channel as an electric current. Our experiment, conducted in a nanofluidic environment, relied on electrokinetic effects that are dominant at tiny scales. The theory we used to analyze and explain our data is based on a simple model of random motion which incorporates some concepts from stochastic calculus. Here, we will provide basic information about these topics, as well as some historical context.

1.1 Electrokinetic phenomena

Electrokinetics refers to a set of phenomena that occur in liquids near charged surfaces. In 1809, the German scientist Ferdinand Friedrich Reuss observed the first electrokinetic phenomena. Using a silver-zinc battery, he applied an electric potential to a U-shaped tube that contained a clay plug [6, 7]. The migration of tiny clay particles he noticed constituted the first recorded instance of what we now call *electrophoresis*, the electric-field-driven motion of a charged particle through a liquid. It was clear to Reuss that the clay particles carried charge, though he did not know the origin of that charge. He also noticed that the level of the water rose on one side of the tube in response to the battery. We now know this to be caused by a closely-related electrokinetic effect

called *electro-osmosis*, the motion of fluid dragged by electrophoresing charged particles.

Half a century later, in 1859, the physicist Georg Quincke performed the reverse experiment, pushing liquid through a tube and measuring the resulting electric current [8, 7]. This effect, the development of an electric current by charges being advected by fluid flow, is now called *streaming current* and is known to originate in charges on surfaces.

The symmetrical relationship where ionic current can cause electro-osmotic fluid flow and fluid flow can cause electrical streaming current did not escape Uno Saxén, a Finnish student studying electrokinetics in the late 1880s. The reciprocal relationships he identified, caused by viscous coupling between the fluid and charge carrying ions, are now referred to as Saxén's laws [9, 7]. Today, these are seen as a special case of the Onsager reciprocal relations, which more generally require equality between related cross terms connecting generalized forces to disparate generalized flows [10, 7]. Work on this topic, performed here at Brown University, earned Lars Onsager the Nobel Prize in Chemistry in 1968 [11].

Electrophoresis, electro-osmosis, and streaming current are sometimes called the classical electrokinetic effects [7]. More recently, others have been discovered. In 1947 Boris Derjaguin observed *diffusiophoresis*, the motion of colloidal particles in response to the concentration gradient of an electrolyte [12, 7]. *Thermophoresis*, also known as the *Soret effect*, is an older but less well-understood phenomenon which under most conditions results in particles fleeing areas with higher temperature as higher thermal energy causes less effective chemical solvation [13].

In this thesis, we will describe and analyze currents measured in fluidic channels where there was no gradient in electric potential, no gradient in pressure, no gradient in solute concentration, and no gradient in temperature, only a gradient in liquid viscosity. Compared to the other electrokinetic effects described above, relatively little experimental work has previously been done to explore the behavior of particles in a viscosity gradient.

1.2 Applications and micro- and nanofluidics

Of all the electrokinetic effects, electrophoresis is the best known because of its many technological applications. The 1948 Nobel prize in chemistry was awarded to Arne Tiselius for his work analyzing proteins using electrophoresis [11]. Today, it famously plays a central role in gel electrophoresis, a technique used for analyzing DNA and other charged particles. A mixture of particles to be analyzed

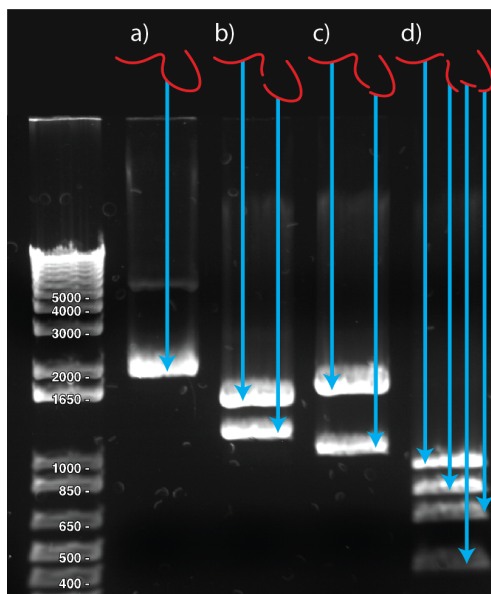


Figure 1.1: An illustration of a simplified DNA restriction mapping experiment using electrophoresis. a) The whole molecule moves a short distance. b) The molecule is cut in one place. The pieces move farther because they are smaller. c) The molecule is cut in a different place. The short piece moves farther. d) The molecule is cut in three places. Gel electrophoresis example image from a Washington University teaching lab [1].

is loaded into a viscous medium. Often a gel is used, among other reasons, to prevent advection like that caused by diffusio-osmosis [7]. In its simplest form, the particles are subjected to an electric field which causes them to migrate at a speed determined by their charge and shape, though the picture gets more complicated for polymers like DNA. Over time, the particles migrate at different speeds and separate into bands. The particles are then visualized with a dye, for example, so that the bands can be analyzed.

In one application called DNA restriction mapping, one can create a DNA fingerprint useful for determining if two samples of DNA are likely to have contained the same sequence. Molecules called restriction enzymes break DNA in particular places. Different mixtures of these enzymes are used on samples of the DNA, creating sets of fragments that depend on the specific sequence of the polymer [14]. When analyzed using gel electrophoresis, different DNA sequences will result in different characteristic patterns of bands. Figure 1.1 illustrates this for three different restriction enzymes which cut the same example DNA sequence in different places. In figure 1.1a, the strand is unbroken and travels the least distance of all. In figures 1.1b and 1.1c, the DNA is cut by the enzyme in one place. In figure 1.1d, the DNA is cut in four places. In all cases, the smaller fragments

travel farther.

Many more applications of electrokinetics exist in micro- and nanofluidic systems. In a 1959 speech at Caltech, Richard Feynman famously declared “there is plenty of room at the bottom” [15]. He was poetically expressing his belief that the micro- and nanoscale world held great potential for science and technology. Feynman was right. Today, nanoscale technologies are commonplace. One example is MEMS (microelectromechanical systems), tiny machines with a wide variety of uses from measuring acceleration to harvesting energy. Microfluidic chips, fluidic systems with micrometer-sized linear dimensions, are another example of the opportunities available at small scales. In these chips, carefully designed channels and other structures are cut into silicon or glass. In the 1970s an early microfluidic system was developed, shown in figure 1.2 [16]. This miniaturized gas chromatography system was integrated into a five centimeter wide wafer and included a spiral-shaped 1.5 m long column along with micro-scale controls and detector [2, 16]. Lab-on-a-chip instruments like this have been able to achieve high resolution while requiring very small samples [17]. Soon, pumps, mixers, sensors, and filters could all be found in tiny fluidic chips. At tiny scales, pressure driven flow can be impractical, due to its strong dependence on channel size, so other mechanisms like electro-osmosis can be used as a micro-scale pump [16]. In similar systems, streaming current can be used a means to harvest energy by turning fluid flow into electricity [18]. It took until the 1990s for a microfluidic system to achieve wide commercial success when the inkjet print head, which uses a MEMS to create a tiny fluid jet, was developed [16]. More recently, nanofluidics extended this technology to a still smaller length scale [19].

1.3 Brownian motion

The smaller the length scales, the more important the fundamental thermal motion of particles becomes. This apparently random motion of small particles in a fluid is called Brownian motion. The name comes from its discoverer, Robert Brown, a botanist who in 1827 noticed the inexplicable motion of pollen on the surface of a liquid [20]. Brown naturally assumed a living organism must be behind the motion. However, tests on lifeless systems, as well as the fact that the motion did not slow down or stop over time, forced him to conclude that the origin of the motion was not living [21]. By the middle of 19th century, a connection between Brownian motion and temperature had been established, and theories were being developed to explain the connection. Still, by the turn of the

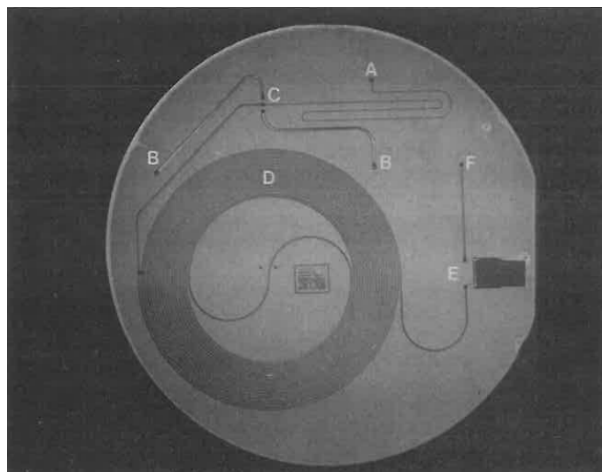


Figure 1.2: Miniature gas chromatograph on a wafer. a) Carrier gas inlet. b) Sample gas inlet and outlet. c) Sample injection valve. d) 1.5 m separating column. e) Detector channel. f) Gas outlet. Image from James B. Angell *et. al.* [2].

century, the theory that all matter is made up of small discrete particles and that theory's connection to Brownian motion were not universally accepted in the scientific community [21]. Existing related theories, like those surrounding the ideal gas law, hinted at the atomic nature of matter, but did not constrain the size of these particles. Moreover, how tiny particles would be capable of causing visible motion of much larger particles was a mystery. In 1905, Einstein proposed a solution: that even tiny random bumps from interactions with fluid particles can occasionally combine to produce noticeable displacements. Within a few years, experiments had confirmed his intuition [22, 23].

The simple analogy of a random walk helps explain how this is possible and will be a useful starting point for the more complicated models to come [21]. Imagine playing a game where you repeatedly flip a fair coin. With every 'heads' you take one step to the right and with every 'tails' you take one step to the left. After two coin flips, there are even odds that you are at your starting position. Figure 1.3a shows the potential results of these two coin flips.

Now, say a friend watches you play this game from far away. Because of the distance, the friend cannot tell which direction you move in each individual step. After the two coin flips, they can detect no movement. After one thousand coin flips, the chance that you are exactly where you started is small, about 2.5%, because it is difficult to flip exactly five hundred heads and five hundred tails. More importantly, there is a 73% chance that you are more than ten steps from your starting point. Your friend can likely notice your movement. Figure 1.3b shows an example of a one thousand flip

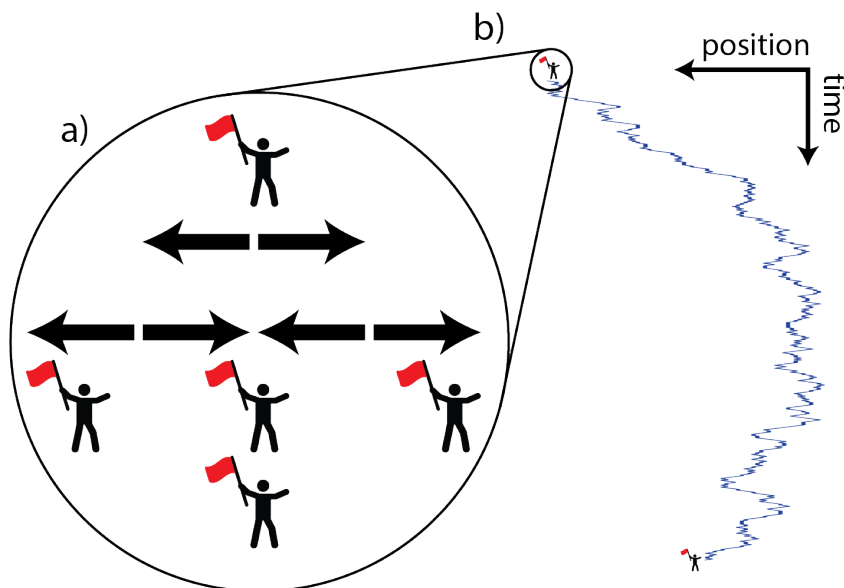


Figure 1.3: Illustration of the coin-flip random walk. The walker holds a red flag for visibility. a) Close up, individual steps are discernible. b) Far away, only the motion resulting from multiple steps in the same direction can be seen.

path where individual steps are not visible, but overall motion is obvious. After one million flips, the chance that you are exactly at your starting point is infinitesimal and you are almost certain ($> 99\%$) to be more than ten steps from the starting point. This game shows how many unobservable and uncorrelated interactions can add up to significant motion.

In addition to establishing the molecular nature of matter and explaining Brownian motion, Einstein's 1905 paper also recognized the fundamental connection between viscous drag and random diffusive motion [24, 25]. The same random bumps that cause Brownian motion also randomize the motion of a drifting particle and eventually bring it to rest. For a particle in a fluid, this connects the diffusivity of that particle with the viscosity of the fluid. This connection is an early example of a more general concept called the *fluctuation-dissipation theorem*, which relates random behavior with dissipation in some systems.

1.4 Stochastic processes

In 1923, Norbert Wiener proved that it was possible to formulate a rigorous continuous time version of the random walk, now called the *Wiener process* [26, 27]. The Wiener process is a collection of

random variables that can be viewed as a rescaled small-step limit of the random walk [27]. Wiener's work is the basis for many ideas in the field of stochastic processes. Beyond describing Brownian motion, it is used in mathematical finance to develop the Black-Scholes model for pricing options, among other things [28]. The Wiener process exhibits the interesting property of self-similarity [29]. Zooming in on a Wiener process with the right scaling reveals another Wiener process. The random bumpiness does not disappear on any scale.

In the 1940s and early '50s, the Japanese mathematician Kiyosi Itô invented a method for integrating stochastic processes like the Wiener process [30, 26]. He generalized the well known Riemann-Stieltjes integral, where one divides a function into tiny intervals and sums the area under the curve based on the value of the function in each interval. A smooth function can be sampled anywhere within the interval because the possible choices all converge to the same value in the limit of small intervals. However, because Brownian motion is not smooth at any scale, no matter how small the interval, the integral depends on the arbitrary choice of where within each interval one evaluates the function. Itô's integral sums the value of the function evaluated at the beginning of each interval [5, 31].

Later, others like Ruslan Stratonovich, Donald Fisk, and Peter Hänggi developed alternatives to Itô's integral, each giving a different but completely self-consistent formulation of stochastic calculus. The Stratonovich integral evaluates the function in the middle of each interval and preserves the chain rule of ordinary calculus, while the isothermal (or Hänggi) integral evaluates the function at the end of each interval.

The differences between the integration conventions are physically meaningful in the case of a Brownian particle moving in a gradient of liquid viscosity where that particle's stochastic step size depends on its viscosity, and hence on its location. A particle will exhibit no average drift in a viscosity gradient if it obeys Itô's calculus, since its steps will have the same size regardless of the direction. If it evolves according to the isothermal convention, it will drift toward lower viscosity as it takes larger average steps in that direction [5].

Recent theoretical work by Hänggi, Lubensky, and others, recognizes that there is actually a continuum of different formulations of stochastic calculus, depending on the position, inside each of the integral's intervals where the function is evaluated.

From another perspective, the question of integration convention boils down to how one should generalize Fick's Law of diffusion, $J = -D\nabla P(x)$, in cases where a particle's diffusivity, D , varies

in space [32]. One option, sometimes called the *Fokker-Planck* generalization, is to put the gradient operator outside the diffusivity and write $J = -\nabla(D(x)P(x))$. This results in an explicit flux term proportional to the diffusivity gradient, $J = -P(x)\nabla D(x)$. Another, the *Fick* generalization, is to leave the gradient operator inside the diffusivity and write $J = -D(x)\nabla P(x)$. This results in no explicit flux dependence on the diffusivity gradient. In chapter 2, we will show that the former option connects to the Itô convention, while the latter connects to the isothermal.

Regardless of which perspective we take, it is important to know which law governs a given system. Do particles in a liquid viscosity gradient drift? If so, which direction do they drift? These questions can be addressed experimentally and could have important consequences.

1.5 Previous Experiments

1.5.1 Diffusion in diffusivity gradients based on distance from a diffusion-inhibiting surface

A few experiments have attempted to measure the effect of a viscosity gradient on the motion of a diffusing particle and resolve the ambiguities discussed above. Some of these experiments have used creative mechanisms to create an effective viscosity gradient. Particles diffusing in the vicinity of solid surfaces are known to exhibit lower diffusivity due to hydrodynamic coupling with the surface [33, 34, 35]. Figure 1.4a shows a particle with radius r , diffusing a distance z from the surface. The blue curve in figure 1.4b shows a model for the diffusivity as a fraction of bulk diffusivity plotted against the distance from the wall in terms of particle radii [34, 35]. This function increases steeply, and once the particle is a few radii away from the surface, the function flattens out as $D(x) \approx D_b$. Because the diffusion stifling effect decreases with the distance from the surface, there is an effective diffusivity gradient normal to the surface for any particle diffusing nearby. The range of this effect is limited to a few radii of the diffusing particle. The orange curve in figure 1.4 shows the gradient in the diffusivity as a fraction of the bulk diffusivity, which is already nearly flat at $z \approx r$.

A couple of experiments have used this effect to measure the diffusivity-gradient induced drift of colloidal particles [36, 3, 4]. One such experiment, performed by Lançon *et al.*, optically observed the motion of colloidal particles in a wedge-shaped fluidic domain defined by a curved glass lens pressed against a flat disk [3]. Figure 1.5 shows their experimental setup. Areas near the point

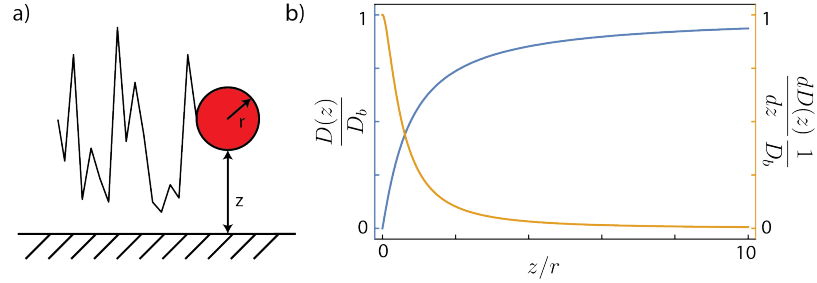


Figure 1.4: a) A diagram of a particle of radius r diffusing a distance z from a surface. b) Diffusivity in units of bulk diffusivity as a function of distance from the solid surface in units of particle radii (blue). The gradient of the diffusivity in units of bulk diffusivity as a function of distance from the solid surface in units of particle radii (orange).

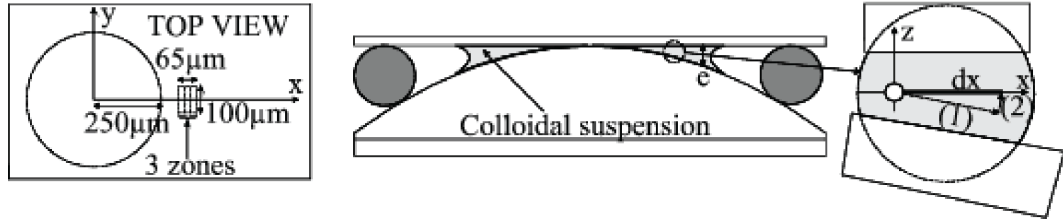


Figure 1.5: Cross-section of the cell showing the colloidal suspension confined between the spherical lens and the flat disk, separated by an elastic O-ring. The left view shows an enlargement of the center of the cell with the circular excluded volume and the observation frame ($65 \times 100\mu\text{m}^2$). The round inset explains the two contributions to the change in diffusion coefficient when a particle moves a distance dx . Image and caption by Lançon *et al.* [3].

of the wedge region are closer to surfaces on average, and particles there tend to experience lower diffusivity. This means there is an effective diffusivity gradient away from the point of the wedge, or away from the center when viewed from above. The group tracked the motion of $1\mu\text{m}$ polystyrene beads in the plane parallel to the flat disk with an optical microscope and measured radial outward drift along the effective viscosity gradient, but a flux-less and uniform particle distribution in steady state. These results were consistent with the isothermal integration convention.

In a comment, Bławdziewicz and Bhattacharya [37] questioned the origin of the flux measured in the experiment by Lançon *et al* [3]. They contended that the drift of the particles could be explained by an entropic effect caused by the increased confinement of the particles near the point of the wedge-shaped region.

Volpe *et al.* performed a different experiment that also used the diffusivity suppressing effect of nearby surfaces. They measured diffusion of colloidal particles in the dimension normal to a glass surface and parallel to gravity. Near the surface, there was an effective diffusivity gradient

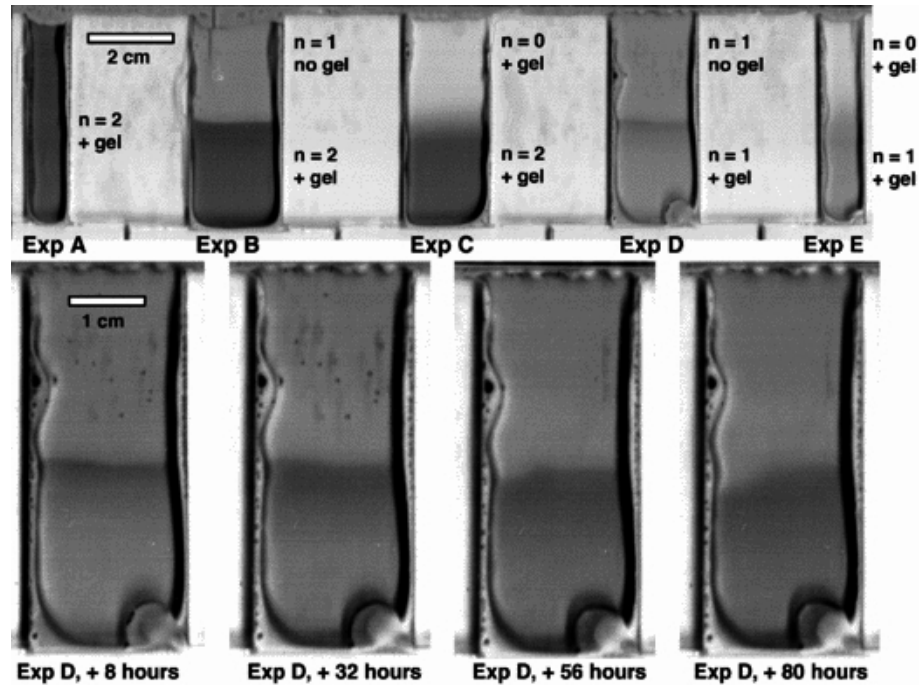


Figure 1.6: The top half shows the five experiments, consisting of flat vessels on a glass plate that were scanned on a flatbed scanner. Image scanned about 8 h after the start of the experiment. Note the sharp colour intensity difference between the top and the bottom half in experiments B and D, where the bottom half has a lower diffusion rate than the top half (the x-coordinate referred to in the text is upward in this picture). The colour intensity boundary is blurred in experiments C and E, where concentrations were different at the start of the experiment, but diffusion rates the same in top and bottom half. Bottom image series shows experiment D at different time intervals, showing the progressive diffusion of food colouring towards the slow diffusion gelatinous bottom half. Image and caption by van Milligen *et al.* [4].

which competed with gravity, while away from the surface, only gravity acted. Using total internal reflection microscopy (TIRM), a technique which relies on the evanescent field near a reflecting interface to accurately measure an object's distance from that interface, the group was able to detect the spurious drift created by the diffusivity gradient by comparing the measured particle distribution with the distribution expected for gravity alone. The results of Volpe *et al.* are also consistent with the isothermal integration rule.

1.5.2 Diffusion in diffusivity gradients caused by gelatin

Van Milligen *et al.* performed an experiment using gelatin to control viscosity and food coloring to visualize particle concentration [4]. They filled a centimeter-scale vessels with liquids containing different concentrations of both gelatin and food coloring, and measured the distribution of food

coloring over time using a flatbed scanner. Figure 1.6 shows some of these experiments, labeled with their starting conditions. Here, $n = 0$ means no food coloring, $n = 1$ means 1 mL L^{-1} , and $n = 2$ means 2 mL L^{-1} .

In their main trial, where initially uniform food coloring distribution straddled a step function diffusivity profile (Exp D in figure 1.6), van Milligen’s group saw a peak develop on the low diffusivity (gelatinous) side [4]. This group did not approach the problem from the perspective of stochastic calculus, and did not comment on integration convention. However, their analysis suggested that the evolution of the concentration profiles in their experiment were more consistent with the *Fokker-Planck* generalization of Fick’s law, since the Fick generalization predicts no flux when the concentration is constant [4]. This experiment is therefore consistent with the Itô convention.

1.5.3 Simulated diffusion in a viscosity gradient

A paper by Hendrick de Haan and Gary Slater [38] inspired us to take on this topic. They simulated a polymer which initially straddles a nano-scale hole called a nanopore, which separates two regions with different viscosities. Figure 1.7a shows the initial conditions, with half of the polymer on the cis side of the pore, and half on the trans side.

They used two different stochastic simulation techniques. One was a full Langevin dynamics simulation, where particles move according to the equation

$$m\ddot{\vec{r}} = -\nabla U(\vec{r}) - \zeta(\vec{r})\vec{v} + \vec{R}(t), \quad (1.1)$$

where \vec{r} is the particle’s position, $U(\vec{r})$ is the sum of any conservative potential function, ζ is a drag coefficient related to the viscosity by $\zeta = 6\pi\eta a$, a is the particle’s radius, and $\vec{R}(t)$ is a random force which represents interactions with the solvent molecule. In the full Langevin dynamics simulation, the molecule was found to preferentially drift toward the low viscosity side of the pore.

The second simulation used an overdamped form of the Langevin equation,

$$\zeta(\vec{r})\vec{v} = -\nabla U(\vec{r}) - \vec{R}(t). \quad (1.2)$$

Here, momentum is ignored and the velocity of each particle is set randomly for each step, with no correlation between steps.

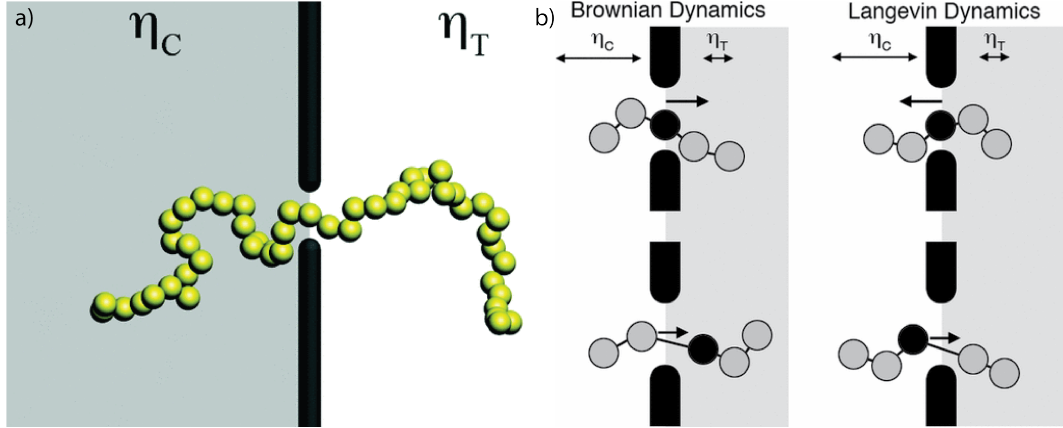


Figure 1.7: a) A polymer straddles a nanopore separating two regions with different viscosities. b) Using overdamped Brownian dynamics, the polymer tends to move toward the side with higher viscosity. Using full Langevin dynamics, where momentum is included, the polymer tends to move toward the lower viscosity side. Image by deHaan and Slater.

De Haan discussed the connection between these two simulation schemes and the Itô-Stratonovich dilemma. In the overdamped equation, each step a particle takes depends on the initial value of $\zeta(\vec{r})$.

$$d\vec{r} = \vec{v}dt = -\frac{\nabla U(\vec{r})}{\zeta(\vec{r})}dt - \frac{\vec{R}(t)}{\zeta(\vec{r})}dt. \quad (1.3)$$

This corresponds to the Itô integration rule, since the increment in position only depends on the state before the jump.

To see how the full Langevin equation fits in, consider a step that starts at position \vec{r} and time t , and ends at \vec{r}' and time t' , caused by a random force $\vec{R}(t)$. For equation 1.1, the motion caused by $\vec{R}(t)$ will partially be determined by the viscosity there, $\zeta(\vec{r})$. However, because of inertia, some of the effect of that force will be retained in the next step, which starts at \vec{r}' . Thus, some of the motion from the original force at \vec{r} will be determined by $\zeta(\vec{r}')$, the end point of the original jump. Because the effects of $\vec{R}(t)$ are determined partially by the starting position, \vec{r} , and partially by the ending position, \vec{r}' , the full Langevin equation simulates something more like the Stratonovich rule or even the isothermal rule, depending on the strength of the inertia effect which is set by ζ/m .

These simulations introduced us to the potentially measurable consequences of diffusion in a viscosity gradient. They also sparked the idea that we could use nanopores as a tool to measure the effects of a viscosity gradient on a diffusing particle.

1.6 Outline of the dissertation

This work is broken into six chapters.

In the second chapter, we discuss the theoretical background for diffusion in a medium where the viscosity can change as a function of position. We present a simple random walk model of homogeneous diffusion. Next, we discuss the main complication that stems from allowing viscosity to vary with position: that the size of each step in a random walk depends on the local viscosity, which itself varies over the length of the step. We connect this to the Itô-Stratonovich dilemma of stochastic calculus. We explain some essential and basic electrokinetic phenomena and related experimental methods. Finally, we discuss an early but flawed experiment we performed to measure electrokinetic current driven by a viscosity gradient.

In the third chapter we report the discovery, experimental characterization, and theoretical analysis of a transport effect driven by viscosity gradients, which cause an ionic current to flow inside a glass nanofluidic channel. Measurements of the current are well described by a simple model wherein counterions in the electric double layers near the surfaces drift in the direction of decreasing viscosity with a drift speed equal to the gradient of the ions' local diffusivity. Drift in a viscosity gradient is a consequence of multiplicative (state-dependent) noise, which results from a particle's thermal fluctuations depending on its position. This surprisingly large effect, measured in a highly controlled nanofluidic environment, reveals fundamental behavior that is relevant to a broad range of systems.

In the fourth chapter, we discuss the physical mechanisms of diffusion in a viscosity gradient. First, we use simulations to show how the different stochastic rules used to integrate random motion affect the steady state particle distribution in a diffusivity gradient. Importantly, we illuminate the role that the boundary conditions play, disallowing steady-state flux when the boundary conditions mimic those of a closed container, and allowing flux when they mimic electrodes. We connect the results of the simulations back to our experiments. Finally, we discuss an alternate interpretation of the ionic currents we measured in our experiments.

In the fifth chapter, we present work toward a new experiment for optically measuring particles diffusing in a gradient of liquid viscosity. We introduce quantum dots into a nanofluidic chip like the ones discussed in chapter 3, measure their time-dependent paths, and deduce their diffusivities from these paths. We discuss factors that have prevented us from proceeding with this experiment.

This experiment would allow us both to measure the viscosity profile by measuring diffusivities at different points in the channel and to detect any drift caused by a viscosity gradient.

The sixth and final chapter is a conclusion.

Chapter 2

Theoretical and experimental foundations

The viscosity of a liquid and the diffusivity of a particle within it are fundamentally related because both are manifestations of the microscopic interactions between the particle and the liquid's molecules [24, 39]. Because it is impractical to know the details of these innumerable interactions, one commonly models them in aggregate as noise, and the Brownian motion as a random process whose scale is set by the noise magnitude. Thus, when a liquid's viscosity varies with position, so does the noise magnitude and the step size of a particle's random walk. As we will show, the physical model is incomplete until one specifies the rule for adding up the random steps. A mathematical ambiguity, often called the Itô-Stratonovich dilemma, arises in stochastic models where the noise is state-dependent (or *multiplicative*). Depending on whether one evaluates the steps' sizes based on the noise magnitude at the beginning of each step, at the end, or somewhere in between, the particle will either drift or not drift [32, 5, 31, 40]. Experiments must resolve the dilemma.

First, we present a simple theory which we will use to analyze particle motion in a viscosity gradient. Then, we present some basic concepts and results related to electrokinetics and fluidic systems, which serve as background for our experiments in this and later chapters.

2.1 Theoretical background on Brownian motion and stochastic processes

2.1.1 Random walk

We will start with a familiar model of diffusion, the one dimensional random walk. This will serve as the basis for a more general description using stochastic calculus. In its simplest version, the random walker always steps a constant length, has an equal probability of stepping left or right, and has no step-to-step correlation. In each step, the walker's position, x , changes by a small but fixed amount, L , in either the positive or negative direction, $\Delta x_i = r_i L$. The random variables r_i represent the choice of direction and have values of either -1 or 1 with equal probability. This leads to a simple equation of motion,

$$x_n = \sum_{i=0}^n \Delta x_i = \sum_{i=0}^n r_i L, \quad (2.1)$$

Where x_n is the position of the random walker after n steps. It is simple to calculate the average behavior of the random walker,

$$\langle x_n \rangle = L \sum_{i=0}^n \langle r_i \rangle = 0 \quad (2.2)$$

Quantities inside angled brackets represent averages over different realizations of that random variables. Since $r_i = \pm 1$ with equal probability, their average value is zero, $\langle r_i \rangle = 0$ and the average position of the walker is zero. The average of the *square* of the displacement is not zero.

$$x_n^2 = L^2 \sum_{i,j=0}^n r_i r_j \quad (2.3)$$

$$\langle x_n^2 \rangle = L^2 \sum_{i,j=0}^n \langle r_i r_j \rangle \quad (2.4)$$

Because r_i are uncorrelated and have values of only 1 or -1 ,

$$\langle r_i r_j \rangle = \delta_{ij} \equiv \begin{cases} 1 & \text{if } i = j \\ 0 & \text{if } i \neq j \end{cases} \quad (2.5)$$

where δ_{ij} is known as the Kronecker delta. Now, we can rewrite equation 2.4 as,

$$\langle x_n^2 \rangle = L^2 \sum_{i,j=0}^n \delta_{ij} = L^2 \sum_{i=0}^n 1 = nL^2 \quad (2.6)$$

If each step happens in a time Δt , the total time is $t = n\Delta t$ and

$$\langle x_n^2 \rangle = \frac{tL^2}{\Delta t} = 2Dt \quad (2.7)$$

where $D \equiv \frac{L^2}{2\Delta t}$. D is known as the diffusivity or the diffusion coefficient.

Going forward, we will model diffusion with a stochastic differential equation,

$$dx = x_{t+dt} - x_t = \sqrt{2D}dW_t, \quad (2.8)$$

where dx is the displacement of a particle over the interval starting at time t and ending at $t + dt$. W_t is a Wiener process, a continuous random process based on the random walk. Its increments, $dW_t = W_t - W_{t+dt}$, have a Gaussian distribution with mean $\langle dW_t \rangle = 0$ and variance $\langle dW_t^2 \rangle = dt$ [21]. It is common and convenient to simplify equation 2.8 by replacing $\sqrt{2D}$ with σ , which directly represents the magnitude of the noise term,

$$dx = x_{t+dt} - x_t = \sigma dW_t. \quad (2.9)$$

If σ is constant in space, it is easy to analyze this equation. Taking the expectation value gives no displacement,

$$\langle x_{t+dt} \rangle = \langle x_t \rangle + \sigma \langle dW_t \rangle = 0, \quad (2.10)$$

but a mean squared displacement that increases linearly with time,

$$\langle x_{t+dt}^2 \rangle = \langle x_t^2 \rangle + \sigma^2 \langle dW_t^2 \rangle = \langle x_t^2 \rangle + \sigma^2 dt. \quad (2.11)$$

2.2 Multiplicative noise and the Itô-Stratonovich Dilemma

What happens, then, to a particle diffusing in a medium whose viscosity varies with position? For some, it seems intuitive that viscosity should cause no net motion of a diffusing particle, because

viscosity does not change the potential energy of a particle, and therefore should not lead to a force. For others, a particle ought to drift toward higher viscosity, getting stuck in the mud. Still, others feel a particle will escape into regions of low viscosity where mobility is higher. It turns out that each of these possibilities corresponds to subtly different theories, each mathematically valid.

When the diffusivity varies with position, i.e. $D = D(x)$ and $\sigma = \sigma(x)$, the system is driven by *multiplicative* noise – noise whose magnitude is multiplied by a function of the system’s state [5]. Equation 2.9 becomes,

$$dx = x_{t+dt} - x_t = \sigma(x)dW_t. \quad (2.12)$$

This raises a mathematical difficulty. To calculate this increment dx , we need to choose a value of σ , but which one is correct? The value at the beginning or the increment, $\sigma(x_t)$, the value at the end of the increment, $\sigma(x_{t+dt})$, or some other value of σ ? As we will show below, this choice has physical consequences.

This problem is sometimes called the Itô-Stratonovich dilemma: Different rules for summing the stochastic displacements in equation 2.12, each one mathematically valid, result in different dynamics and therefore amount to subtly different models of Brownian motion.

The Itô integration rule (Fig. 2.1a) determines each displacement based on the value of σ at the origin of the displacement, i.e. $\sigma(x_t)$. This results in displacements that are the same regardless of the direction of dW_t , so individual particles do not drift preferentially in either direction. The Stratonovich rule (Fig. 2.1b) evaluates displacements at the midpoint, i.e. based on $\sigma(x_{t+\frac{1}{2}\Delta t})$. Finally, the isothermal (or Hänggi) rule bases the step size on the end point, i.e. it uses $\sigma(x_{t+\Delta t})$ (Fig 2.1c) [41, 42]. In this case, particles take larger average steps in the direction of increasing σ , resulting in mean drift toward lower viscosity.

We can analyze the effect of the integration rule analytically. Starting with equation 2.9 with $\sigma = \sigma(x)$,

$$dx = \sigma(x)dW_t, \quad (2.13)$$

we can introduce α to parameterize the choice of integration convention.

$$dx = \sigma(x + \alpha dx)dW_t \quad (2.14)$$

The parameter α runs continuously from 0 to 1. The Itô, Stratonovich, and isothermal rules are

special cases of equation 2.14, represented by $\alpha = 0$, $\alpha = 1/2$, and $\alpha = 1$, respectively. The influence of the integration convention on the dynamics of the Brownian walker is revealed by expanding $\sigma(x + \alpha dx)$,

$$\begin{aligned} dx &= \sigma(x)dW_t + \alpha \frac{d\sigma}{dx} dx dW_t \\ &= \sigma(x)dW_t + \alpha \frac{d\sigma}{dx} \sigma(x)dW_t^2. \end{aligned} \quad (2.15)$$

Reinserting $D(x)$ gives,

$$dx = \sqrt{2D(x)}dW_t + \alpha \frac{dD(x)}{dx} dW_t^2. \quad (2.16)$$

Finally, taking the expectation value,

$$\begin{aligned} x_{t+dt} &= x_t + \left\langle \sqrt{2D(x)} \right\rangle \langle dW_t \rangle + \alpha \left\langle \frac{dD(x)}{dx} \right\rangle \langle dW_t^2 \rangle \\ \langle x_{t+dt} \rangle &= \langle x_t \rangle + \alpha \left\langle \frac{dD(x)}{dx} \right\rangle dt. \end{aligned} \quad (2.17)$$

or

$$\langle \dot{x} \rangle = \alpha \left\langle \frac{dD(x)}{dx} \right\rangle \quad (2.18)$$

This drift, which occurs under the isothermal integration rule ($\alpha = 1$) but not under the Itô integration rule ($\alpha = 0$), is sometimes called *noise-induced drift* or *spurious drift* [43, 5].

2.3 Connection to Fick's law

In the above sections we view diffusion from the perspective of individual particles. Another approach is to consider the evolution of the distribution of a group of particles. Fick's first law relates the diffusive flux of particles to their distribution, $\rho(x)$, in a system with constant diffusivity D ,

$$J = -D \frac{d\rho}{dx}. \quad (2.19)$$

But what happens when D varies with space? There are two straightforward ways to generalize equation 2.19. We can put $D(x)$ outside the derivative or inside it,

$$J = -D(x) \frac{d\rho}{dx}. \quad (2.20)$$

$$J = -\frac{d(D\rho)}{dx}. \quad (2.21)$$

Of course, both equations reduce to equation 2.19 when the diffusivity is constant. Equation 2.20 is often called the Fick generalization of Fick's law and equation 2.21 is called the Fokker-Planck generalization. It turns out that these options correspond to the different integration rules defined in section 2.2.

Starting with the results of section 2.2, we can connect equation 2.20 to the isothermal integration rule and equation 2.21 to the Itô rule. We can demonstrate this by returning to a random walk model based on the Itô rule and considering particles that hop right (in the positive direction) and hop left (negative direction) separately. We will estimate flux by counting the difference in the number of particles we expect to hop past a test point x' in each direction. For a particle that hops to the right and arrives at x' ,

$$x' = x^- + \sqrt{2D(x^-)dt}, \quad (2.22)$$

where x^- is the starting point. The number of particles that will cross x' from the left will be half the number of particles between x' and x^- . We can approximate $D(x^-)$ with a expansion of $D(x)$ about the point x' ,

$$x' - x^- \approx \sqrt{2 \left[D(x') - \frac{dD}{dx}(x' - x) \right] dt}. \quad (2.23)$$

Solving for $x' - x^-$ gives,

$$x' - x^- \approx \sqrt{2D(x')dt} - \frac{dD}{dx} dt \quad (2.24)$$

Now we can approximate the number of particles that will cross x' from below as,

$$n_+ \approx \frac{1}{2} \left[\sqrt{2D(x')dt} - \frac{dD}{dx} dt \right] \rho, \quad (2.25)$$

where ρ is the particle density at x' . We get similar results when considering particles passing x'

from the right,

$$x^+ - x' \approx \sqrt{2D(x')dt} + \frac{dD}{dx}dt \quad (2.26)$$

$$n_- \approx \frac{1}{2} \left[\sqrt{2D(x')dt} + \frac{dD}{dx}dt \right] \rho, \quad (2.27)$$

Subtracting the number crossing x' in each direction gives the flux for $\alpha = 0$,

$$J = (n_+ - n_-)/dt = -\rho \frac{dD}{dx} \quad (2.28)$$

In the case of $\alpha \neq 1$, we need to add the flux due to the drift in equation 2.18, $J \approx \rho v = \rho \alpha \frac{dD}{dx}$. In the general case then,

$$J = -(1 - \alpha)\rho \frac{dD}{dx} \quad (2.29)$$

If there is a concentration gradient, this adds a flux governed by Fick's first law,

$$J = -(1 - \alpha)\rho \frac{dD}{dx} - D \frac{d\rho}{dx} \quad (2.30)$$

When $\alpha = 0$, equation 2.30 reduces to

$$J = -\frac{d(D\rho)}{dx}. \quad (2.31)$$

When $\alpha = 1$, equation 2.30 reduces to

$$J = -D \frac{d\rho}{dx}. \quad (2.32)$$

These correspond to equations 2.20 and 2.21.

2.4 Experimental background – Electrokinetics and microfluidics

Several fluidic and electrokinetic concepts are relevant in later sections. Here, we will describe pressure-driven flow in a channel, surface charge and the accompanying screening layer, electrophoresis, electro-osmosis, and streaming current. Then we will discuss an early experiment we performed to measure ionic motion driven by a viscosity gradient. This experiment shares some key features with the experiment we will describe in chapter 3.

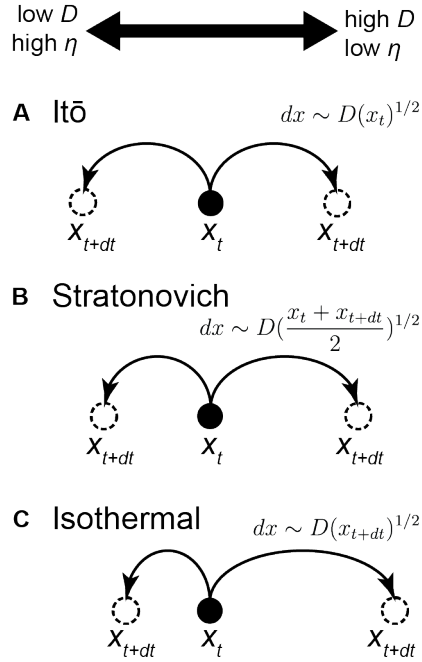


Figure 2.1: Stochastic displacement models. Illustrations show leftward and rightward steps of random walks corresponding to (a) the Itô, (b) the Stratonovich rule, and (c) the isothermal rule.

2.4.1 Flow in a pipe or channel

Because of non-linearities in the Navier-Stokes equations, few closed-form solutions for fluid flows are known [44]. Poiseuille flow, steady-state pressure driven flow in a long pipe or wide rectangular channel, is one of these known solutions. Viscous shear forces originating at the boundaries balance the force of pressure, so the flow speed increases with distance from the nearest wall. The result is the parabolic flow profile illustrated in figure 2.2 [44]. For a wide rectangular channel, the solution is

$$u(y) = -\frac{y}{2\eta} \frac{\Delta P}{L} (h - y), \quad (2.33)$$

where $u(y)$ is the flow speed a distance y from the bottom of the channel, $\frac{\Delta P}{L}$ pressure drop per unit length, η is the fluid viscosity, h is the height of the channel. Integrating equation 2.33 across in y and z , gives the flow rate,

$$Q = \frac{wh^3}{12\eta} \frac{\Delta P}{L}. \quad (2.34)$$

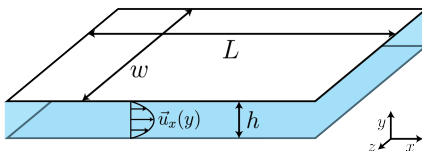


Figure 2.2: Poiseuille flow in a wide channel.

A similar equation describes the flow rate in a cylindrical pipe,

$$Q = \frac{\pi r^4}{8\eta} \frac{\Delta P}{L}. \quad (2.35)$$

My website contains a demo of two dimensional Poiseuille flow ¹ [45].

2.4.2 Surface chemistry and surface charge of glass

Surfaces are essential to electrokinetic phenomena. A relatively simple model by Behrens and Grier explains the behavior of a glass well [46]. At the surface of a piece of glass, which has the chemical formula SiO_2 in the bulk, are terminal chemical groups called silanol [46]. The acid dissociation constant of these chemical groups is estimated to be about $pK_a = 7.5$ [46], meaning the glass surface has the properties of a weak acid. Figure 2.3a shows the chemical structure of the glass before and after the introduction of basic and acidic solvents. Before dissociation, the terminal O–H groups are generally intact. The introduction of a basic solution pulls many protons off of the glass, leaving a negatively charged glass surface with a high charge density. The introduction of a weakly acidic solution pulls fewer protons off of the glass, and leaves a sparsely charged surface.

This negative charge attracts a cloud of positive mobile counterions into the vicinity [21]. Figure 2.3b shows the distribution of these ions. Electrostatics draw the ions toward the surface, while thermal energy keeps them away. The linearized Poisson-Boltzmann equation, $\frac{d^2\phi}{dx^2} = \frac{2c_0e^2}{\epsilon\epsilon_0k_B T}\phi$, can be used to approximate this system. Its solution in one dimension,

$$\phi(x) = \phi_0 e^{-\kappa x}, \quad (2.36)$$

is called the Poisson-Boltzmann distribution. It has a characteristic decay length known as the

¹<http://www.benwiener.com/physics/poiseuille.html>

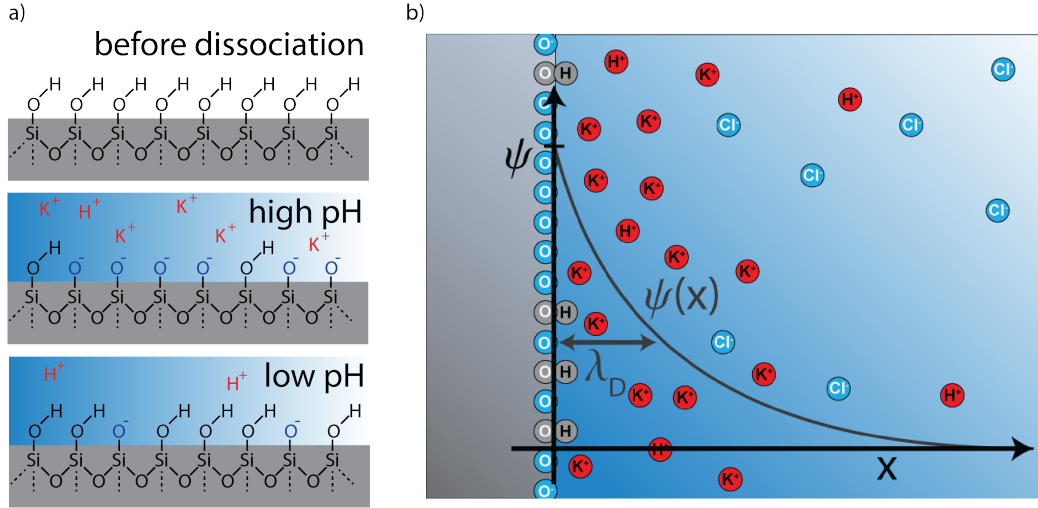


Figure 2.3: Glass surface schematic. a) Chemical diagram of an ideal glass surface. Before dissociation, terminal silanol groups are protonated. When the pH of the solution is high, protons are in low concentration. Many protons dissociate from the glass surface, leading to a highly charged surface. When the pH is low, fewer protons dissociate, leaving a less charged solution. b) A cloud of positive counterions screening a negatively charged glass surface. Plotted line shows the electric potential, $\phi(x)$. This equilibrium is a balance between electrostatic forces drawing counterions toward the surface and thermal energy.

Debye length [21],

$$\lambda_d = \kappa^{-1} = \sqrt{\frac{\epsilon\epsilon_0 k_B T}{2c_0 e^2}}. \quad (2.37)$$

A monovalent salt concentration of 200 mM gives a Debye length of about one nanometer [21].

The surface chemistry of glass, therefore, results in a cloud of positive and mobile counterions. The layer of surface charges and the attracted counterions are often called the *electric double layer* or EDL.

2.4.3 Electrophoresis

In an electric field, charged particles like those in the EDL experience a force proportional to the electric field, \vec{E} , and the charge, q , equal to $F_E = q\vec{E}$. This force drags the ions through the surrounding fluid, accelerating them until viscous drag matches the electric force. Solving the Navier-Stokes equations for a spherical particle in viscous flow at low Reynolds number gives the viscous force as a function of drift speed, v_d , as $F_v = 6\pi\eta r v_d$, where r is the particle's radius and η is the viscosity of the fluid [47, 21]. Applying this to our drifting ions by modeling them as spheres

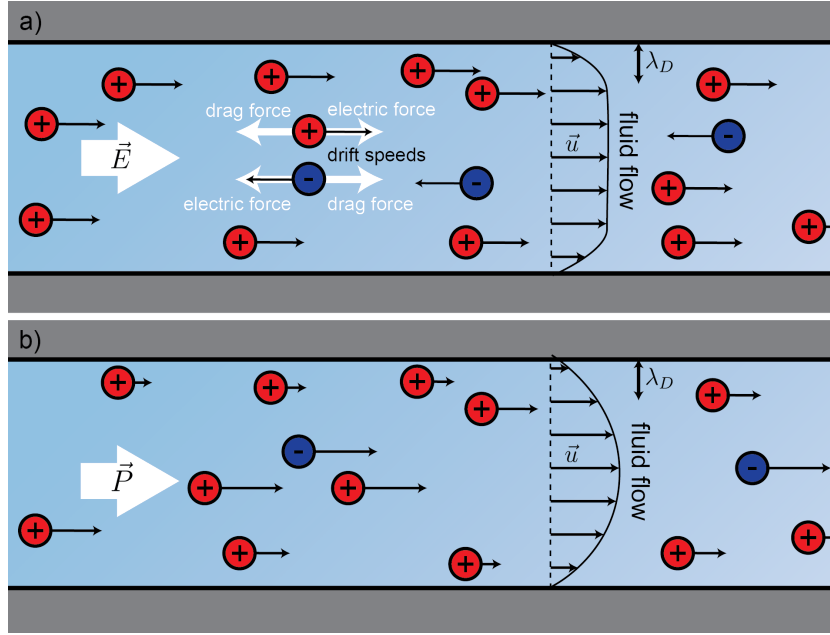


Figure 2.4: a) An electric field drives the electrophoretic motion of charged particles in a channel. The charged particles exert a viscous force on the fluid and cause electro-osmotic flow. b) Hydrostatic pressure pushes fluid through a channel. The flow carries charged particles in the EDL, causing a streaming current.

and equating the electric and viscous forces, we get an electrophoretic drift speed,

$$v_d = \frac{qE}{6\pi\eta r}, \quad (2.38)$$

where r is now an effective hydrodynamic radius for the charged particle. Note that oppositely charged particles drift in opposite directions. Figure 2.4a illustrates electrophoresis, showing charged particles drifting with balanced electric and viscous forces.

2.4.4 Electro-osmosis

The viscous force that the fluid exerts on the charged particle is matched by an equal and opposite force on the fluid. This force causes a fluid flow called electro-osmotic flow. In the bulk, positive and negative charges, which move in opposite directions in an electric field, exist in equal concentration and cause no net force on fluid. Within a Debye length of a charged surface, where net positive charge resides in the EDL, the fluid experiences a net drag from ions. In this surface region, the force exerted by the ions is balanced by viscous shear forces. This means that the shear rate and

the force of the electric field on the ions must balance,

$$\eta \frac{\partial^2 u_x}{dy^2} + \rho E = 0, \quad (2.39)$$

where u_x is the flow speed parallel to the wall, ρ is the density of net charge. The result is a flow profile which is flat in the bulk where no stress exists and falls to zero inside the EDL to conform with the no-slip condition. Figure 2.4a illustrates an electro-osmotic fluid flow profile. If the Debye length is small, outside of the EDL, the bulk electro-osmotic flow velocity is related linearly to the electric field, E ,

$$v_{\text{bulk}} = -\frac{\epsilon\zeta}{\eta}E, \quad (2.40)$$

where η is the fluid viscosity and ϵ is the dielectric constant [19, 48]. The last parameter, ζ , represents the zeta potential, which is the electric potential slightly away from a surface, where the first layer of mobile fluid molecules sits [19, 48], and is approximately equal to ϕ_0 in equation 2.36.

2.4.5 Streaming current

Similarly, a pressure driven flow can cause an electric current called streaming current. Figure 2.4b illustrates pressure driven flow inside a channel with charged surfaces. The ions are advected by the flow and move with a speed that corresponds to the local fluid flow speed. In the bulk, equal positive and negative charges exist, so no current results from the flow. Near surfaces, the motion of the net positive charge in the EDL results in current. We can write this current as [48],

$$I = w \int_0^h \rho(y)u_x(y)dy. \quad (2.41)$$

My website contains an interactive demo of streaming current ² [49]. If the Debye length is small, the flow profile can be taken as linear near the wall and the streaming current can be approximated [19, 48],

$$I = \frac{\epsilon\zeta}{\eta}wh \frac{\Delta P}{L}. \quad (2.42)$$

²http://www.benwiener.com/physics/streaming_current.html

2.4.6 Generalized forces and flows

The effects described above can be written in a neat form,

$$\begin{bmatrix} I \\ Q \end{bmatrix} = \begin{bmatrix} G_e & k_{ef} \\ k_{fe} & G_f \end{bmatrix} \begin{bmatrix} \Delta V \\ \Delta P \end{bmatrix} \quad (2.43)$$

where I is the electric current, Q is the flow rate, ΔV is a voltage difference, ΔP is a pressure difference, G_e is the electrical conductance, G_f is the fluidic flow conductance. The off-diagonal cross-terms k_{ef} and k_{fe} represent the strength of the streaming current and electro-osmotic flow effects, respectively, and are required by Onsager's reciprocal relations to be equal [19]. Reviewing equations 2.40 and 2.42, we see that $k_{ef} = k_{fe} = \frac{\epsilon \zeta}{\eta} \frac{A}{L}$

2.5 Measuring drift in a viscosity gradient using glass nanocapillaries

Nanopores can take a variety of forms, but their essential characteristic is a nano-scale opening. Most commonly, a tiny hole is bored into a flat silicon nitride membrane, forming a *solid state nanopore*. All of the current that goes through a nanopore needs to pass through a tiny space. This makes them electronic tools that are sensitive to nano-scale effects. We used a different kind of nanopore, a pulled glass nanocapillary with a nano-scale opening at the end, to detect the motion of ions in a viscosity gradient. We wondered if it would be possible to put liquids with different viscosities inside and outside the capillary and electronically measure the motion of ions in response to a viscosity gradient as an electric current.

Figure 2.6a illustrates the experimental setup. We filled a pulled glass nanocapillary with a liquid, and dipped the tip into a bath of a different liquid. We inserted the electrodes into the capillary and into the bath. At the tip of the capillary, a gradient forms between the two liquids. For this experiment, we used binary mixtures of water and glycerol. The higher the glycerol fraction, the higher the viscosity.

Figure 2.5a shows how we made these capillaries using a Sutter P-97 micropipette puller. They start as a 1 mm outer diameter, 0.5 mm inner diameter glass tube. The machine heats the middle of the tube with a tungsten filament and pulls on both ends. When the middle of the tube nears its

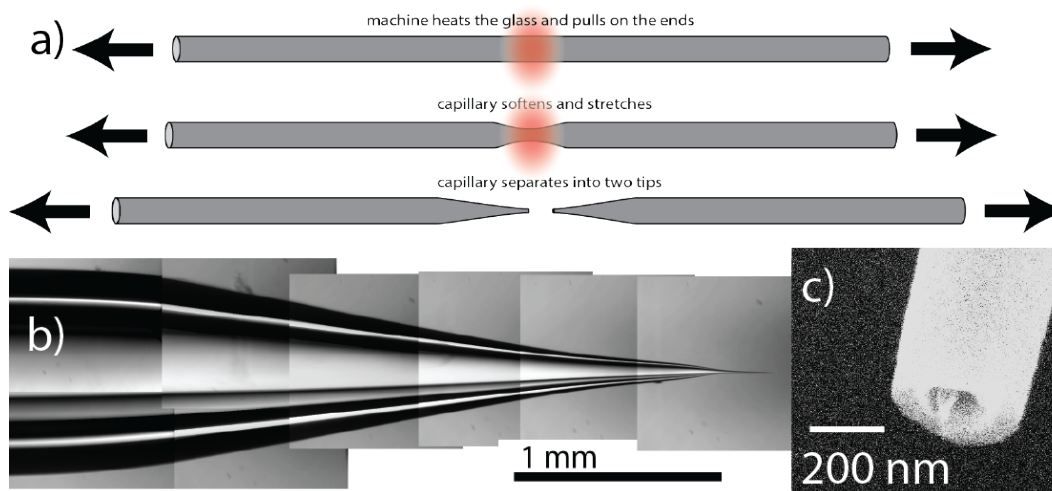


Figure 2.5: Pulled glass nanocapillaries. a) The method used by the Sutter P-97 Micropipette Puller. b) A composite microscope image of a nanocapillary. c) An scanning electron microscope image of the opening of a nanocapillary

melting point, it softens and stretches into a roughly conical shape. Figure 2.5b shows a composite microscope image of a pulled nanocapillary. Figure 2.5c shows a scanning electron microscope image, which reveals that the tube tapers to a final inner diameter of less than 200 nm.

2.5.1 Detecting drift using surface counterions

Our strategy was to take advantage of the surface charge of glass to electronically measure drift driven by a viscosity gradient in a nanocapillary. As explained in section 2.4.2, glass is generally negatively charged in solution, and it attracts a cloud of positive counterions to screen it. A nanoscale channel made of glass will have a high ratio of surface area to volume, and will therefore have a significant excess of positive ions. Any systematic drift of these excess ions would constitute an ionic current, which we could measure electronically. The drift of ions in the bulk would not be measurable, because each of these ions is countered by another of opposite charge.

We used Ag\AgCl electrodes in our experiments. To prepare them, we started with silver wire, sanded off any oxidation on the outside, and submerged them in chlorine bleach for fifteen minutes. This had the effect of creating a AgCl coating on the surface of the electrode. The chemical half-reaction $\text{AgCl}(s) + e^- \rightleftharpoons \text{Ag}(s) + \text{Cl}^-$ allows the electrode to either emit a chloride ion via the forward reaction or absorb one by the reverse. We used an Axopatch 200B to measure the ionic currents generated within the chip.

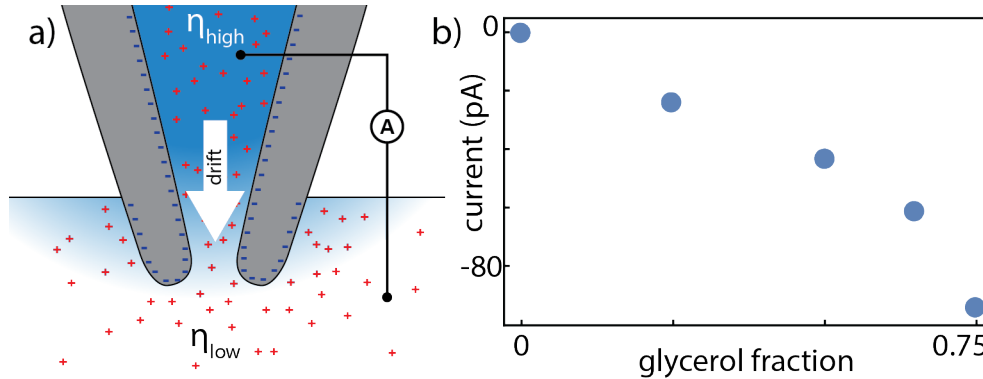


Figure 2.6: a) The tip of a glass nanopipette inside a liquid with lower viscosity. Positive ions screen the negatively charged surfaces. An ammeter detects and new motion of ions. b) Measured current plotted against glycerol fraction from a capillary experiment.

2.5.2 Electrokinetic rectification in glass nanopipettes

While experimenting with electric measurements in nanopipettes, we noticed diode-like rectification in the I-V curves we measured. This is actually a well-known effect; conical nanopores like our pulled nanopipettes often exhibit this interesting current rectification property [28]. Figure 2.7a shows solution conductivity-normalized I-V curves inside 200 nm inner diameter nanopipettes. We varied the NaCl concentration from 1 M to 0.1 mM. At 1 M, the I-V curve is linear, indicating normal ohmic behavior. At lower salt concentrations like 0.1 mM, we saw diode-like rectification, where a negative voltage drives much more current than the equivalent positive voltage. A simple qualitative model explains this behavior [50]. Because of the negative charge on the walls, the thinnest part of the capillary is partly *permselective*, meaning it is more permeable to positive ions than negative ones. The lower the salt concentration, the weaker the screening of the surfaces and the greater the permselectivity effect. When a positive voltage is applied, positive ions are depleted from the inside of the capillary, decreasing its conductance. The confined geometry means that few positive ions are available to replace the ones that are pushed out. When a negative voltage is applied, positive ions are forced into the capillary, enhancing its conductivity.

The geometry of the capillary combined with electrokinetics explains the rectification effect we saw, but similar rectification effects can be observed with different types of asymmetry. Differences in surface chemistry or salt concentration can also cause similar rectification effects [28].

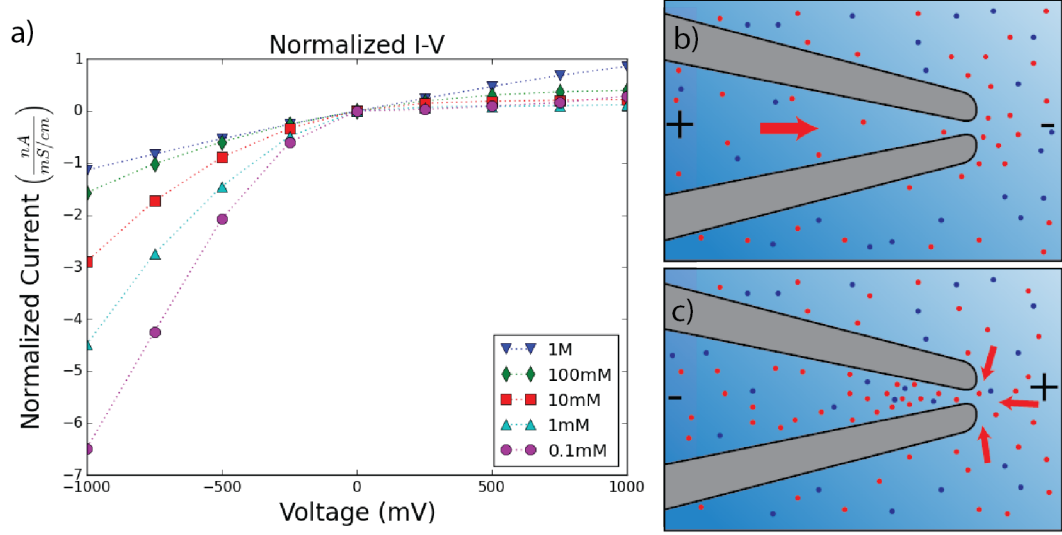


Figure 2.7: a) Current normalized by bulk conductivity plotted against applied voltage. b) When a positive voltage is applied inside the capillary, the tip is partially depleted of positive ions, decreasing the overall conductance. c) When a negative voltage is applied inside the capillary, the tip the concentration of positive ions inside the tip is enhanced, increasing the overall conductance.

2.5.3 Flow rate through glass nanocapillaries

We developed a method for measuring the flow rate through these tiny capillaries. The concept was simple: we filled the capillary with water and used it to blow a tiny water bubble into an immiscible medium. Using a microscope with a $60\times$ objective, we observed the size of the bubble over time and inferred its volume from the radius of the circle it projected onto the image plane. By analyzing a video recording of the growing bubble we were able to measure the flow rate of capillaries with radii ranging from 60 nm to 500 nm. We were able to detect flow rates on the order of 1 pL per second. For the immiscible medium, we used a somewhat visco-elastic silicone grease to prevent the bubbles from floating away.

Figure 2.8 shows the flow rates of fifteen nanocapillaries with different inner diameters. The inset shows an example bubble. We can use equation 2.35 to calculate the pressure drop, dP , over a short length of tube, dL ,

$$dP = \frac{8\eta}{\pi r^4} dL. \quad (2.44)$$

Then, we can integrate to estimate the pressure drop over a tube with a variable radius. We modeled the nanocapillary as an infinite cone with an angle θ , truncated so that the small end has a radius

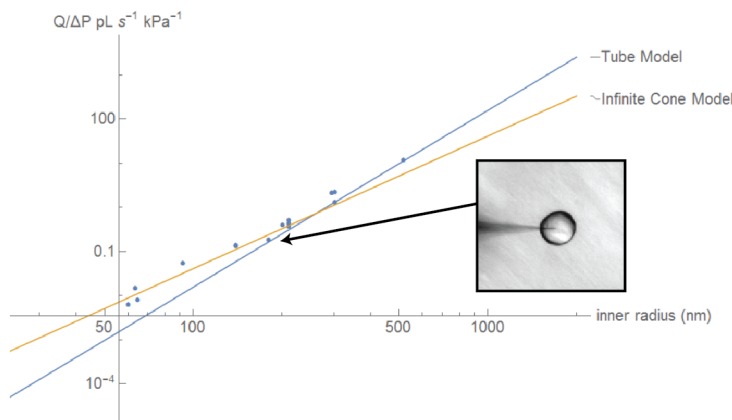


Figure 2.8: The flow rate per unit pressure as a function of capillary inner diameter. Inset shows the bubble used to measure the flow rate of one device. The yellow line shows the truncated cone model. The less successful tube model will not be discussed here.

r . From this, we find,

$$Q = \frac{3\pi r^3 \sin \theta}{8\eta} \Delta P. \quad (2.45)$$

Figure 2.8 shows this model plotted against the data.

2.5.4 Ionic current in a viscosity gradient

Using these nanocapillaries, we performed our viscosity gradient experiment. We saw evidence of current flowing from the more viscous side to the less viscous side. Figure 2.6b shows data from an experiment with water on one side and water-glycerol mixtures on the other. The measured current is plotted as a function of the glycerol fraction. This data was encouraging but hard to reproduce. We found the experiment to be wildly inconsistent, producing currents with different magnitudes in each trial. The tantalizing but unreliable results of this experiment prompted us to design a better experiment.

The geometry of our capillary experiment was not ideal. It was easy to change the solution outside of the capillary, but the solution inside was effectively stuck there. We worried about how the viscosity profile would evolve over time in this somewhat complicated configuration. We also identified an important asymmetry. Potassium chloride is much more soluble in water than in glycerol. This means that the ions are chemically drawn toward higher water concentrations.

Our experiments with nanocapillaries led us to design an improved experiment that solved two major problems with the capillary experiments. Instead of binary solutions of water and glycerol,

which caused gradients in KCl solubility and generated unwanted currents, we used ternary mixtures of water, glycerol, and formamide, which can be mixed to provide constant solubility. We also designed a glass chip which made it easy to maintain a viscosity gradient of choice.

2.6 Conclusion

It is surprising that the rule used to integrate Brownian motion can have a real physical effect which can be probed experimentally. More than one hundred years after the discovery of Brownian motion, controversy still exists about relatively straightforward variations of the basic effect. So far, measurements of particles diffusing in a viscosity gradient have been unsatisfying. Of the two measurements based on the subtle diffusion stifling effect of a solid surface, one has had its conclusions publicly questioned, and the other takes place over tiny length scales, confined to the space within a few particle widths from a solid surface. A third experiment, using gelatin to control viscosity, arrives at a different conclusion from the others. Meanwhile, two simulations with different but reasonable implementations produce opposite results. Our first try at addressing this problem experimentally was encouraging but flawed. We seek to provide a convincing experiment to quantify the effect of a liquid viscosity gradient on diffusing particles.

Chapter 3

Electrokinetic Current Driven by a Viscosity Gradient

Electrokinetic transport phenomena like electrophoresis, thermophoresis, and diffusiophoresis, which arise from gradients in voltage, temperature, and solute concentration, respectively, play important roles in biology, geology, and micro- and nanofluidic systems[51, 52, 19]. Could gradients in viscosity, which are ubiquitous in nature and technology, also drive transport? Micro- and nanofluidic devices have proven to be successful toy systems for probing electrokinetic effects. It is now easy to fabricate these tiny but tightly-defined channels with well-known techniques. The small volume and high aspect ratios achievable in these systems enhance the effects of surfaces and make subtle electrokinetic effects observable. Here, we present the first electrokinetic measurement of viscosity-gradient driven motion.

3.1 Experimental methods

We experimentally imposed a controlled viscosity gradient in the liquid filling a glass nanochannel and measured the electrical current resulting from the drift of counterions in the electric double layers near the nanochannel's charged surfaces. Figure 3.1 illustrates the basic setup. The nanofluidic device was a glass chip containing a 150 μm -wide, 50 nm-deep mixing channel that bridged two parallel 0.5 μm -deep microchannels (Fig 3.1(b)).

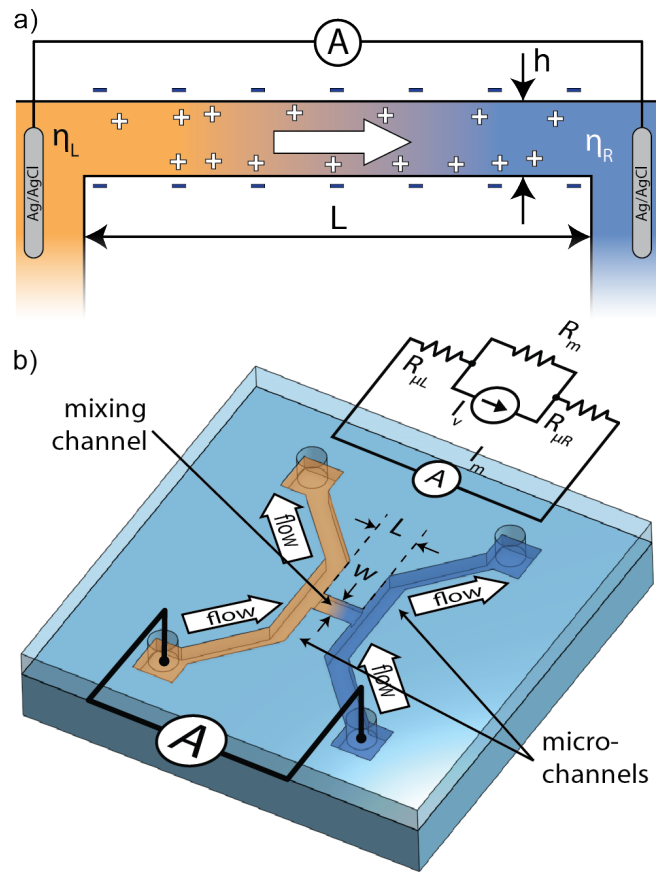


Figure 3.1: (a) Sketch of the mixing channel cross section showing counterions drifting in the direction of lower viscosity. (b) 3D sketch of the nanofluidic chip indicating w and L . The equivalent circuit diagram shows how I_v , modeled as a current source, is related to I_m , R_m , $R_{\mu L}$, and $R_{\mu R}$.

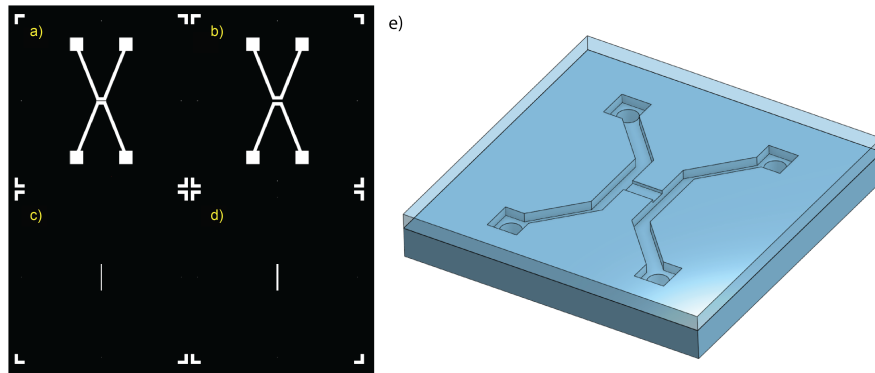


Figure 3.2: **Chip fabrication.** The masks used to expose the microchannels for chips with a) 100 and b) 400 μm long nanochannels. The masks used to expose the c) 50 and d) 150 μm wide nanochannel. e) A 3D rendering of the finished chip.

We pumped miscible liquids with viscosities η_L and η_R through the left and right microchannels past either end of the mixing channel, inside which the liquids interdiffused. The flow in the microchannels continuously refreshed the liquids at the left and right ends of the mixing channel, fixing the viscosities there at η_L and η_R , respectively, and reaching steady state in between. We measured the ionic current flowing through the device, I_m , using an ammeter (Axon Axopatch 200B) with Ag/AgCl electrodes immersed in liquid on either side.

3.1.1 Fabrication of chip-based fluidic devices

We made the chips by etching the fluidic channel pattern into glass wafers and then thermally bonding a thin cover to enclose them. We started with fused silica wafers (Marc Optics), cut into one-inch squares and thoroughly cleaned. The pattern required two stages of etching. First, we spun about 2 μm of S1818 photoresist onto the wafer and soft baked it. S1818 is a positive photoresist, so areas exposed to sufficient UV radiation become soluble in the developer solution. We exposed and developed the mixing channel first, using a pattern like in figure 3.2c, leaving bare glass in the shape of the mask. Then, we used CF_4 plasma to etch away about 50 nm of glass. We used a profilometer to check the dimensions of this feature. Next, we spun on a new layer of resist and repeated the process with the pattern for the microchannels in figure 3.2a, being careful to align the two patterns. We removed all the resist and measured the key features using the profilometer. We used an alumina powder blaster to cut holes into each of the square reservoirs. After one final chemical etch in hydrofluoric acid, we bonded a thin cover and baked the chip overnight at 1000 $^\circ\text{C}$.

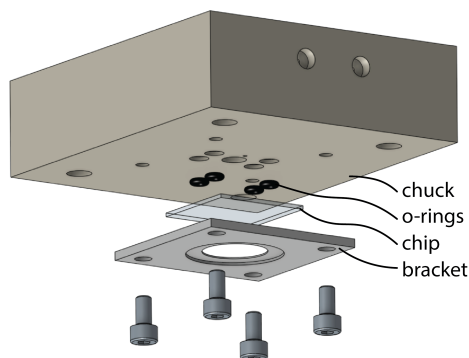


Figure 3.3: **Exploded view of chuck.** Shows the chip, which (when assembled) is sealed to the chuck with o-rings and fastened to the chuck with an aluminum bracket and screws.

Figure 3.2e shows a rendering of the completed chip. Four holes in the chip give access to the channels.

We made four chips in four separate runs. The first set of chips were used to collect most of the data. They had mixing channels that were 200 μm long. The second run provided chips with mixing channels half as long and twice as long as those in the first series. The third and fourth set of chips were for followup experiments and for quantum dot experiments described in chapter 5.

3.1.2 Fluid flow control system

We designed a chuck to hold the chip in place, allow us to make electronic contact with the solutions inside, apply pressures, and replace the solutions with new ones. Figure 3.3 shows an exploded view of the chuck and chip assembly. The chip is sealed to the chuck with Viton o-rings and held in place with an aluminum bracket. Electrodes are inserted through the top of the chuck, along with thin tubing which allows us to flush old fluid out and replace it on the fly. These tubes were carefully cut so that they reached all the way to the openings of the chips.

To start an experiment, we aligned the holes in the chips with the holes in the chuck and carefully screwed the bracket in place. We then used the tubes in the top of the chuck to fill the areas surrounding the openings with the experimental liquids. It was important to avoid introducing bubbles into the openings of the chips because they are hard to remove and often result in unpredictable behavior. We used a mechanical pump and regulator supply 0.5 bar to drive fluid through the chips. After introducing a solution, we waited for the system to stabilize. Typically this took 10 to 30 min.

3.2 Making the experimental liquids

We used ternary liquid mixtures composed of water, formamide, and glycerol, with potassium chloride added to increase conductivity. The viscosity of glycerol is much higher than that of formamide (934 mPas compared with 3.34 mPas at 25 °C[53]), so by varying the ratio of those liquids with the water content kept constant at 50% by volume, we could vary the viscosity of the mixture. We achieved viscosities ranging from 1.4 to 6.1 mPas. We first prepared a stock solution of water, KCl, and a pH buffer. For this water stock, we always used a concentration of 10 mM for the buffers, and 200 or 1000 mM for the salt. We then made binary mixtures of glycerol and formamide: 100% glycerol; 75% glycerol, 25% formamide; 50% glycerol, 50% formamide; 25% glycerol, 75% formamide; and 100% formamide. We mixed the water stock solution with the various glycerol-formamide mixtures 1:1 by volume, halving the concentration of the salt. We then titrated the resulting solutions to the target pH using either HCl or KOH.

We used water combined with mixtures of glycerol and formamide to minimize chemical potential gradients in our nanochannel. KCl has very similar solubilities in glycerol and formamide, so chemical effects that would draw ions into one solution or another are minimized. This effect is analyzed quantitatively in section 3.7.1.

3.2.1 Controlling conductivity and pH

We wanted the liquids to be conductive so that any ionic current originating within the mixing channel could be transmitted to the electrodes. We added KCl to the liquids to a concentration of either 100 or 500 mM. This brought the conductivity to the range of 200 mS m⁻¹, which was enough for our experiments. We used a Hach EC-71 conductivity meter to measure the conductivity of each liquid.

We also wanted to control the pH, because the pH has a strong influence on the surface charge density[54]. We made liquids of pH 8 and 5. For our liquids at pH 8, we used tris as a buffer, which has a pKa of 8.1[53]. For those at pH 5, we used a citric acid buffer, a triprotic acid with pKa values of 3.13, 4.76, and 6.40 for its three carboxyl groups. We used a Denver Instruments UB-10 pH meter to monitor the pH. It took on the order of 30 μ L of concentrated HCl or KOH to reach the pH targets.

We observed that the conductivities of the liquids increased over time. Figure 3.4a shows the

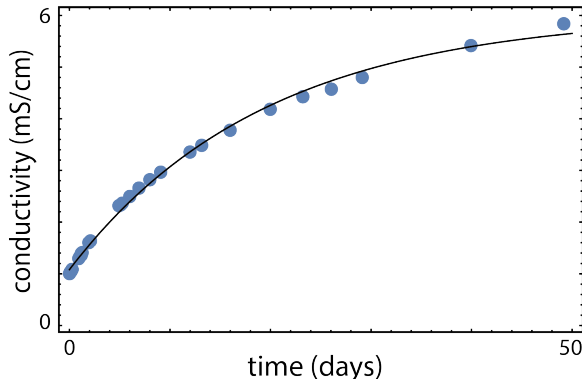


Figure 3.4: The conductivity of a solution of 50% water, 25% glycerol, 25% formamide with 100 mM KCl over time. Line shows best fit of an exponential function, equation 3.1.

conductivity over time for a solution of 50% water, 25% glycerol, 25% formamide with 100 mM KCl. The conductivity increases significantly on the timescale of a month. We modeled this conductivity curve with an exponential function,

$$\kappa(t) = a + be^{-ct}. \quad (3.1)$$

The line in figure 3.4a shows a best fit of this line and gives a time constant of 19.4 days.

3.2.2 Measuring liquid viscosity

We measured liquid viscosities using a ball-drop method[55]. We filled a small capillary ($L = 10$ cm, $r = 1.25$ mm) with the liquid, and added a small ($r = 500$ μm) steel ball. We measured the terminal velocity of the ball in the liquid.

According to Stokes drag, the force on a sphere of radius r moving with velocity v through a liquid of viscosity η is

$$f = 6\pi\eta rv. \quad (3.2)$$

The gravitational terminal velocity of a ball falling through a liquid is therefore inversely proportional to the liquid's viscosity. We can then measure the viscosity of a liquid, η , by comparing the time, t , for a ball to fall a constant distance with the time an identical ball takes to fall the same distance, t_0 , in a different liquid of known viscosity, η_0 .

$$\eta = t \frac{\eta_0}{t_0}. \quad (3.3)$$

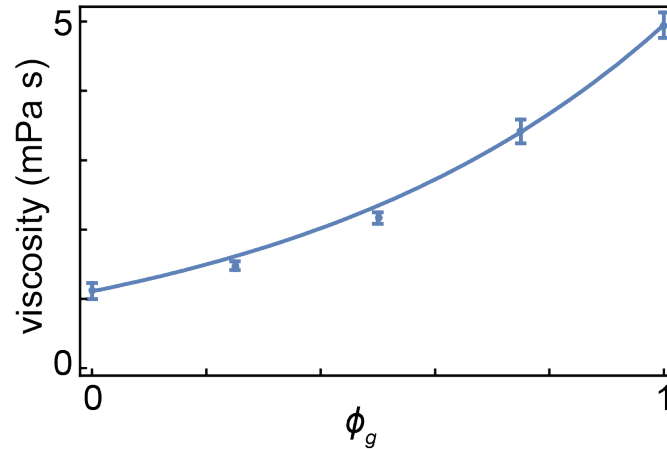


Figure 3.5: Dependence of the viscosity of a mixture of two liquids on the volume fraction of the higher-viscosity component. Symbols show measured viscosity of a mixture containing 50 % water, $\phi_g \times 50$ % glycerol, and $(1 - \phi_g) \times 50$ % formamide. The solid line shows eq. 3.20, where $\eta_f = 1.11$ mPa s and $\eta_g = 5.96$ mPa s.

We used water as as our liquid of known viscosity, $\eta = 0.890$ mPa s at 25 °C[53].

3.2.3 Dependence of the viscosity on the composition of the liquid mixtures

Predicting the viscosity of an arbitrary mixture of liquids of known viscosities is complicated, but we found that our solutions fit a simple model,

$$\eta(\phi) = \eta_a^{1-\phi} \eta_b^\phi. \quad (3.4)$$

which is well supported theoretically [56, 57]. Here, ϕ is the volume fraction of the liquid with viscosity η_a , and η_b the viscosity of the other liquid. Figure 3.5 shows the measured relationship between η and ϕ , where solution a is a 1:1 water/glycerol mixture, and solution b is a 1:1 water/formamide mixture.

3.3 Measuring surface charge density of nanofluidic channels

The surface properties of a nanofluidic channel are key to understanding any electrokinetic effect occurring within them. In particular, the surface charge density of our chips sets the strength of any viscosity-gradient-driven current. We estimated the surface charge density inside one of our glass chips using a conductance saturation technique [54]. We measured the conductance of a glass chip filled with solutions with KCl concentrations that varied from 10^{-1} mM to 10^1 mM in 50% water, 25% glycerol, 25% formamide. At higher salt concentrations, the conductance of the bulk dominated the overall conductance of the device. Because of the electric double layer described in section 2.4.2, there is always a cloud of counterions based on the magnitude of the surface charge. This means that the conductance has a lower bound corresponding to the conductance contributed by the EDL. Figure 3.6 shows the current at 200 mV plotted against the KCl concentration. The conductance decreased with bulk conductivity and eventually leveled out when the KCl 1 mM.

3.3.1 Conductance model for rectangular nano- and microscale channels

We modeled the expected conductance using the measured bulk conductivity to estimate the bulk conductance, and Stokes' drag to estimate the contribution of the surfaces. Using these models, we can estimate the conductance contributions of the bulk and of the surface and find the overall conductance with $G = G_{\text{bulk}} + G_{\text{surface}}$.

We can find the bulk resistance along a square channel of length L and cross-sectional area A from the conductivity using

$$G_{\text{bulk}} = \frac{1}{R_{\text{bulk}}} = \kappa \frac{A}{L}, \quad (3.5)$$

where κ is the conductivity of the bulk solution as measured by a conductivity meter. Combining contributions of the micro and mixing channels gives

$$I = \kappa V \left(\frac{L_m}{w_m h_m} + \frac{L_\mu}{w_\mu h_\mu} \right)^{-1}, \quad (3.6)$$

where w_m and h_m are the widths and heights of the mixing channels, and w_μ and h_μ are the widths and heights of the microchannels.

We estimated the contribution of the surface charge using a model based on Stokes' law which gives the drift speed of a particle moving through a viscous medium at low Reynolds number as a

function of the force on that particle. By applying this to charged particles in the EDL, we can estimate the current due to the EDL as a function of the applied electric field.

According to Stokes' law, the speed, v , of a particle with radius r moving through a fluid with a viscosity η under a force F is

$$v = \frac{F}{6\pi\eta r}. \quad (3.7)$$

For a particle with charge q in an electric field caused by a voltage difference ΔV dropping linearly over a distance L , the force can be written

$$v = \frac{\Delta V q}{6\pi\eta r L}. \quad (3.8)$$

The charge screening the surfaces in a length of channel ΔL is the surface area inside multiplied by the surface charge density,

$$\Delta Q = (2w + 2h)\Delta L\sigma. \quad (3.9)$$

If these ions are moving at a speed v , it takes a time $\Delta T = \Delta L/v$ for this charge to move a distance ΔL and

$$I = \Delta Q/\Delta T = (2w + 2h)\sigma v. \quad (3.10)$$

Plugging in equation 3.8 gives

$$I = (2w + 2h)\sigma \frac{\Delta V q}{6\pi\eta r L}. \quad (3.11)$$

or

$$G_{surface} = \frac{1}{R_{surface}} = \frac{(2w + 2h)\sigma q}{6\pi\eta r L}. \quad (3.12)$$

Combining the contributions from the micro and mixing channels gives,

$$I = \frac{6\pi\eta r}{\sigma q} \left(\frac{2w_m + 2h_m}{L_m} + \frac{2w_\mu + 2h_\mu}{L_\mu} \right). \quad (3.13)$$

Figure 3.6 shows plots of equations 3.13 and 3.6 in green and red respectively. We treated the surface charge density, σ , as a free parameter, which we used to fit the model to the data. This revealed a surface charge density of 200 mC m^{-2} in this device.

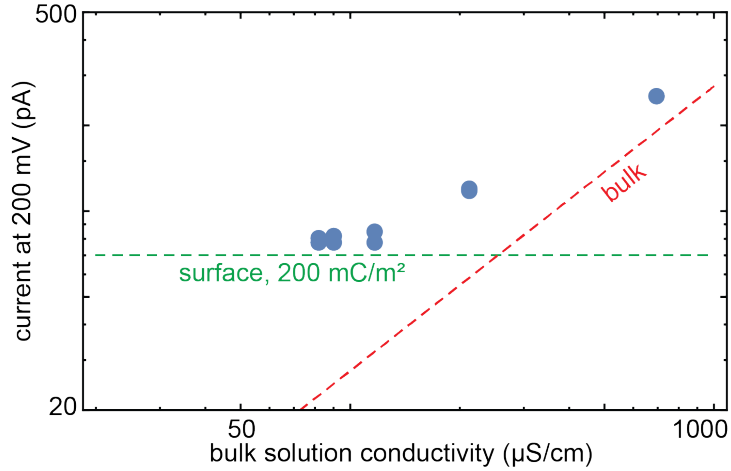


Figure 3.6: Measured current as a function of bulk solution conductivity. Red dashed lines show expected contributions from bulk ions, equation 3.6. Green dashed line shows expected contributions from ions screening the surfaces, equation 3.13.

3.4 Width of the boundary layers at the ends of the mixing channel

We used flows in the microchannels of our fluidic chips to refresh the solutions at either end of the mixing channel and maintain a controlled viscosity gradient. Nevertheless, the inter-mixing of the liquids in the channel and in the microchannels creates diffuse transition regions that increase the effective length of the mixing channel. This effect can influence the magnitude of the viscosity gradient. In this section, we theoretically calculate the width of the diffuse boundary layers at the ends of the mixing channel.

We take the flows in the microchannels to be in the positive y direction with constant and uniform speed u . Diffusion acts to transport molecules in the x direction. The interface between a microchannel and the mixing channel is illustrated in figure 3.7. A molecule of the fluid with diffusion coefficient D will diffuse a characteristic distance \sqrt{Dt} in a time t . The time it takes fluid flowing in the microchannel to traverse the width, w , of the mixing channels is $t = w/u$. Therefore, as fluid in a microchannel flows past the end of the mixing channel, diffusion creates a boundary layer that grows in width as $\sqrt{\Delta y}$ to a maximum value of $\sqrt{Dw/u}$ at the far edge of the mixing

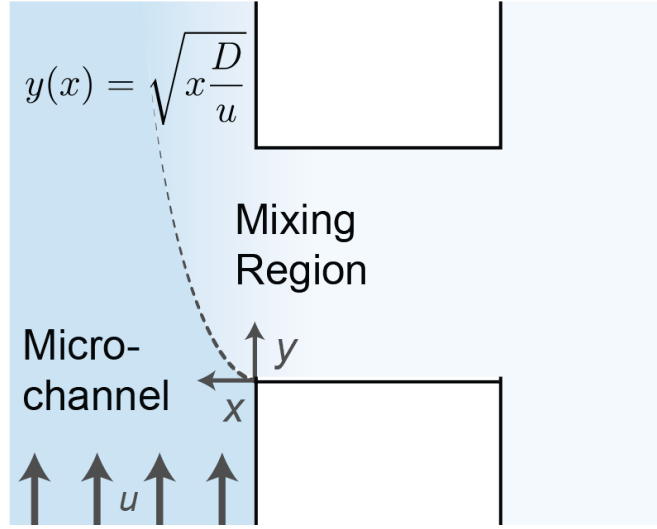


Figure 3.7: Sketch of the mixing region extending into a microchannel.

channel. The mean width of the boundary layer over the width of the mixing channel is

$$\Delta L_m = \frac{1}{w} \int_0^w \sqrt{\frac{Dl}{u}} dl = \frac{2}{3} \sqrt{\frac{Dw}{u}}, \quad (3.14)$$

and this represents the effective extension of the mixing region.

The maximum flow rate inside a wide, flat rectangular channel is

$$u = \frac{\Delta P}{8\eta} \frac{h^2}{L} \quad (3.15)$$

Combining equations 3.14 and 3.15 and the Stokes-Einstein equation ($D = \frac{k_B T}{6\pi\eta r}$) gives

$$\Delta L_m = \frac{4}{3} \sqrt{\frac{k_B T w L}{3\pi \Delta P r h^2}}. \quad (3.16)$$

Here w , L , and h are the width, length, and height of the microchannel. Notice that eq. 3.16 does not depend on the properties of the solution, only parameters that did not vary in our experiments. Using the experimental values from our typical experiment, $w = 150 \mu\text{m}$, $L = 1.8 \text{ cm}$, $h = 0.5 \mu\text{m}$, $\Delta P = 100 \text{ kPa}$, and $r = 1.25 \text{ \AA}$ gives a ΔL of $27 \mu\text{m}$. The boundary regions at the ends of the mixing channel are relatively small compared with the length of the mixing channel itself. In our analyses, we accounted for the small effective extension of the mixing channel due to diffusive mixing at the ends by taking $L = L_{mixing} + 2 \times \Delta L_m$, where L_{mixing} is the measured length of the mixing channel.

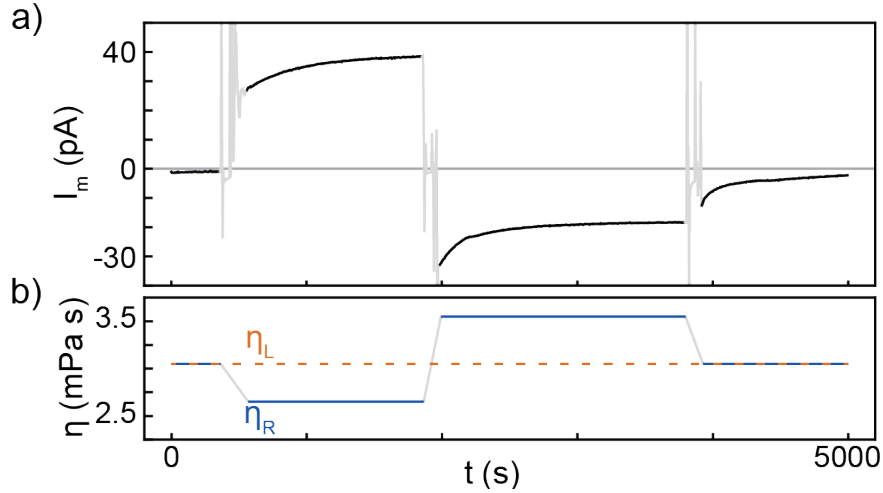


Figure 3.8: Measuring viscoporesis in nanofluidic channels. Traces of (a) I_v and (b) η_L (orange dashed) and η_R (blue) from a typical viscoporesis measurement.

3.5 Measurements of viscosity-driven currents in a nanofluidic channel

3.5.1 Typical experiment

Figure 3.8a plots I_m and Fig. 3.8b plots η_L and η_R during a typical experiment. After zeroing the ammeter on a resistive dummy load, we pumped identical liquids with viscosities $\eta_L = \eta_R = 2.6$ mPa s through both microchannels. The homogeneous viscosity condition within the mixing channel resulted in a stable current close to zero. Next, we imposed a viscosity gradient by flushing the right microchannel with a liquid with a lower viscosity, $\eta_R = 1.8$ mPa s. A current began to flow which settled at a stable value of $I_m = 38$ pA after about 25 minutes. The polarity indicated a flow of conventional (positive) current toward the right side. Next, we flipped the direction of the viscosity gradient by flushing the right channel with a liquid of higher viscosity $\eta_R = 3.6$ mPa s, and a current $I_m = -18$ pA flowed, this time toward the left channel. Finally, we re-established the homogeneous viscosity condition, and the flow of current halted.

The characteristic time for the system to reach steady state should roughly correspond to the average time for a liquid particle to diffuse the length of the channel, $t \approx \frac{L^2}{2D} \approx \frac{3\pi\eta r L^2}{k_B T}$. For a 200 μm channel and a diffusivity corresponding to a 5 \AA particle diffusing in a liquid with viscosity 3 mPa s, we get a characteristic time of 136 s. This looks roughly consistent with our data.

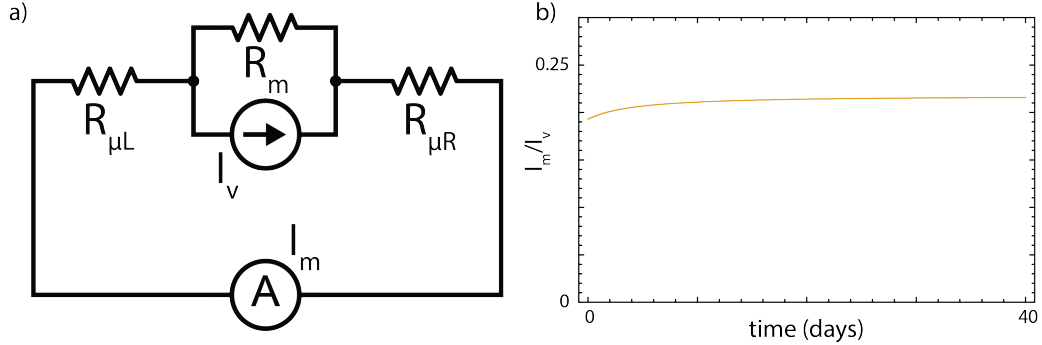


Figure 3.9: a) Equivalent circuit representing the experimental device. The viscosity gradient induced drift is treated as a constant current source. This current can fork back through the mixing channel or through the ammeter via the micro-channels. b) The time evolution of the ratio of I_m/I_v assuming bulk conductivity evolves as shown in figure 3.4a, according to the models in section 3.3.1

3.5.2 Equivalent circuit and current forking ratio

The current that a viscosity gradient generates within the mixing channel, I_v , forks into two parts. I_m is the part that flows to the ammeter, but another part flows back through the mixing channel. The forking ratio is determined by the relative electrical resistances of the mixing channel, R_m , the left microchannel, $R_{\mu L}$, and the right microchannel, $R_{\mu R}$. The equivalent circuit shown in figure 3.9 gives the relationship $I_v = I_m \frac{R_{\mu L} + R_{\mu R} + R_m}{R_m}$.

Fortunately, the conductivity variability described in section 3.2 does not cause the ratio I_m/I_v to change very much because it affects the conductivity of both the microchannels and the mixing channel. The effect causes the forking ratio to vary by a maximum of 12%.

3.5.3 Dependence of I_v on η_R and η_L

Figure 3.10a shows the dependence of I_v on η_R for four fixed values of η_L . The magnitude of I_v grew with the magnitude of the imposed viscosity difference. The current always flowed toward the lower viscosity side. The data from the four sets of measurements collapse onto a single curve when the product $I_v \eta_L$ is plotted against the viscosity ratio η_R/η_L , as shown in Fig. 3.10b.

Figure 3.11a compares the dependence of I_v on η_R for two mixing channels of different lengths, $L = 100$ and $400 \mu\text{m}$, with $\eta_L = 2.6 \text{ mPa}\cdot\text{s}$. The $400 \mu\text{m}$ mixing channel, which was four times longer than the other, produced about a quarter the current.

Figure 3.11b compares measurements performed using liquids buffered at pH 5 with liquids buffered at pH 8. The magnitude of I_v was approximately six times lower at pH 5 than at pH 8 for

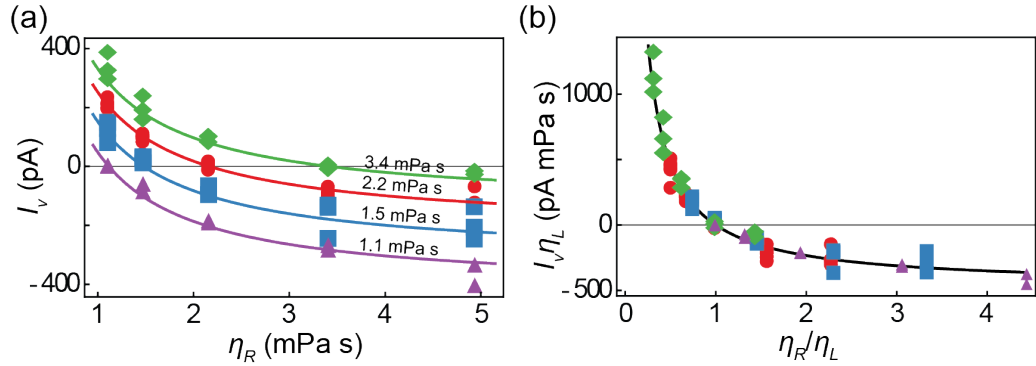


Figure 3.10: Experimental characteristics of viscophoresis. (a) Dependence of I_v on η_R for $\eta_L = 1.1$ (purple triangles), 1.5 (blue squares), 2.2 (red circles), and 3.4 mPa s (green diamonds) in a $L = 200 \mu\text{m}$ channel. Lines show equation 3.29 with $\sigma = 200 \text{ mC m}^{-2}$. (b) Dependence of $I_v \eta_L$ on η_R / η_L for the same measurements. Line shows equation 3.29 rescaled by η_L .

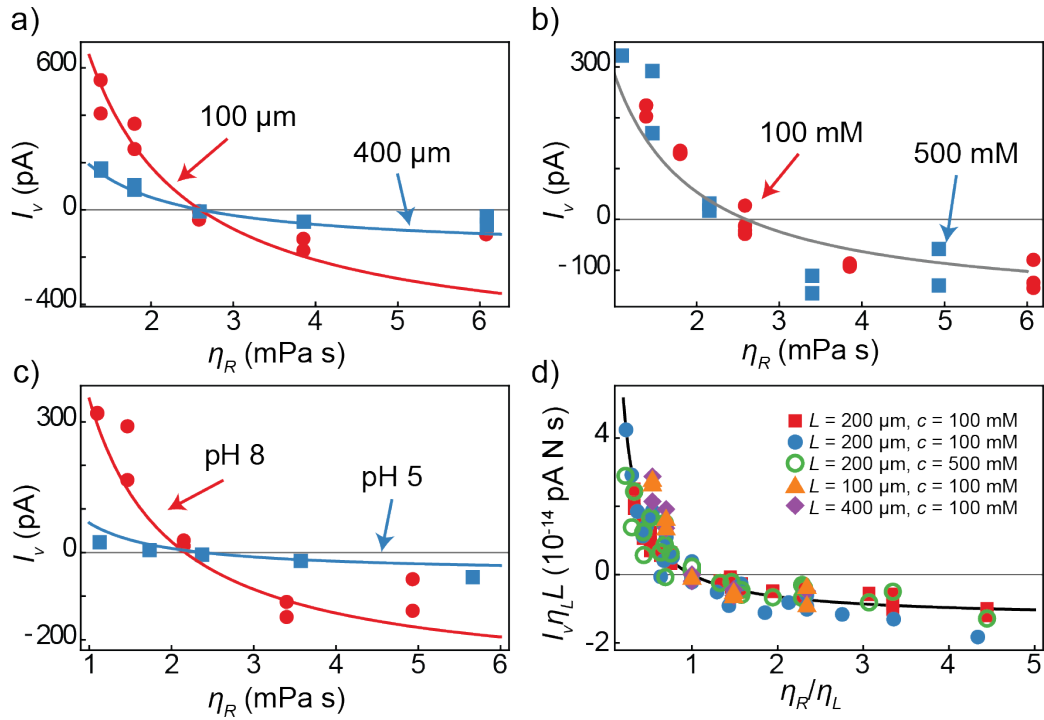


Figure 3.11: The dependence of I_v on η_R is compared a) between channels with $L = 100$ (red circles) and $400 \mu\text{m}$ (blue squares); b) between measurements at pH 8 (red circles) and pH 5 (blue squares) in a single $L = 100 \mu\text{m}$ channel; and c) between measurements at bulk KCl concentrations of 100 mM (red circles) and 500 mM (blue squares) in the same $L = 100 \mu\text{m}$ channel. In all cases $\eta_L = 2.6 \text{ mPa s}$ and the lines show fits of equation 3.29 to the data, which obtained a) $\sigma = 400 \text{ mC m}^{-2}$, b) $\sigma = 280 \text{ mC m}^{-2}$ for pH 8 and $\sigma = 50 \text{ mC m}^{-2}$ for pH 5, and c) $\sigma = 250 \text{ mC m}^{-2}$. d) Dependence $I_v \eta_L L$ on η_R / η_L for measurements performed at pH 8 using various L and KCl concentrations, as indicated. The line shows equation 3.29 rescaled by $\eta_L L$ with $\sigma = 200 \text{ mC m}^{-2}$. The experimental uncertainty in these figures is comparable to the size of the symbols.

all viscosity gradients tested.

Figure 3.11c shows the dependence of I_v on η_R from measurements on the same device but with two different KCl concentrations, 100 and 500 mM. The salt concentration had no discernible effect on I_v .

Figure 3.11d shows data from a variety of different experimental conditions plotted on the same rescaled axes. It includes data taken with 100 and with 500 mM KCl in four different devices. The devices had mixing channels with lengths $L = 100, 200,$ and $400 \mu\text{m}$. The data all collapse when the product $I_v\eta_L L$ is plotted against the viscosity ratio η_R/η_L .

3.6 Discussion

These experiments indicate that the current originates in the motion of counterions in the electric double layers near the mixing channel surfaces. Decreasing the pH of the liquid decreased the magnitude of I_v because of the lower equilibrium surface charge density of the glass and the consequently lower number of counterions. Changing the salt concentration caused no change in I_v because that bulk property of the liquid does not significantly affect the surfaces [54].

Our measurements are well described by a stochastic model based on the isothermal rule. That finding is consistent with previous measurements of colloidal particles and theoretical studies of systems coupled to a heat bath [5, 36, 58], which also point to the applicability of the isothermal rule. A particle obeying the isothermal rule drifts toward higher diffusivity with a drift speed

$$\langle \dot{x} \rangle = \frac{dD(x)}{dx}. \quad (3.17)$$

The isothermal rule also leads to a generalization of Fick's law in which the flux, J , is related to the concentration profile, $\phi(x)$, by $J(x) = -D(x)\frac{d\phi(x)}{dx}$ [31]. Thus, a uniform distribution of particles exhibits no net flux. However, the electrochemical currents we measured involve the arrival and absorption of ions at one electrode and the accompanying release of ions from the other. As explored further in chapter 4, that process shifts the distributions of ions away from uniformity and allows a flux in the steady state.

To provide intuition for the existence of drift and the absence of flux that the isothermal rule predicts in equilibrium, an analogy with sedimenting particles is sometimes invoked [58]. Particles

sedimenting in a container have a net drift due to gravity but reach a flux-less equilibrium supported by a concentration gradient. However, the boundary condition for a particle arriving at the bottom of a closed container differs fundamentally from that of an ion arriving at an electrode. For a closer analogy, a sedimenting particle should be absorbed by the bottom and a new particle released from above. That system would clearly exhibit a steady state flux related to the drift speed and mean density of the particles, $\bar{\rho}$, as $J = \langle \dot{x} \rangle \bar{\rho}$.

3.6.1 Deriving a model of I_v

We found that the currents we measured are well described by a simple model in which the positive surface counterions drift uniformly according to equation 3.17. For a uniform charge density on the walls of the rectangular mixing channel, this leads to

$$I_v = \sigma(2w + 2h) \langle \dot{x}(t) \rangle, \quad (3.18)$$

where $\langle \dot{x} \rangle$ is the counterion drift speed, w and h are the width and height of the channel, and $-\sigma$ is the average surface charge density of the channel. Using equation 3.17 along with the Stokes-Einstein relation gives,

$$I_v = -\sigma(w + h) \frac{k_B T}{3\pi r} \frac{1}{\eta^2} \frac{d\eta(x)}{dx}. \quad (3.19)$$

Now, we need to find $\eta(x)$.

Viscosity profile inside the nanofluidic mixing channel

We calculated $\eta(x)$ based on two assumptions: First, we presume, as in section 3.2.2, that the viscosity of a mixture of two liquids obeys

$$\eta(\phi) = \eta_L^{1-\phi} \eta_R^\phi, \quad (3.20)$$

where ϕ is the volume fraction of the liquid with viscosity η_g , and η_f the viscosity of the other liquid.

Second, we assume that as the molecules that comprise the liquids intermix, they execute Brownian motions with an isothermal integration rule, i.e. they obey the same equations of motion as the counterions whose currents we have measured. We showed that isothermal integration rule also

corresponds to the ‘‘Fick’’ generalization of the diffusion equation [59]

$$\frac{\partial \phi_i}{\partial t} = \frac{\partial}{\partial x} D_i(x) \frac{\partial \phi_i}{\partial x}, \quad (3.21)$$

where ϕ_i is the volume fraction of diffusing species i , and $D_i(x)$ is its local diffusion coefficient. This says that in steady state $D(x) \frac{\partial \phi}{\partial x} = D(x) \frac{\partial \phi}{\partial \eta} \frac{\partial \eta}{\partial x}$ is constant for each species. Since $D \propto 1/\eta$ according to the Stokes Einstein equation,

$$\frac{1}{\eta(x)} \frac{\partial \phi}{\partial \eta} \frac{\partial \eta}{\partial x} = \text{const}, \quad (3.22)$$

Next, we can invert equation 3.20 to find

$$\phi(\eta) = \frac{\ln \eta / \eta_f}{\ln \eta_g / \eta_f}. \quad (3.23)$$

Now we can calculate,

$$\frac{\partial \phi}{\partial \eta} = \frac{1}{\eta} \frac{1}{\ln \eta_g / \eta_f} \quad (3.24)$$

Combining this with equation 3.22 gives,

$$\frac{1}{\eta^2} \frac{\partial \eta}{\partial x} = \text{const}. \quad (3.25)$$

Integrating this and applying the boundary conditions $\eta = \eta_L$ at $x = 0$ and $\eta = \eta_R$ at $x = L$ leads to the theoretical viscosity profile inside the mixing channel

$$\eta(x) = \left[\frac{1}{\eta_L} - \frac{x}{L} \left(\frac{1}{\eta_L} - \frac{1}{\eta_R} \right) \right]^{-1}. \quad (3.26)$$

I_v as a function of η_L and η_R

Returning to equation 3.18, since $\frac{1}{\eta^2} \frac{\partial \eta}{\partial x}$ is constant, we can use its value anywhere. At $x = 0$, the value is,

$$\frac{1}{\eta^2} \frac{\partial \eta}{\partial x} = \frac{1}{\eta_L^2} \frac{\partial \eta}{\partial x} \Big|_{x=0} = \frac{1}{L} \left(\frac{1}{\eta_L} - \frac{1}{\eta_R} \right) \quad (3.27)$$

Combining equation 3.26 with equation 3.18 gives

$$I_v = -\frac{k_B T \sigma}{3\pi r} \frac{w + h}{L} \left(\frac{1}{\eta_L} - \frac{1}{\eta_R} \right). \quad (3.28)$$

For our mixing channel, $w \gg h$ so we can write

$$I_v = -\frac{k_B T \sigma w}{3\pi r L} \left(\frac{1}{\eta_L} - \frac{1}{\eta_R} \right). \quad (3.29)$$

Equation 3.29 agrees quantitatively with the data in Fig 3.10(a) with no adjustable parameters; we measured $\sigma = 200 \text{ mC m}^{-2}$ in a separate conductance saturation experiment described in section 3.3 and obtained $r = 1.25 \text{ \AA}$ from measurements of conductivity and viscosity using the Stokes-Einstein equation. Equation 3.29 also predicts the observed L -dependence in Fig 3.11(a) using $\sigma = 400 \text{ mC m}^{-2}$ for those devices, which were fabricated together. In Fig 3.11(b) we fit equation 3.29 to pH-dependent data using σ as a fitting parameter and found $\sigma = 280 \text{ mC m}^{-2}$ for pH 8 and $\sigma = 50 \text{ mC m}^{-2}$ for pH 5. As expected, the more acidic conditions lowered the surface charge density of the glass nanochannel. Equation 3.29 also predicts that I_v is independent of KCl concentration, consistent with the data in Fig 3.11(c). The data collapse in Fig 3.10(b) follows directly from equation 3.29, which gives

$$I_v \eta_L = -\frac{k_B T \sigma w}{3\pi r L} \left(1 - \frac{\eta_L}{\eta_R} \right) \quad (3.30)$$

when rescaled by η_L . Similarly, rescaling by $\eta_L L$ gives

$$I_v \eta_L L = -\frac{k_B T \sigma}{3\pi r} w \left(1 - \frac{\eta_L}{\eta_R} \right), \quad (3.31)$$

consistent with the data in Fig 3.11(d).

3.7 Other sources of current

We have excluded the possibility that the currents we measured in the above experiments result from a chemical potential gradient due to the composition of our experimental liquids, the streaming current driven by a pressure imbalance across the mixing channel, or the Bernoulli effect resulting from the differential flow speeds in our microchannels.

3.7.1 Chemical potential gradient

A gradient in the chemical potential of ions can drive a current. To eliminate this as a possible explanation for the current that we measured, we estimated the effect of a chemical potential gradient arising from the inhomogeneous solvent.

Ions in the bulk liquid

If an ion has a different solvation energy in glycerol/water than in formamide/water, there will be a chemical force acting to drive it toward a lower chemical potential and resulting in an electrical current. In particular, if K^+ has a lower solvation energy in glycerol than in formamide, a net current of these ions could flow toward regions of higher glycerol concentration. Similarly, if Cl^- has a lower solvation energy in formamide than glycerol, a net current of these ions could flow toward regions of higher formamide concentration. Furthermore, we expect a chemically-driven current to grow with the magnitude of the viscosity gradient because the viscosity gradient reflects the gradient in the chemical composition of the liquid. Therefore, a chemical potential gradient could generate a current similar to the one we have measured and attributed to the viscosity gradient. However, such a current would scale linearly with the bulk salt concentrations. In contrast, we found that the bulk KCl salt concentration had almost no effect on the measured current, so we can rule out bulk ion transport due to chemical potential gradients as the cause of the current we measured.

Surface

The bulk argument presented above does not rule out the possibility that chemical potential gradients give rise to currents in the electric double layers near surfaces. There can exist a gradient in the chemical potential of K^+ that drives it in the direction of increasing formamide content; the absence of a bulk ionic current only implies that the chemically driven motion of K^+ must be offset by an equivalent motion of Cl^- in the same direction. In the electric double layers, there is an excess of K^+ , so the motion of that ion will no longer be offset by Cl^- . We know from the absence of a bulk ionic current that K^+ and Cl^- experience the same chemical potential differences between glycerol and formamide, and we can estimate those chemical potential differences based on KCl solubilities.

The change in free energy associated with the dissolution of KCl ($KCl \rightarrow K^+ + Cl^-$) in solvent

i , ΔG_i , is

$$\Delta G_i = \mu_{0,i}^{\text{K}^+} + \mu_{0,i}^{\text{Cl}^-} - \mu_{0,i}^{\text{KCl}} + k_B T \log(C_i^{\text{K}^+} C_i^{\text{Cl}^-}), \quad (3.32)$$

where $\mu_{0,i}^x$ is the standard chemical potential of species x in solvent i , and $C_i^{\text{K}^+}$ and $C_i^{\text{Cl}^-}$ are the concentrations of K^+ and Cl^- , respectively. When the concentrations of K^+ and Cl^- are constant and equal to each other, as they are in our experiments, the change in free energy as KCl moves from glycerol to formamide, $\Delta G_{g \rightarrow f}$, is

$$\Delta G_{g \rightarrow f} = \mu_0^{K,g} + \mu_0^{\text{Cl},g} - \mu_0^{K,f} - \mu_0^{\text{Cl},f}. \quad (3.33)$$

We can relate eq. 3.33 to the solubilities of KCl in glycerol and formamide. We begin by noting that at the saturation concentration, $C_{i,\text{sat}} = C_i^{\text{K}^+} = C_i^{\text{Cl}^-}$, dissolving additional KCl does not lower the free energy, and $\Delta G_i = 0$ in eq. 3.32 implies

$$\mu_{0,i}^{\text{K}^+} + \mu_{0,i}^{\text{Cl}^-} - \mu_{0,i}^{\text{KCl}} = -k_B T \log[(C_{i,\text{sat}})^2]. \quad (3.34)$$

Combining eqs. 3.33 and 3.34 obtains

$$\Delta G_{g \rightarrow f} = \mu_{0,f}^{\text{KCl}} - \mu_{0,g}^{\text{KCl}} - 2k_B T \log\left(\frac{C_{f,\text{sat}}}{C_{g,\text{sat}}}\right). \quad (3.35)$$

Because KCl is a solid, its chemical potential cannot depend on the solvent. Therefore, $\mu_{0,f}^{\text{KCl}} = \mu_{0,g}^{\text{KCl}}$, and eq. 3.35 simplifies to

$$\Delta G_{g \rightarrow f} = 2k_B T \log\left(\frac{C_{g,\text{sat}}}{C_{f,\text{sat}}}\right). \quad (3.36)$$

The free energy change in eq. 3.36 occurs over the length of the mixing channel, so the effective force F that it exerts on salt ions inside the mixing channel is

$$F = \frac{2k_B T}{L} \log\left(\frac{C_{g,\text{sat}}}{C_{f,\text{sat}}}\right). \quad (3.37)$$

If we model the viscous drag on the ions with Stokes' drag on a sphere of radius r , the resulting drift speed is

$$v = \frac{F}{6\pi\eta r} = \frac{k_B T}{3\pi\eta r L} \log\left(\frac{C_{g,\text{sat}}}{C_{f,\text{sat}}}\right). \quad (3.38)$$

The drift of ions can result in a net current where there is an imbalance in the density of positive

and negative ions, namely, in the electric double layers near the channel surfaces. For a channel with $w \gg L$, we can neglect edge effects and approximate the current as $I = 2\sigma wv$, which is combined with eq. 3.38 to obtain

$$I = \frac{F}{6\pi\eta r} = \frac{2}{3}k_B T \frac{\sigma}{\pi\eta r} \frac{w}{L} \log\left(\frac{C_{g,sat}}{C_{f,sat}}\right). \quad (3.39)$$

The saturation concentrations for KCl in glycerol and formamide are 1106 mM and 939 mM, respectively [60, 61]. Using pure formamide and glycerol concentrations and typical parameters from our experiment ($w = 150 \mu\text{m}$, $L = 200 \mu\text{m}$, $r = 1.25 \text{ \AA}$), and the measured viscosity of an equal glycerol-formamide mixture, $\eta = 21.2 \text{ mPa}\cdot\text{s}$, gives only 8 pA. Our liquids always contained 50% water, so this represents conditions more extreme than those found in our experiments. Further, KCl is more soluble in glycerol than in formamide, meaning this effect would tend to pull ions toward the high viscosity side, opposite from what we saw in our experiments. Therefore, we conclude that chemical forces cannot account for more than a small fraction of the currents we measured.

3.7.2 Streaming current

Streaming currents are a potential alternative explanation for the currents we have measured. However, we have found that the currents do not immediately die when the microchannel flows are turned off. This observation is not consistent with streaming current.

Further, estimates of streaming current show the effect to be far too small. A measurement of streaming current in a similar glass mixing channel gives a good estimate of the magnitude. The Dekker group found a current of less than 10 pA of streaming current driven by 1 bar of pressure in a water-filled mixing channel 4.5 mm long, 50 μm wide, and 100 nm tall. Our mixing channel is 22.5 times shorter and three times wider. This results in more streaming current. It is also half as tall and has at least double the viscosity. Based on scaling, this leads to an estimate of 84 pA bar⁻¹. This means that even 100 mbar across our mixing channel could only drive 8.4 pA. This is not enough to explain the effect we have measured.

3.7.3 Bernoulli effect

The liquid viscosities in the two microchannels are different, so the flow rates through them are also different. This introduces the possibility of a pressure difference developing across the mixing channel due to the Bernoulli effect. Again, this effect would stop as soon as flow stops, but the

current we have measured persists.

An estimate of the magnitude of this effect also shows it to be far too small. Bernoulli's principle says

$$P + \frac{\rho v^2}{2} = \text{const} \quad (3.40)$$

Comparing the points at either end of the nanochannel,

$$P_L + \frac{\rho_R v_L^2}{2} = P_R + \frac{\rho_R v_R^2}{2} \quad (3.41)$$

$$P_L - P_R = \frac{1}{2} (\rho_R v_R^2 - \rho_L v_L^2) \quad (3.42)$$

The maximum flow rate in a rectangular channel of width w , height h , and length l , where $w \gg h$ is

$$u_{max} = \frac{h^2 P_a}{8\eta l}, \quad (3.43)$$

where P_a is the pressure applied to the microchannels, and η is the viscosity.

The pressure arising as a result of Bernoulli's principle is,

$$P_L - P_R = \frac{P_a h^4}{128 l^2} \left(\frac{\rho_R}{\eta_R^2} - \frac{\rho_L}{\eta_L^2} \right) \quad (3.44)$$

This amounts to about 5×10^{-11} bar. Using the above estimate of 84 pA bar^{-1} gives a minuscule current of 4.2×10^{-9} pA

3.8 Conclusion

We designed a glass nanofluidic system sensitive to a viscosity gradient driven drift which allowed us to vary the viscosity profile and net charge concentration in various ways. We concluded liquid viscosity gradients drove the surprisingly large ionic currents we measured inside our nanofluidic channels. The microscopic mechanism is the noise-induced drift of counterions obeying the isothermal rule. The electrodes also play an essential role by permitting a finite, steady-state flux in a system that would otherwise reach a homogeneous and flux-less equilibrium. This conclusion will be expanded upon in chapter 4. Transport in a viscosity gradient evidently uses the free energy of

mixing to drive transport, in contrast with other forms of noise-driven motion, like Brownian motors, which consume chemical energy to rectify thermal noise [62]. We speculate that the effect we have measured could cause significant motion within and between cells, across synthetic membranes, and within nanofluidic devices, where viscosities can vary by orders of magnitude over short distances [63]. Furthermore, even viscosity gradients over large distances might influence the distributions of hydrocarbons, sediments, and other small particles in geological systems over long timescales. Finally, the simple picture of drifting counterions we presented describes our measurements well, despite neglecting the full behavior of co- and counterions, the electro-neutrality condition, and possibly other complications. Computational methods can account for such details in biological, chemical, and other liquid systems where viscosity gradients naturally arise. It is important that they apply the isothermal rule or miss real and potentially large effects [38, 40].

Chapter 4

The mechanisms of diffusion in a viscosity gradient

We posited that the current we measured in our experiments originates in the drift of ions toward low viscosity, which is expected if the ions obey the isothermal rule. But how does that drift translate into a measurable current? That turns out to be a surprisingly subtle question because the flux of particles obeying the isothermal rule is not directly linked to the viscosity gradient. We used simulations to understand the connections between flux, drift, and viscosity.

In section 2.3, we showed the connection between the integration conventions and the generalizations of Fick's law. In chapter 3 we showed that a model based on the isothermal convention, which predicts drift according to $\langle \dot{x} \rangle = \frac{dD(x)}{dx}$, agrees nicely with our data. However, the theory based on the isothermal convention has a feature that was initially confusing. The Fokker-Planck generalization of Fick's law, which corresponds to the Itô convention, explicitly predicts flux which depends on the diffusivity gradient,

$$J = -\frac{d}{dx}D(x)\rho(x) = -\rho\frac{dD(x)}{dx} - D\frac{d\rho(x)}{dx}. \quad (4.1)$$

However, the predicted flux goes toward lower diffusivity, opposite of what we saw in our experiments. The other generalization of Fick's law,

$$J = -D(x)\frac{d\rho(x)}{dx}, \quad (4.2)$$

has no diffusivity gradient term. The presence of explicit $\frac{dD}{dx}$ in equation 4.1 but not in equation 4.2 led me to initially believe I might have reversed the leads on the ammeter, or in some other way inverted the current. Instead, as we will show below, it is possible to find flux without explicit diffusivity gradient term in equation 4.2.

The key to explaining the sustained currents in our experiments lies in the boundary conditions. Commonly, simulations of inhomogeneous diffusion are performed inside some closed domain which particles cannot enter or leave. Closed boundary conditions like this require a flux-less steady-state. Periodic conditions, which effectively connect the boundaries, have no such restriction.

4.1 Simulation design

We studied diffusion in a viscosity gradient with a simple model for the motion of particles. The basis for our model was a paper by Volpe and Wehr, which uses the stochastic differential equation [5],

$$dx_t = \sqrt{2D(x)}dW_t \equiv \sigma(x)dW_t, \quad (4.3)$$

where $dx_t = x_t - x_{t'}$ is the change in position between times t and t' , D is the diffusivity, $dW_t = W_t - W_{t'}$ is a random variable with mean zero and variance $t - t'$. In these simulations, we break the continuous path of a particle into discrete steps, x_n , occurring with a regular time interval Δt . It is convenient to use $\sigma(x) \equiv \sqrt{2D(x)}$, which represents the size of each random step. We will use a discrete form of equation 4.3,

$$\Delta x = x_{n+1} - x_n = \sigma(x)(\pm\sqrt{\Delta t}). \quad (4.4)$$

The random variable dW_t in equation 4.3 has been represented in equation 4.4 by a discrete random variable $\pm\sqrt{\Delta t}$ (where the \pm represents the random choice), which has variance Δt . We set $\Delta t = 1$ and used a spatial domain 100 units wide. Typically, in simulations like this one, when a particle would pass through a boundary at $x = 0$ or $x = 100$, it is instead reflected back into the domain [5]. Figure 4.2a shows a diagram of a particle whose final position would have sent it past the boundary by a distance a . Instead, the particle is placed a distance a inside the domain. This rule is known as a *reflective* boundary condition [5].

For a system without a diffusivity gradient, the application of equation 4.4 is uncomplicated. We

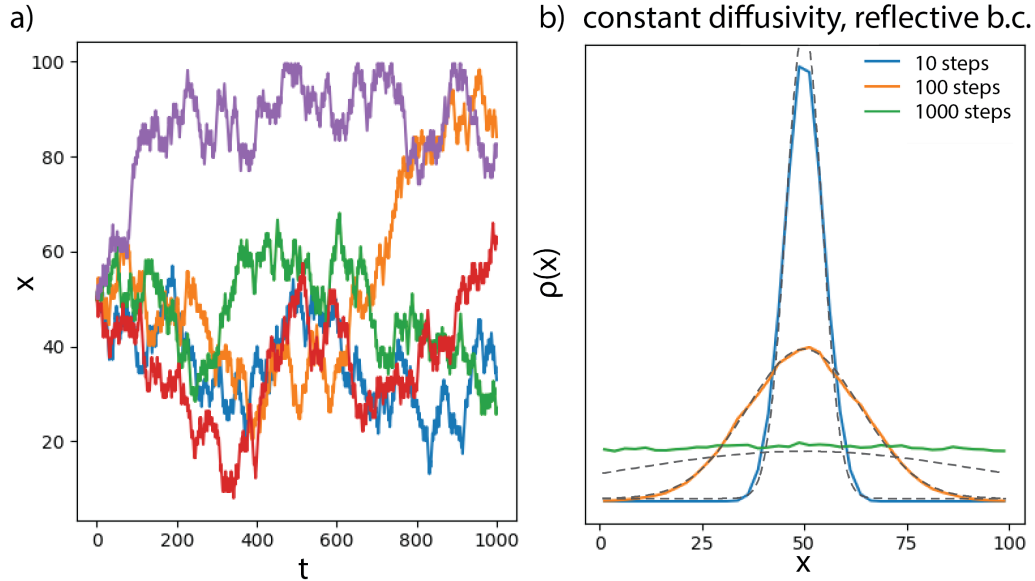


Figure 4.1: Simulated diffusion of 10^5 particles with reflective boundary conditions and spatially-constant diffusivity. a) Five sample particle trajectories. b) The distribution of particles after 10, 100, and 1000 time steps. Dashed lines show theoretical expectation according to equation 4.5.

simply generate a random choice, either $\sqrt{\Delta t}$ or $-\sqrt{\Delta t}$, multiply it by σ , add the result to x_n , and repeat.

4.1.1 Constant diffusivity

Figure 4.1a shows five sample trajectories for particles with $D = 1$. Particles are just as likely to go in either direction. The particles start tightly clustered but spread out over time. By 1000 steps, they look randomly distributed. The purple trajectory in figure 4.1a shows a particle bumping against the wall at $x = 0$.

Figure 4.1b shows the distributions of 10^5 particles with uniform diffusivity $D = 1$ after 10, 100, and 1000 time steps. The particles were released from an initially Gaussian distribution centered at $x = 50$ with a standard deviation 1. The sharply peaked distribution spreads symmetrically about $x = 50$, relaxing to a half-max width of about 10 after 10 time steps and 35 after 100 steps. By step 1000, the distribution was nearly flat. We compared the simulated distributions with the analytic solution for point-source free diffusion: a Gaussian function whose width increases with time,

$$\rho(x, t) = \frac{N}{\sqrt{4\pi Dt}} e^{-x^2/4Dt}, \quad (4.5)$$

where N is the number of particles [21]. Our simulation matches equation 4.5 well after 10 and 100 steps, but shows an overabundance of particles everywhere after 1000 steps. This is because equation 4.5 is a solution for diffusion in free space, but our simulation will not let particles leave the domain.

4.1.2 Diffusivity gradient

Introducing a diffusivity gradient complicates the model in an important way. Each particle begins a step at a position x_n and ends at x_{n+1} so we have to choose where in that interval to evaluate function $\sigma(x)$; any location from x_n to x_{n+1} is equally valid. We could use the Itô convention, evaluating the diffusivity at the beginning of the step:

$$x_{n+1} = x_n \pm \sigma(x_n)\sqrt{\Delta t}. \quad (4.6)$$

We could use the Stratonovich convention, evaluating the diffusivity in the middle of the step:

$$x_{n+1} = x_n \pm \sigma\left(\frac{x_{n+1} + x_n}{2}\right)\sqrt{\Delta t}. \quad (4.7)$$

Finally, we could use the isothermal convention, evaluating it at the end:

$$x_{n+1} = x_n \pm \sigma(x_{n+1})\sqrt{\Delta t}. \quad (4.8)$$

The Itô convention, represented by equation 4.6, is the easiest to implement in a simulation because we know the current position of each particle and can straightforwardly compute the value of $\sigma(x_n)$. Equations 4.7 and 4.8 present an apparent catch-22. They require us to know where the particle will land to find the step size, but, of course, we must know the step size to compute where the particle will land. We will show how to find x_{n+1} in a self-consistent manner by first noting that equations 4.6, 4.7, and 4.8 can be expressed as special cases of a more general equation in which a continuous parameter α represents the choice of where to evaluate $\sigma(x)$,

$$x_{n+1} = x_n \pm \sigma(x_n + \alpha\Delta x)\sqrt{\Delta t}. \quad (4.9)$$

The parameter α runs from 0 to 1, and equations 4.6, 4.7, and 4.8 are special cases with $\alpha = 0$,

1/2, and 1 respectively. We Taylor expand equation 4.9 to first order about the point x_n to find an equation for x_{n+1} based on x_n and the gradient in the diffusivity,

$$\sigma(x_n + \alpha\Delta x) \approx \sigma(x_n) + \alpha \frac{d\sigma(x)}{dx} \Delta x. \quad (4.10)$$

Substituting in equation 4.4 gives

$$\sigma(x_n + \alpha\Delta x) \approx \sigma(x_n) \pm \alpha \sigma(x_n) \frac{d\sigma(x_n)}{dx} \sqrt{\Delta t} \quad (4.11)$$

and applying to equation 4.9 gives a way to calculate x_{n+1} in terms of x_n for any value of α ,

$$x_{n+1} = x_n + \alpha \sigma(x_n) \frac{d\sigma(x_n)}{dx} \delta t \pm \sigma(x_n) \sqrt{\delta t}. \quad (4.12)$$

In terms of $D(x)$, this would be,

$$x_{n+1} = x_n + \alpha \frac{dD(x_n)}{dx} \delta t \pm \sqrt{2D(x_n)} \delta t. \quad (4.13)$$

Consider a step subject to the isothermal rule as given by equation 4.9 with $\alpha = 1$. The diffusive third term in equation 4.9 updates the position based on $\sigma(x_n)$, as prescribed by the Itô convention. By adding the second term, sometimes called the *spurious* or *noise-induced* drift, we recover the results of the isothermal convention [32, 5, 31]. In other words, a trajectory in the isothermal convention is equivalent to one in the Itô convention with an added drift term [5, 31].

4.2 Results of simulations with diffusivity gradients

4.2.1 Using reflective boundary conditions

Our first goal was to replicate Wehr and Volpe's simulations [5]. In their paper, they studied the Itô, Stratonovich, and isothermal integration conventions using simulations and demonstrated how this choice affects the steady-state particle distribution, finding a monotonically decreasing particle density when using the Itô convention, and a flat one when using the isothermal convention. Figure 4.4, from Volpe and Wehr's paper, shows $\sigma(x)$ (a,d,g), a sample particle trajectory (b,e,h), and the time evolution of the particle distributions (c,f,i) they simulated for different values of α .

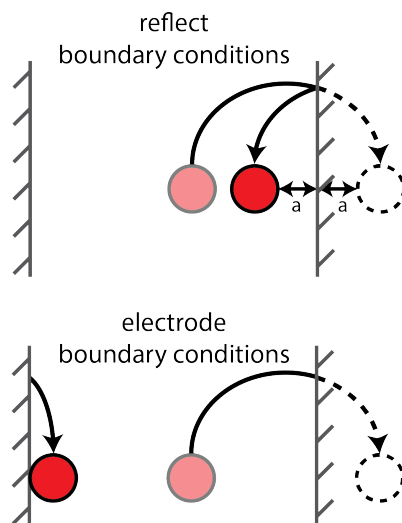


Figure 4.2: a) A particle hopping into a reflective boundary condition. b) A particle hopping into a boundary condition designed to emulate an electrode.

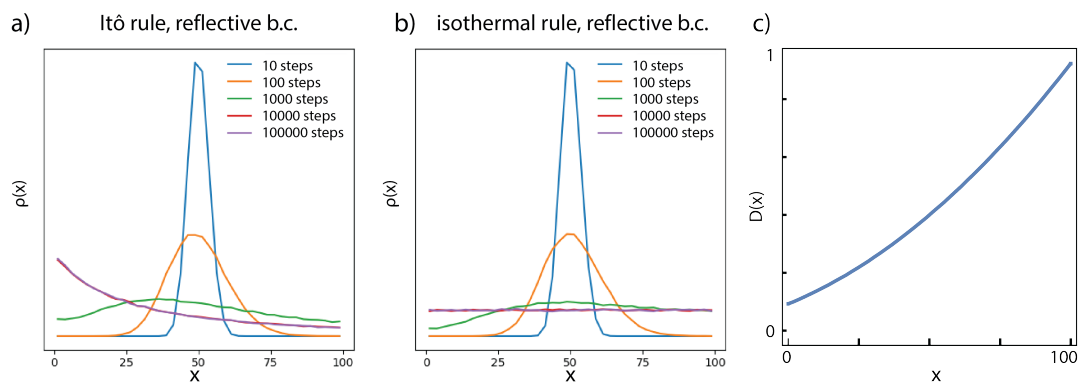


Figure 4.3: Simulated diffusion of 10^5 particles with reflective boundary conditions using different integration conventions. Evolution of the particle distribution using a) the Itô convention and b) the isothermal convention. c) Diffusivity as a function of x .

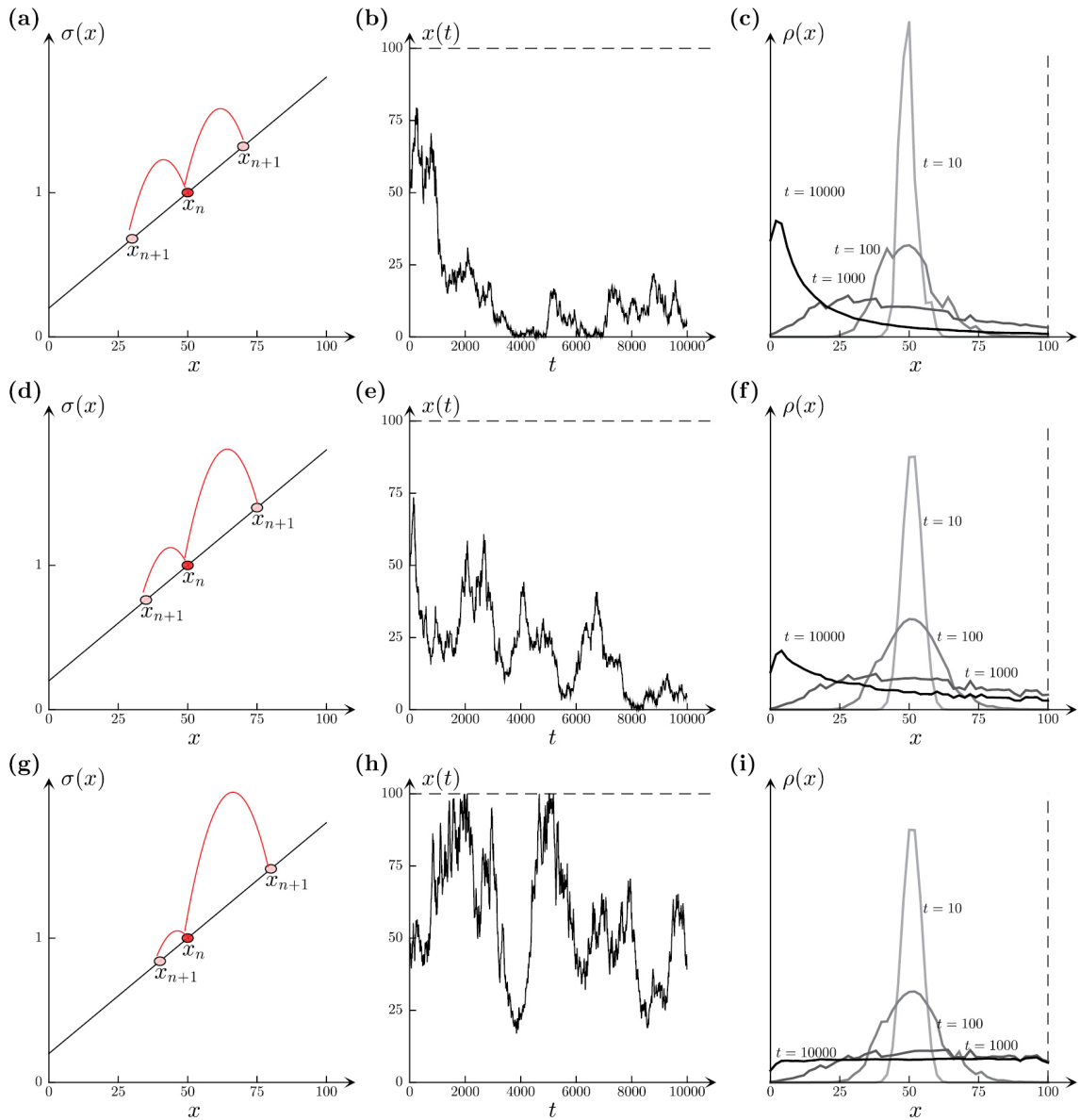


Figure 4.4: Evolution of the random walker with multiplicative noise for various values of α . (a) For $\alpha = 0$, the amplitude of each random step is a function of the initial state and is therefore symmetrically distributed; (b) example of a trajectory in state space; (c) probability density of the distributions at selected times. The corresponding results for $\alpha = 0.5$ and $\alpha = 1$ are shown in ((d)–(f)) and ((g)–(i)), respectively. In all cases, reflecting boundary conditions are imposed at $x = 0$ and $x = 100$. Note that the steady-state probability distribution is uniform only in the $\alpha = 1$ case, while in the other two cases it is peaked in the low-noise (small $\sigma(x)$) region. The steady-state probability distributions are calculated from 100 000 simulated trajectories. Figure and caption by Volpe and Wehr [5].

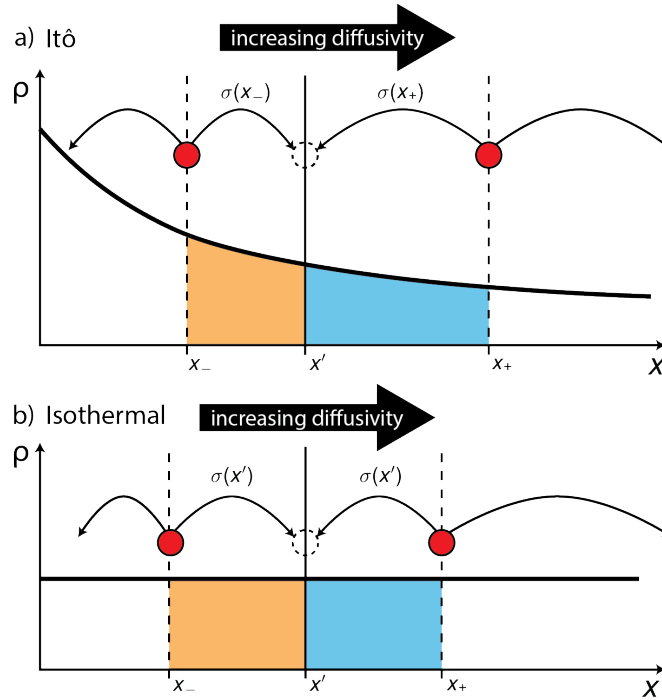


Figure 4.5: Simulated equilibrium particle densities in the a) Itô convention and b) isothermal convention. Dotted lines show the farthest positions, x_+ and x_- , from which particles can cross a test point, x' , from the left and right respectively. The areas of the shaded regions below the curve are proportional to the approximate number of particles that can cross x' from the left (orange) and the right (blue) in one step.

We set all simulation parameters to match those of Volpe and Wehr's [5]. Importantly, we used the same *reflective* boundary condition shown in figure 4.2 that Volpe and Wehr did. The simulation contains 10^5 particles with an initial Gaussian distribution with mean 50 and standard deviation 1 at intervals up to 10^6 time steps, enough to reach steady state. Figure 4.3c shows the diffusivity function used in the simulation. It corresponds to $\sigma(x) = 0.2 + 0.02x$, a formula estimated from figures 4.4a, d, and g [5].

Our results closely match Volpe and Wehr's. Figure 4.3a shows the distribution of particles in a simulation of diffusion using the Itô convention. After 10 and 100 steps, the initial distributions widened and skewed slightly to the left. By $t = 10^3$, the tails of the distribution reached the boundaries, and the distribution is skewed noticeably left. It is clear the system has reached steady state by 10^4 steps because no further change is visible by 10^5 steps. Particles have piled up against the left boundary. Once the steady state was reached, we measured no significant flux across $x = 50$.

Likewise, the figure 4.3b simulates diffusion under the $\alpha = 1$ or isothermal convention. The distributions look roughly Gaussian until step after 10^1 and 10^2 steps. After 10^3 steps, the distribution has reached the boundary at $x = 100$, but not the one at $x = 0$. By 10^4 steps, the system reached a steady state with a flat ion distribution and no significant flux through $x = 50$.

The lack of flux in these cases is not a surprise. In a closed container like the one simulated here, flux cannot exist anywhere in steady state. This constraint, along with spatial differences in hop length, allows us to understand the asymmetric steady state distribution resulting from the Itô rule in figure 4.3a, as well as the flat distribution resulting from the isothermal rule in figure 4.3b. Figure 4.5a shows, for an arbitrary test point x' , the farthest points to the left and right from which particles are capable of hopping to or past x' for the Itô convention. The region on the right is always larger than that on the left because the diffusivity increases toward the right so hops originating from that direction are longer. Figure 4.5a also shows the equilibrium particle distribution, as calculated by our simulation and shown in figure 4.3a. The regions under the ρ curve shaded with orange and blue and are proportional to the number of particles that can possibly pass x' from the left and right respectively. Since particles jump left and right with equal probabilities in our model, the areas of these regions are proportional to the average number of particles that will cross x' in each direction in a given time step. Any difference in these areas indicates that a net flux will flow away from the larger region. The system must reach an equilibrium where the particle distribution always decreases toward the right in a way that compensates for the difference in hop length and brings the shaded areas into equality.

Figure 4.5b again shows the region to the left and right of an arbitrary point x' inside which particles are capable of hopping past x' , but this time for the isothermal rule. The hop lengths are based on the hop's end position, so the size of these regions is equal. In this closed system, the flux must eventually reach zero everywhere. For the shaded regions to be equal for every choice of x' , the equilibrium distribution must be flat, which is what we see in figure 4.3b. Equation 4.12 suggests another perspective from which to view the isothermal convention of stochastic motion. As hopping with hop-length determined by the starting position, with a superimposed drift proportional to the gradient in the diffusivity.

In this simulation, we have drift but no flux. The situation is analogous to particles sedimenting in a closed container. Each particle experiences a net downward drift due to gravity. The drift causes a flux until a reverse concentration gradient builds up, matching gravity with a statistical

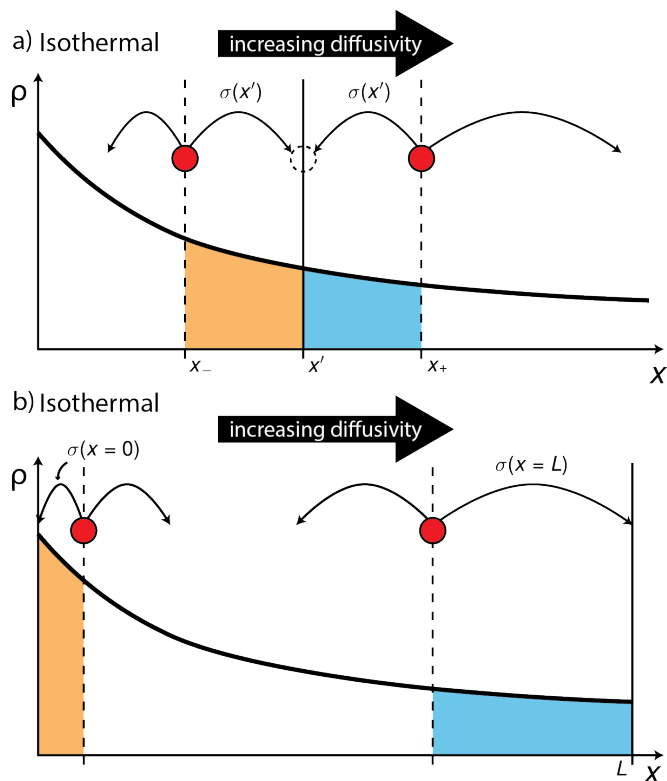


Figure 4.6: Simulated equilibrium particle density in the isothermal convention with electrode boundary conditions. a) Dotted lines show farthest positions from which particles can reach or cross a test point, x' , from the left and right. The areas of the shaded regions are proportional to the number of particles that can reach or cross x' from the left (orange) or right (blue) in one step. b) Dotted lines show the farthest positions from which particles can reach or cross the boundaries at $L = 0$ and $L = 100$. Area of the shaded regions is proportional the number of particles with a chance to hit the boundary at $x = 0$ (orange) or $x = 100$ (blue) in one step.

upward migration. Here, the drift is not countered by a concentration gradient, but instead by a gradient in hop length.

4.2.2 Using electrode boundary conditions

The reflective boundary conditions used above are a poor model for our experiment, where electrodes at either end of the mixing channel can absorb and emit ions instead of reflecting them. When an ion in a nanochannel arrives at an electrode it can be absorbed and effectively re-emitted at the opposite electrode. This wraps the domain into a circle and breaks the requirement that the flux be zero. We studied the following boundary condition to better model electrodes. Any particle that would pass a boundary in the simulation is counted and moved to the opposite boundary. Figure 4.2b illustrates

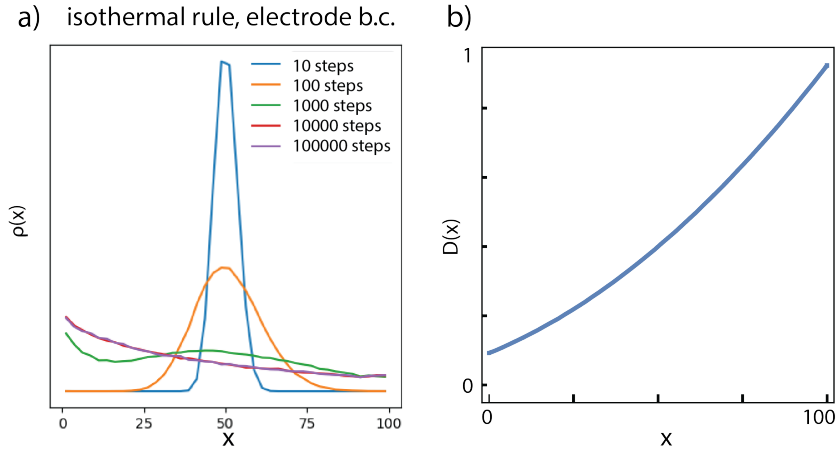


Figure 4.7: Simulated diffusion of 10^5 particles with electrode boundary conditions using the isothermal convention. a) Evolution of the particle distribution. b) Diffusivity as a function of x .

a particle that would hop past the boundary instead being placed inside the domain at the opposite boundary. The result is a steady state flux and a non-uniform particle distribution.

Figure 4.7a shows the evolution of the simulated particles distribution using the isothermal convention. This simulation was the same as the one in figure 4.3b, but with the electrode boundary conditions described above. Figure 4.7b shows the diffusivity function used in the simulation. By step 10^4 , the system reached steady state. This time, the distribution is not flat. The concentration is highest on the left and decreases monotonically to the right. Figure 4.6a illustrates the regions in which particles can reach or pass x' in one step, along with the distribution of particles found in the isothermal experiment with electrode boundary conditions. The left shaded region under the curve is larger than the right shaded region, meaning that we expect net right-ward flux. In steady-state, this flux must be constant for every choice of x' , including at the boundaries. This constraint determines the magnitude of the flux. Figure 4.6b shows the regions inside which particles can reach the boundaries at $L = 0$ and $L = 100$. The difference in the areas of these regions represents the flux through the boundary, which must be equal to the flux everywhere else in steady state.

Returning to the sedimentation analogy, isothermal diffusion with electrode boundary conditions is like sedimentation in an infinite container. The concentration gradient doesn't build up and steady-state flux can exist.

4.3 Mathematical analysis of the toy model

The toy model represented in this simulation is simple enough that we can analytically approximate $\rho(x)$ for the isothermal rule. We can estimate the flux through a point x' by calculating the number of particles on the left and right with a chance to hop past x' . Turning this into a differential equation, we can solve for the steady-state particle distributions with the *reflective* and *electrode* boundary conditions.

We can estimate the flux in the isothermal convention by looking at figure 4.6a,

$$J = \frac{1}{2} [\rho(x' - \sigma_l/2)\sigma_l - \rho(x' + \sigma_r/2)\sigma_r], \quad (4.14)$$

where $\rho(x)$ is the particle density at x . The length of a hop arriving at x' , $\sigma(x')$, is also the width of the regions to the left and right where particles can pass x' , and $\rho(x' - \sigma(x')/2)$ and $\rho(x' + \sigma(x')/2)$ are midpoint estimates of the particle densities there. Multiplying the width by ρ gives the approximate number of particles that can pass x' from either side, and the factor of $\frac{1}{2}$ reflects the fact that only half of the particles that *can* cross x' will because the other half will hop in the wrong direction. We can insert the finite difference approximation

$$\frac{d\rho}{dx} = \frac{\rho(x + \sigma/2) - \rho(x - \sigma/2)}{\sigma} \quad (4.15)$$

and obtain the same generalization of Fick's law shown in equation 4.2,

$$J = -\frac{\sigma^2}{2} \frac{d\rho}{dx} = -D \frac{d\rho}{dx}. \quad (4.16)$$

It is nice to see the toy model replicate this.

Inserting a linear function (like the one used by Volpe and Wehr [5]), $\sigma(x) = \sigma_0 + x\sigma'$, we can solve for the particle density profile, $\rho(x)$. We get a differential equation,

$$\frac{d\rho}{dx} = -\frac{2J}{\sigma_0 + x\sigma'}. \quad (4.17)$$

In steady state, J should be constant in space. This leads to a solution,

$$\rho(x) = \frac{2J}{\sigma'(\sigma_0 + x\sigma')} + c. \quad (4.18)$$

The flux should also be consistent at the boundaries. The number of particles exiting at the right less the number exiting on the left should equal J . With reflective boundary conditions, J must be zero, and $\rho(x)$ must be constant:

$$\rho(x) = \frac{N}{L}, \quad (4.19)$$

where N is the number of particles in the simulation and L is the size of the domain of the simulation.

With electrode boundary conditions, the numbers exiting right and left will depend on the densities $\rho(0)$ and $\rho(L)$, and the hop lengths $\sigma(0)$ and $\sigma(L)$. We can express this as

$$J = \frac{1}{2} [\rho(L)\sigma(L) - \rho(0)\sigma(0)]. \quad (4.20)$$

Combining equation 4.18 and equation 4.20 gives,

$$J = \frac{1}{2} cL\sigma'. \quad (4.21)$$

This lets us replace the constant in equation 4.18,

$$\rho(x) = \frac{2J}{\sigma'(\sigma_0 + x\sigma')} + \frac{2J}{L\sigma'}. \quad (4.22)$$

We can apply a normalization to find J as a function of the number of particles, N . Defining,

$$\int_0^L \rho(x) dx = N, \quad (4.23)$$

we get,

$$\rho(x) = \frac{N}{L} \frac{\sigma'(L + \sigma(x))}{\sigma(x)(\ln(\sigma(x)/\sigma_0) + \sigma')} \quad (4.24)$$

Figure 4.8 shows the simulation plotted in figure 4.7a, along with equation 4.24. The solution we found has a similar shape to the steady state distribution from the simulation but predicts a higher density near $x = 0$ than we found. We have not yet found a good explanation for this discrepancy.

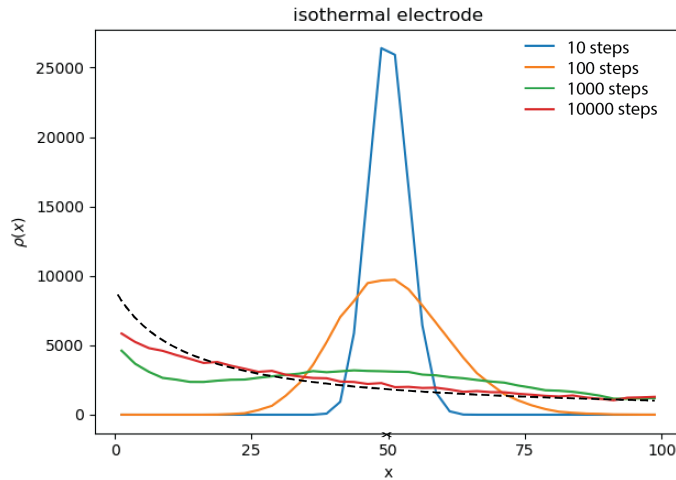


Figure 4.8: a) Simulated distribution of 10^5 particles relaxing from peaked distribution to steady state distribution using the isothermal convention and electrode boundary conditions. Dashed line shows

4.4 Comparison with experiment

Our simulations show the effects of integration convention and boundary conditions, but how do they compare to our experiments? We performed simulations to qualitatively match our experiments. In those experiments, we varied the viscosity on both sides of our nanochannel, the length of our nanochannel, the pH of the solution, and the bulk salt concentration.

In the simulations that follow, we tried to match the features of our experiments more closely. We only used the isothermal integration rule and electrode boundary conditions. In the simulations discussed above, we used linear functions for $\sigma(x)$ to match the conditions used by Volpe and Wehr [5]. In the simulations presented below, we match the steady state viscosity profile we found in equation 3.26, which corresponds to a linear diffusivity gradient. We used a flat initial particle distribution to hasten the arrival at steady state.

The result, we noticed, was that the simulator would immediately register flux at the boundaries, but no flux at the center. After a long delay, the flux at the center would catch up. Figure 4.9a shows the evolution of a flat particle distribution toward steady state. The initially flat distribution at $x = L/2$ explains the lack of flux there. The gradient in $\rho(x)$ seems to build in from the boundaries. Figure 4.9b shows the absolute difference between the center and boundary fluxes (as a fraction of the boundary flux) for a range of times as the system approaches steady state. Two different simulations

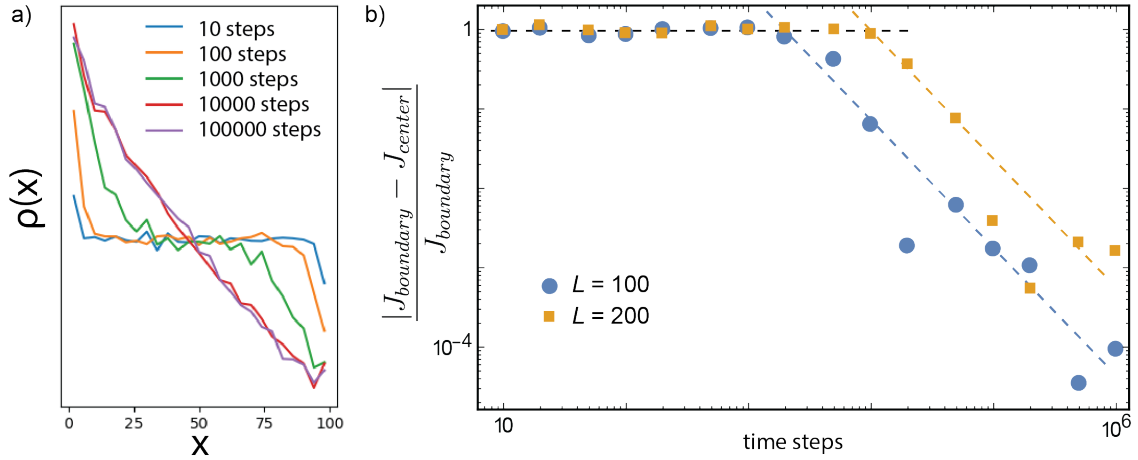


Figure 4.9: a) The evolution of an initially flat particle distribution with the isothermal rule and electrode boundary conditions. b) The fractional absolute difference in flux at the center and at the boundaries for simulations with domain sizes of 100 and 200.

are shown, with domain sizes of 100 and 200. At first, the fractional absolute flux difference is 1, because all of the flux is at the boundary. At about step 2000 for the $L = 100$ simulation and step 10 000 for the $L = 200$ simulation, the difference starts to drop. Eventually, the difference becomes negligible as the fluxes converge to the same number, once the system is in steady state. We used analysis like this to guide the lengths of our simulations.

To compare with our viscosity-varying experiments, we performed simulations with a variety of diffusivity profiles. We simulated 10^5 particles according to the isothermal rule for 2×10^5 times steps, counting flux for the last 5×10^4 steps. Once the system reached equilibrium, we started counting the flux at the boundaries and at $x = L/2$, where L is the size of the simulation domain.

Figure 4.10a shows the simulated flux as a function of the inverse diffusivity at $x = L$ with the viscosity at $x = 0$ fixed at $\eta(x = 0) = 10$. Figure 4.10b shows the diffusivity profiles used for each data point. We have used inverse diffusivity as the independent variable here to represent viscosity and make the plot easily comparable to figure 3.10a. The similarities are clear: ions flow toward lower viscosity with the curve flattening out at higher values of η_R or $\eta(x = L)$.

Figure 4.11a shows the simulated flux as a function of the simulation domain size. The the particle number density, N/L , and diffusivities at the boundaries, $D(x = 0)$ and $D(x = L)$ were kept constant. Figure 4.11b shows the diffusivity gradients used, where the color corresponds to the color of the data points in figure 4.11a. As the domain gets longer, the gradient decreases and so does the drift speed. The dotted line in figure 4.11a shows the expected flux dependence, $1/L$. This

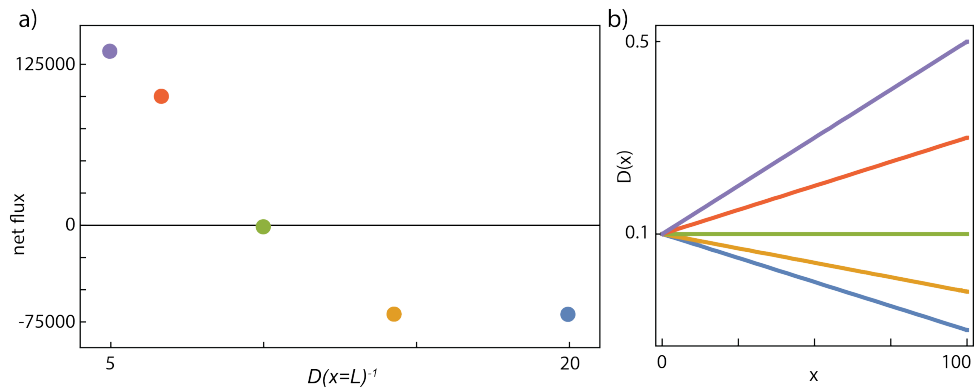


Figure 4.10: Flux in simulations with several diffusivity ratios using the isothermal rule and electrode boundary conditions. a) Dependence of flux on $D(x = L)^{-1}$. b) Diffusivity profiles, color coded to match points in (a).

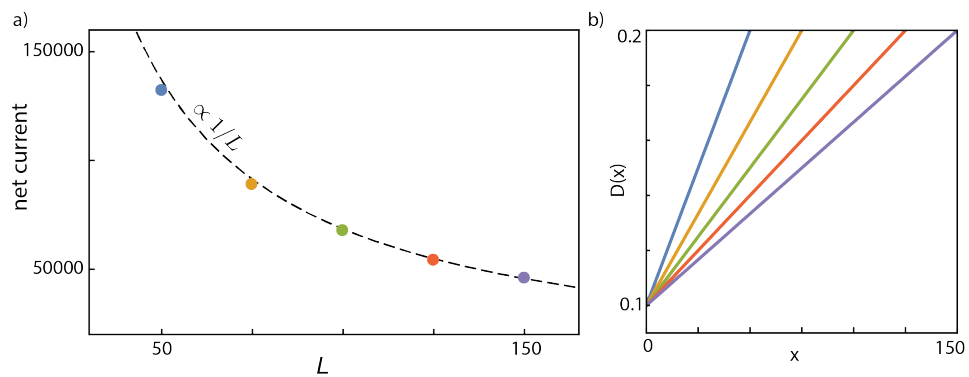


Figure 4.11: Flux in simulations with several domain lengths using the isothermal rule and electrode boundary conditions. a) Dependence of flux on L . b) Diffusivity profiles, color coded to match points in (a).

dependence matches equation 3.29.

4.5 Alternate derivation of $\eta(x)$ and interpretation of drift

At present, we have not measured the viscosity profile between the two ends of the channel. In section 3.2.3, we presented a model for $\eta(x)$, which we used to build a quantitative theoretical model of the viscosity gradient driven ionic current. Here, we present a more sophisticated model which arrives at the same results and suggests an alternate interpretation of the ionic currents we measured and described in chapter 3. In chapter 5, we will discuss an experiment which could in the future provide a measurement of the viscosity profile.

The Maxwell-Stefan theory of diffusion applies to systems with n components of any concentration [57]. Thermodynamic interactions for each species i , represented by a gradients in a chemical potential, $\nabla\mu_i$, are balanced by friction with each other species, j , based on the velocity difference, $\vec{v}_i - \vec{v}_j$ and the mole fractions of those species, ϕ_j ,

$$\frac{\phi_i}{k_B T} \nabla_{(T,p)} \mu_i = \sum_{j=1}^n \Gamma_{ij} \nabla \phi_j = - \sum_{j=1}^n \frac{\phi_i \phi_j}{D_{ij}} (\vec{v}_i - \vec{v}_j). \quad (4.25)$$

Here, $k_B T$ is the thermal energy, D_{ij} are the Maxwell-Stefan diffusivities which can be interpreted as inverse of the drag coefficients between species i and j , and Γ_{ij} is related to the activity coefficients γ_i by $\Gamma_{ij} = \delta_{ij} + \phi_i \frac{\partial \log \gamma_i}{\partial \phi_j}$.

Here, the chemical potential gradients could include contributions from the chemical interactions between the species. In our experiments, we took steps to minimize enthalpic chemical potential gradients for salt ions within our channels, so that only the entropic free energy of mixing would be important. We also used miscible solvents that we approximate to be an ideal mixture, with activity coefficients all equal to 1. In this idealized, one-dimensional situation, equation 4.25 simplifies to

$$\sum_{j=1}^n \frac{\partial \phi_i}{\partial x} = - \sum_{j=1}^n \frac{\phi_i \phi_j}{D_{ij}} (\vec{v}_i - \vec{v}_j). \quad (4.26)$$

Considering a channel filled with a binary mixture of liquids A and B , where the composition at the ends of the channel are maintained at pure A and pure B . The diffusivities of the pure liquids A and B are D_A and D_B , respectively. We will use the same simple model for diffusivity as a function

of composition as we did in section 3.2.3 [56, 64]

$$D_{AB}(\phi_A, \phi_B) = (D_A)^{\phi_A} (D_B)^{\phi_B}. \quad (4.27)$$

Now, we can write equation 4.26 for each equation,

$$\begin{aligned} \frac{d\phi_A}{dx} &= -\frac{\phi_A \phi_B}{D_{AB}} (v_A - v_B) \\ \frac{d\phi_B}{dx} &= -\frac{\phi_A \phi_B}{D_{AB}} (v_B - v_A) \end{aligned} \quad (4.28)$$

The continuity condition for each component gives

$$\begin{aligned} \frac{d}{dx}(\phi_A v_A) &= 0 \rightarrow \phi_A v_A = J_A \\ \frac{d}{dx}(\phi_B v_B) &= 0 \rightarrow \phi_B v_B = J_B \end{aligned} \quad (4.29)$$

where J_A and J_B are the steady-state fluxes of species A and B , respectively. The conservation of total liquid inside the channel also gives a condition

$$\phi_A + \phi_B = 1$$

Now using equation 4.27 with equations 4.28 gives

$$\begin{aligned} \frac{d\phi_A}{dx} &= -\frac{\phi_A \phi_B}{D_A^{\phi_A} D_B^{\phi_B}} (v_A - v_B) \\ \frac{d\phi_B}{dx} &= -\frac{\phi_A \phi_B}{D_A^{\phi_A} D_B^{\phi_B}} (v_B - v_A) \end{aligned}$$

Using the continuity equations and the conservation of total liquid equations, we can eliminate the velocities and ϕ_B to give

$$\frac{d\phi_A}{dx} = -\frac{\phi_A(1-\phi_A)}{D_A^{\phi_A} D_B^{1-\phi_A}} \left(\frac{J_A}{\phi_A} - \frac{J_B}{1-\phi_A} \right).$$

Simplifying,

$$D_A^{\phi_A} D_B^{1-\phi_A} \frac{d\phi_A}{dx} = (J_A + J_B)\phi_A - J_A.$$

In the equation above, $J_0 \equiv J_A + J_B$ is the net flow of fluid in the channel. Considering the

situation where there is no flow,

$$D_A^{\phi_A} D_B^{1-\phi_A} \frac{d\phi_A}{dx} = -J_A.$$

We can solve this equation by first taking the logarithm of both sides

$$\phi_A \log D_A + (1 - \phi_A) \log D_B + \log \frac{d\phi_A}{dx} = \log -J_A$$

Simplifying,

$$\phi_A \log \frac{D_A}{D_B} + \log \frac{d\phi_A}{dx} = \log \frac{-J_A}{D_B}$$

Making the replacement $\alpha \equiv \log \frac{D_A}{D_B}$ and exponentiating gives,

$$e^{\alpha\phi_A} \frac{d\phi_A}{dx} = -\frac{J_A}{D_B}$$

We can integrate the above expression and solve for ϕ_A

$$\int e^{\alpha\phi_A} d\phi_A = -\frac{J_A}{D_B} \int dx$$

$$\frac{1}{\alpha} e^{\alpha\phi_A} d\phi_A = C - \frac{J_A}{D_B} x$$

$$\phi_A = \frac{1}{\alpha} \log \left(\alpha C - \frac{\alpha J_A}{D_B} x \right)$$

We will use the boundary conditions $\phi_A(0) = 1$ and $\phi_A(L) = 0$,

$$1 = \frac{1}{\alpha} \log(\alpha C) \rightarrow \alpha C = \frac{D_A}{D_B},$$

$$0 = \frac{1}{\alpha} \log \left(\frac{D_A}{D_B} - \frac{\alpha J_A}{D_B} L \right) \rightarrow \alpha J_A = \frac{D_A - D_B}{L}$$

Now, we have the steady-state concentration profile

$$\phi_A(x) = \frac{1}{\log \frac{D_A}{D_B}} \log \left(D_A - \frac{x}{L} (D_A - D_B) \right) - \frac{1}{\log \frac{D_A}{D_B}} \log D_B.$$

We can use equation 4.27 to translate this into a diffusivity profile. It is helpful to start by taking

the logarithm of equation 4.27,

$$\log D_{AB}(x) = \phi_A \log D_A + (1 - \phi_A) \log D_B$$

$$\log D_{AB}(x) = \phi_A \log \frac{D_A}{D_B} + \log D_B$$

Now inserting the solution for ϕ_A and simplifying gives

$$\log D_{AB}(x) = \log \left(D_A - \frac{x}{L} (D_A - D_B) \right)$$

$$D_{AB}(x) = D_A - \frac{x}{L} (D_A - D_B)$$

To convert the diffusivity profile into the viscosity profile $\eta(x)$, we use Stokes-Einstein relation $D \propto \eta$

$$\eta(x) = \left[\frac{1}{\eta_A} - \frac{x}{L} \left(\frac{1}{\eta_A} - \frac{1}{\eta_B} \right) \right]^{-1}.$$

This is the same expression for the viscosity profile that we found in section 3.2.3.

This picture suggests another interpretation of the currents we described in chapter 3, as the result of differential drag from the intermixing glycerol and formamide. In the Maxwell-Stefan theory, particles feel a drag force from each species. As the glycerol and formamide intermix, they flow in opposite directions in the mixing channel. The positive counterions feel different drag forces from these two species. The drag forces on them will equal zero only when the drift speed of the ions, v_i , satisfies

$$\frac{\phi_f}{D_{fi}}(v_i - v_f) = \frac{\phi_g}{D_{gi}}(v_i - v_g). \quad (4.30)$$

In this interpretation, there is no mystery where the energy to drive the current comes from: It comes from the free energy of mixing.

4.6 Conclusion

Toy models and simulations have illuminated the mechanisms of diffusion in a gradient of liquid viscosity. The boundary conditions turned out to be essential. The reflective boundary conditions simulate a closed container and make it impossible for steady-state flux to exist. The electrode boundary conditions simulate electrodes which can absorb and re-emit ions, and allow steady-state

flux. Using the isothermal convention, particle drift toward lower viscosity leads to a flux, which qualitatively matches those in our experiments. A second approach to calculating $\eta(x)$ agreed with our calculation in section 3.2.3 and suggested an alternate interpretation of the current.

Chapter 5

Optical measurements of the drift of quantum dots

5.1 Introduction

Tracking particles in fluidic systems is a common technique [65]. Modern imaging systems and data analysis tools make it possible to configure a microscope to resolve small particles, identify them in images, and reconstruct their time-dependent paths. Single DNA molecules, for example, can be stained with a fluorescent dye and easily tracked in microfluidic systems [66]. Methods like this, sometimes called *particle tracking velocimetry* (PTV) or just *single particle tracking* (SPT), can be a powerful tool for quantifying diffusive systems [66, 67]. By analyzing the path of a particle, it is possible to calculate its diffusivity and detect any systematic drift in its motion [68].

In chapter 1, we reviewed several experiments which used optical means to attack the problem of diffusion in a diffusivity gradient. One used total internal reflection microscopy (TIRM) to measure motion normal to a solid surface, while another measured motion parallel to the surface [3, 36]. In both of those, the experimenters observed the drift particles with diameters of about $1\ \mu\text{m}$ in the steep but short range gradient in effective diffusivity caused by viscous coupling to a solid surface. Another experiment used a flatbed scanner to track the evolution of the distribution of dye, which is composed of organic molecules [4]. Individual dye molecules are not resolvable on a flatbed scanner, so only the collective behavior was obtained.

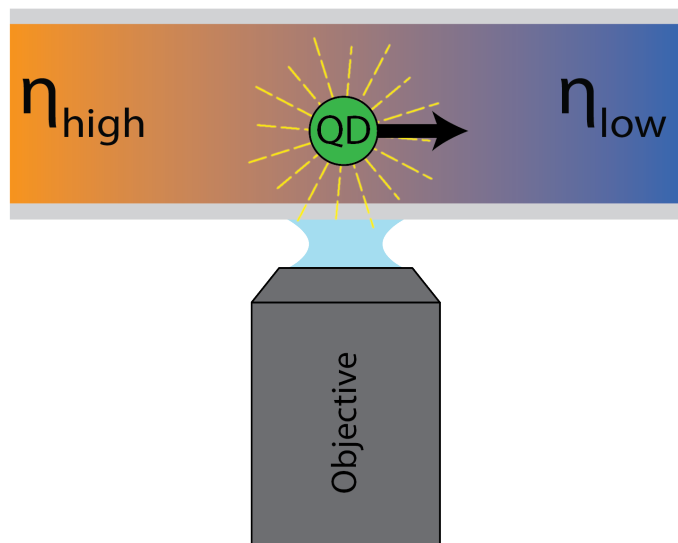


Figure 5.1: An illustration of a fluorescing quantum dot, imaged by a microscope drifting in a liquid viscosity gradient.

Quantum dots, tiny crystals on the 10 nm scale which fluoresce when exposed to ultraviolet light, provide some benefits over micron-sized colloidal particles and dye molecules. They are tiny, smaller than some molecules, which means they diffuse rapidly. Unlike dye molecules, however, they can be made to fluoresce. This means that they can be detected individually by a microscope despite the fact that their size is below the diffraction limit of visible light.

We thought quantum dots could be the basis for an experiment to complement the ones presented in chapter 3. Figure 5.1 shows the basic outline of such an experiment. Inside a chip similar to the ones used in chapter 3, a liquid viscosity gradient is established and quantum dots are added. A microscope is used to track the motion of the dots. By analyzing the trajectories of these particles, it is possible to pick out any drift. We decided to attempt such an experiment.

An optical experiment has several appealing features. First, by measuring the diffusivity and drift speeds of particles at different points in the mixing channel, we can measure $D(x)$. Because of the connection between $D(x)$ and $\eta(x)$, this will allow us to check the accuracy of our model for $\eta(x)$, equation 3.26. Second, it allows us to directly measure $\langle \dot{x} \rangle$ without a model connecting drift speed to ionic current. Seeing is believing; directly observing the action inside the mixing channel can be more convincing than an electrical measurement.

5.2 Feasibility of measuring the drift of quantum dots driven by a viscosity gradient

Quantum dots are promising tools, but they present several challenges. Their small size means that they are not as bright as other fluorescing particles like DNA [67]. Discerning them from noise can be difficult. Further, they diffuse rapidly, meaning that longer exposures spread their light over more pixels. The high diffusivity that makes them appealing as tools to measure viscosity-driven motion also means that they readily diffuse out of the focal plane or *drop-out* [67]. They also intermittently *blink*, and stop emitting photons for a period of time [67]. Overall, it can be difficult to obtain long and accurate particle trajectories.

5.2.1 Drift speed compared to diffusion

The drift speed of a quantum dot with radius $r = 10$ nm should be appreciable. Assuming this quantum dot is diffusing in a 200 μm long mixing channel with $\eta_L = 2$ mPa s and $\eta_R = 6$ mPa s,

$$\langle \dot{x} \rangle = \frac{dD}{dx} \approx \frac{k_B T}{6\pi r L} \left(\frac{1}{\eta_L} - \frac{1}{\eta_R} \right), \quad (5.1)$$

suggests a drift speed of about 35 nm s^{-1} . For commonly used optical microscopes, this would result in the dot drifting by one pixel every few seconds.

However, while the particle is drifting, it is also diffusing. For the drift to be easily detectable, it should be at least of the same magnitude as the random motion. We expect the particle to diffuse according to,

$$\langle x^2 \rangle = 4D\Delta t. \quad (5.2)$$

Since the random motion scales with $\sqrt{\Delta t}$ and the drift scales with Δt , we expect random motion to dominate at short timescales and drift to dominate at long timescales. The magnitudes of the random motion and the drift are approximately equal when,

$$4D\Delta t = \langle \dot{x} \rangle^2 \Delta t^2. \quad (5.3)$$

A particle like the one described above diffusing in a liquid with viscosity 4 mPa s (four times that of water) has a diffusivity of $5.3 \times 10^{-12} \text{ m}^2 \text{ s}^{-1}$. Solving for Δt gives about 8500 s. This is a long

time, but by accumulating statistics over multiple molecules, it may be possible to detect the drift of these particles.

5.2.2 Number of photons expected at the CCD from a single quantum dot

Assuming a decay rate of $\gamma = 10$ ns from the excited state, an ideal single quantum dot can emit 10^8 photons per second under perfect illumination [67, 69]. With 100 ms exposure, we have 10^7 photons to work within each frame for a single dot.

A typical imaging system using a 100×1.49 NA oil immersion objective can collect light that is off of the optical axis by an angle [70],

$$\theta = \sin^{-1} \left(\frac{\text{NA}}{n} \right). \quad (5.4)$$

Using immersion oil with a refractive index of 1.52, we get $\theta = 78.6^\circ$. This corresponds to a solid angle of $SA = 4\pi \sin^2 \theta = 5.05$, or about 40% of the unit sphere. If the dot emits photons isotropically, we can collect 40% of the photons emitted.

These photons are not all focused onto a single pixel. Using equation 5.3, and the diffusivity mentioned above, we expect a diffusing dot to be localized to about $1 \mu\text{m}^2$ in one 100 ms frame. For a typical imaging system, this could mean about 40 pixels. Collecting these terms, an estimate of the number of photons per pixel per frame is,

$$n = \gamma^{-1} \Delta t \frac{SA}{4\pi} N_{\text{pixels}}, \quad (5.5)$$

where Δt is the exposure time. This means an ideal signal of about 10^5 photons hitting each pixel in each frame. This neglects imperfect illumination, sources of photon loss like reflections, the efficiency of the CCD to convert photons into charge and measure it, the quantum efficiency of the dots, and blinking, among other things. Overall, we found the detectability of the dots to be a problem.

5.2.3 Drop-out and blinking

Two factors that can make quantum dots hard to track are drop-out and blinking [67]. Drop-out refers to when a particle moves normal to the focal plane, goes out of focus, and becomes impossible

to detect. For diffusing particles, this can be especially problematic because the motion cannot be predicted. The *depth of field*, the distance about the focal plane of an optical system in which an object remains in focus, is critical because it says roughly how far a particle can diffuse without becoming untrackable. The depth of field of a microscope objective can be approximated,

$$DOF = \frac{\lambda n}{NA^2} + \frac{n}{M \times NA} e, \quad (5.6)$$

where λ is the wavelength of light, NA is the numerical aperture of the objective, n is the index of refraction of the immersion medium, and e is the size of the smallest feature resolvable with the detector [67]. For a typical microscope used in tracking small fluorescent particles, the two terms in equation 5.6 are comparable and the depth of field is about 500 nm.

We expect a typical quantum dot diffusing in free space to remain within two depths of field for about 100 ms on average. Imaging quantum dots inside a microchannel thinner than the depth of field, however, would force dots to remain in focus and eliminate this problem.

Quantum dots are also known to *blink*, or cease fluorescing for an unpredictable period of time lasting milliseconds to hundreds of seconds [71]. The mechanism for blinking is complicated, but the effect is an added challenge for tracking. One silver lining is that blinking can be useful for differentiating individual dots from aggregates, as a large group of uncorrelated dots will rarely blink at the same time [67].

5.3 Experimental methods

We used a Nikon inverted microscope with a $60\times$ 1.2 NA water immersion objective. Connected to the microscope was an Andor iXon 978 CCD camera and a 120 W EXFO X-Cite 120 UV illumination source. The width of the 512×512 CCD was 8.2 mm, and the depth of field was about $0.5 \mu\text{m}$. We generally used an exposure time of 100 ms.

The chips we used in the electrokinetic chip experiments outlined in chapter 3 were very similar to (and in fact based on) chips used for fluorescent DNA experiments [66]. They are designed to mount on a microscope and have particles inside excited by UV light. This made it relatively simple to convert our electrokinetic experiment into an optical particle tracking one.

We used CdSe quantum dots (Ocean Nanotech QSH-525) which were carboxyl functionalized

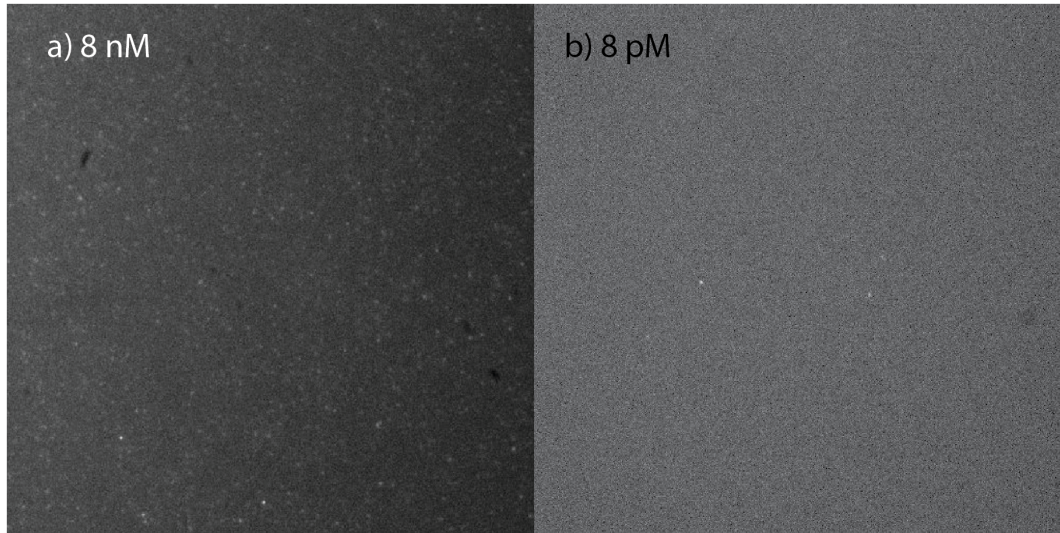


Figure 5.2: Quantum dots in a droplet of water. a) 8 nM, b) 8 pM.

and had fluorescence peaks at 525 nm. Including the acidic shell, these dots had a radius of about 10 nm. We prepared solutions ranging from the picomolar to nanomolar range. We introduced KCl and tris buffer to control the screening length of surfaces and the pH of the solutions. To minimize the problem of quantum dot aggregation, we generally made solutions with pH in the range of 8. At this pH, many of the carboxyl groups on the surfaces of the dots should have been deprotonated, leaving the dots negatively charged. In theory, this caused mutual repulsion among the particles. In practice, we still saw evidence of aggregation.

Using this setup to image a solution of quantum dots, it was possible to distinguish bright objects from the background. Figure 5.2 shows typical images of quantum dots in droplets of water. However, we questioned whether these objects were individual quantum dots or aggregates for two main reasons. First, the number density was lower than expected. Second, the diffusivity was less than expected. The next two sections will outline these observations.

5.4 Number density

Most obvious, the number density of the objects seemed too low. We expected the number of visible dots to be roughly,

$$N_{\text{apparent}} = \frac{n \times DOF \times w_{\text{CCD}}^2}{\text{mag}^2} \quad (5.7)$$

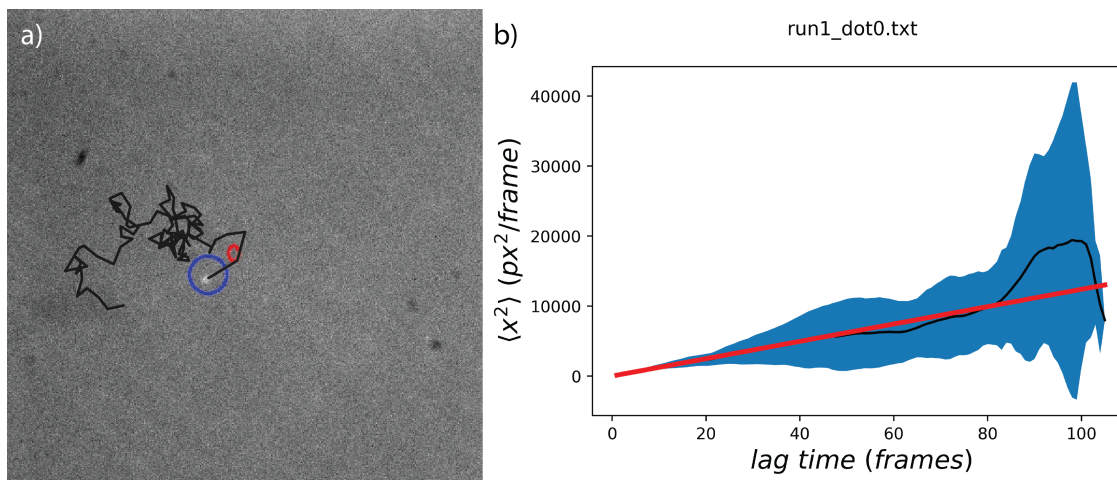


Figure 5.3: a) A frame of video with a single quantum dot identified and circled. Red line shows the particle's trajectory. b) The mean squared displacement as a function of lag time. Red line shows a power law fit.

where n is the number density of particles in the bulk solution, DOF is the depth of field of the imaging system, w_{CCD} is the width of the CCD, and mag is the magnification. For a 10 pM solution of quantum dots, we expected to see about 500 dots. In a situation like this, we would routinely see less than 50. Figure 5.2b shows 8 pM quantum dots. Less than 10 are clearly visible.

5.5 Tracking quantum dots and measuring diffusivity

Another clue that the objects we were resolving were quantum dot aggregates came when we tracked the particles' trajectories and obtained diffusivities which seemed too low. We used two independent methods to track quantum dots in images and calculate diffusivities. The first, we wrote ourselves. It relied on OpenCV, a computer image analysis toolbox for Python [72]. We subtracted the average brightness of all pixels in the video from each pixel to eliminate background, and we applied a Gaussian blur with a width of five pixels to decrease noise. Then, we applied a threshold to find bright objects in the image. To start, a user clicks on the location of a bright object in a frame. In each subsequent frame, the positions of pixels that pass a brightness threshold and were close to a bright object in the previous frame were recorded.

The second method used TrackPy [73], a particle tracking software package for Python. Both methods produced similar results, but we found TrackPy was more reliable and easier to use. Both systems produced a list of each particle's position in each frame.

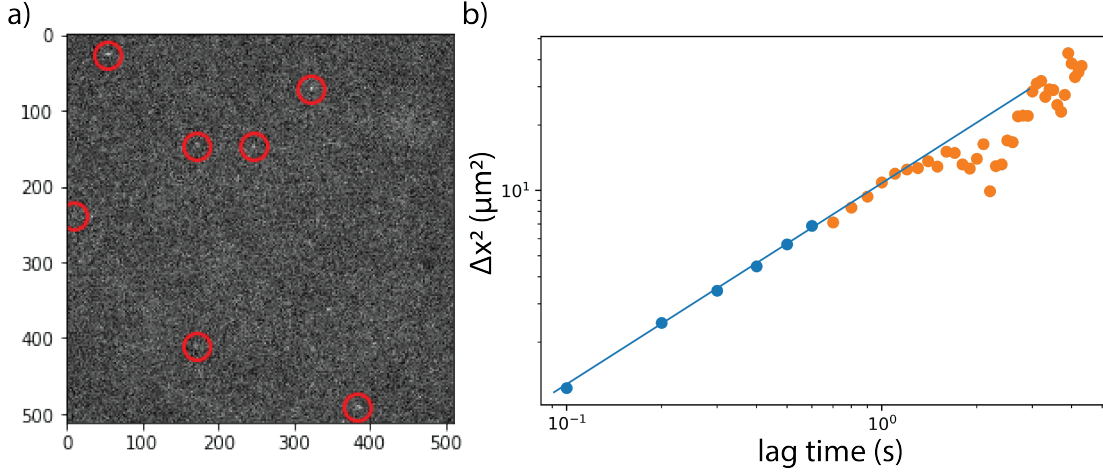


Figure 5.4: a) A frame of video with quantum dots identified and circled. b) The ensemble mean squared displacement as a function of lag time. The blue line shows is a power law fit. Points in blue are included in the fit.

5.5.1 Measuring quantum dot diffusivity by tracking individual particles

With the trajectory of an individual dot, it is straightforward to find the diffusivity. In two dimensions, the expected mean squared displacement of a random walker is proportional to the time [21],

$$\langle x^2 \rangle = 4Dt. \quad (5.8)$$

We calculated the mean squared displacement as a function of time using,

$$\langle \Delta x^2 \rangle_l = \frac{1}{N} \sum_{i=0}^N (x_{il} - x_{i0})^2, \quad (5.9)$$

where N is the number of particles, l is the lag time or the length of time over which the squared displacements are measured. This is a naive approach which does not use the available data optimally because each particle trajectory actually contains many shorter subtrajectories. Therefore, using the same data, we can get better statistics for mean squared displacement of lag time l by averaging the squared displacements of all subtrajectories of length l ,

$$\langle \Delta x^2 \rangle_l = \frac{1}{N} \sum_{i=0}^N \frac{1}{M-l} \sum_{j=0}^{M-l} (x_{i(l+j)} - x_{ij})^2. \quad (5.10)$$

Here, j is the offset of the subtrajectory from the full trajectory, and M is the number of steps in the full trajectories. Allowing for trajectories of different lengths requires a small change,

$$\langle \Delta x^2 \rangle_l = \frac{1}{N_{M_i \geq l}} \sum_{i=0}^N \frac{1}{M_i - l} \sum_{j=0}^{M_i - l} (x_{i(l+j)} - x_{ij})^2, \quad (5.11)$$

where M_i is now the number of steps in trajectory i and $N_{M_i \geq l}$ is the number of trajectories with lengths longer than l .

Figure 5.3a shows the trajectory of a single quantum dot tracked by our software. The path shows no obvious systematic drift over time. Figure 5.3b shows the mean squared displacement of the particle as a function of the lag time, with a linear fit. The width of the blue region shows the standard error whose width increases with lag time as the number of independent subtrajectories decreases. The mean squared displacement increases linearly, as expected. The slope of the fitted line suggests an effective radius of 27.4 nm.

Figure 5.4a shows several dots identified by the TrackPy software. Figure 5.4b shows the ensemble mean squared displacement of the dots as a function of the lag time, again with a linear fit. The slope of the fitted line suggests an effective radius of 27.1 nm.

The two particle tracking methods produced similar results. Both show particle radii nearly three times larger than expected. This suggests that all or many of the particles we observed were aggregates composed of approximately nine quantum dots.

5.5.2 Measuring ensemble quantum dot diffusivity

In another experiment, we observed quantum dots near the mouth of the 50 nm tall mixing channel using 8 nM dots in water with only 10 mM tris buffer and no other added electrolyte. When we applied pressure to direct fluid flow through the mixing channel, the flow trapped the dots against the mouth of the channel in a sharply peaked distribution, instead of pushing them into the channel. Figure 5.5a shows the dots trapped against the edge of the mixing channel.

Once the flow was turned off, the dots would diffuse freely and the distribution would relax away from the edge, widening with time. Figures 5.5b and c show the state of the quantum dots after 10 and 40 frames.

Electrostatic repulsion explains why the dots did not enter the channel. At with low salinity, the Debye length (described in section 2.4.2) was large. A 10 mM solution of KCl has a Debye

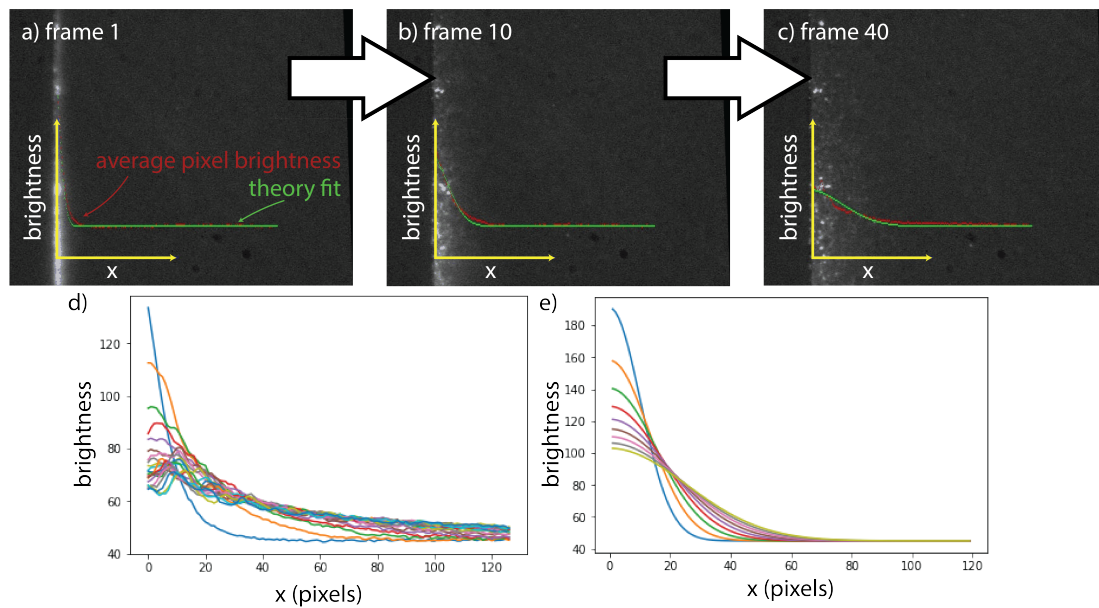


Figure 5.5: Frames from a video of fluorescing quantum dots in a glass chip. Before frame 1, a fluid flow pressed the dots against an electrostatic boundary at $x = 0$ a) The fluid flow is turned off and the dots can freely diffuse. They start in a sharply peaked distribution at $x = 0$. The red line shows the average pixel brightness. The green line shows equation 5.12 b) and c) The dots relax into a wider distribution. d) The brightness as a function of position for several different frames. e) The brightness as a function of position predicted by equation 5.12.

length of about 3 nm [21]. Since tris is a weak acid which does not fully dissociate in water, the ion concentration would have been lower than for the equivalent concentration of KCl, and the Debye length would have been longer than 3 nm. With the positively charged glass surfaces ineffectively screened, the like-charged quantum dots were electrostatically excluded from the mixing channel.

To analyze this video quantitatively, we used OpenCV again. The red lines overlaid on the microscope images in figure 5.5 show the pixel brightnesses, averaged by column. Figure 5.5d shows the brightness data for several frames. After subtracting the average background brightness from each pixel, we used the average column brightness as an analog for fluorescent particle density as a function of x . We analyzed each frame of the video in this way.

Particles diffusing from an initial sharply peaked distribution is the same as the system we simulated in section 4.1.1. Accordingly, we will fit this two dimensional data with an equation similar to equation 4.5,

$$b(x, t) = \frac{N}{\sqrt{4\pi D(t - t_0)}} e^{-(x-x_0)^2/4D(t-t_0)} + bg. \quad (5.12)$$

Here, N is a fitting parameter representing the total number of particles, t_0 and x_0 are fitting parameters representing offsets in position and time, and bg is a manually set parameter that represents the background brightness far from the edge of the mixing channel. The final fitting parameter, D , is the one we care about. The green lines in figure 5.5 show the results of the fit, $D = 11.7 \mu\text{m}^2 \text{s}^{-1}$. Based on the Stokes-Einstein equation, this corresponds to an average particle radius of 20 nm. Figure 5.5e shows the results of the fit for several frames. This is larger than the 10 nm from the product specification. However, in the video there are clearly larger clumps which are being averaged into this measurement. These would drag the average up.

5.6 Conclusion

The above calculations reveal that the radii of the particles we have been able to resolve are about three times greater than expected. This suggests that the particles we were observing were aggregates of multiple quantum dots. Returning to the calculations of section 5.2.1, tripling the radius of the particles triples the time scale at which drift overcomes diffusion. The expected time needed to measure the drift reaches 25 000 s or nearly seven hours. This measurement would require a lot of

data. Finding a way to avoid quantum dot aggregation is important.

A bigger problem was the overall difficulty of consistently producing videos with trackable quantum dots. We have presented results here that featured some individually resolved fluorescing particles, but these were not the norm. In practice we were able to resolve clear individual objects in our fluidic chips only intermittently. We believe this problem could be partly mitigated with an imaging system specifically built to track quantum dots. Objectives are available with higher magnification and higher numerical apertures than the ones we used. We will continue to work on these experiments.

Chapter 6

Conclusion

We have examined diffusion in a gradient of liquid viscosity from several different angles. First, we discussed some background and historical context. We reviewed existing experiments in the area. These experiments have significant drawbacks and come to conflicting conclusions. We also discussed some simulation work which, with slight twists on the basic model, produced different results, demonstrating the need for a solid experiment. These simulations led us to design our own experiments.

We developed some theoretical and experimental background and described an early experiment in which we used pulled glass nanocapillaries to attempt to electronically measure current driven by a viscosity gradient. This experiment's flaws led us to design a new experiment inside a purpose built nanofluidic chip. We described the methods of this nanochannel-based electrokinetic experiment, and analyzed the data, finding good agreement with a simple model. In summary, we showed evidence that counterions screening the glass surfaces drifted toward lower viscosity, resulting in an ionic current. This experiment gave us fine control over viscosity profile, allowing us to vary its parameters in a way never possible before. We also analyzed alternate explanations for the currents we measured, and concluded that they cannot explain our results.

We used a simulation to help explain the mechanisms behind drifting particles and flux and explore the problem with access to properties only reachable in a computer. The boundary conditions of our simulation turned out to be fundamentally important. Boundary conditions designed to simulate electrodes produced qualitatively similar results to our experiments.

Finally, we outlined an ongoing experiment using optical particle tracking in place of electronic

current detection. We explore the merits of this experiment, and explained why it has not worked so far.

Viscosity gradients can be seen as a new tool to drive transport for a variety of purposes in nanofluidics and membrane technology. It could also have unappreciated effects in other contexts. For example, viscosity gradients can drive motion within and between cells, where viscosities are known to vary by orders of magnitude [38]. It may also have effects in geology, causing significant changes in the distributions of hydrocarbons, sediments, or other small particles to build up over extremely long timescales. Our work also has important implications for computer simulations of biological, chemical, or other liquid systems, where spatially-varying viscosities naturally arise. In these, a position on the Itô-Stratonovich dilemma must (consciously or unconsciously) be taken, and there was previously no experimental guidance.

Bibliography

- [1] Restriction digest map. <http://www.nslc.wustl.edu/courses/bio2960/labs/07DNA/Restriction/index.html>. Accessed: 2018-12-25.
- [2] Angell, J. B., Jerman, J., Terry, S. & Saadat, S. A prototype gas analysis system using a miniature gas chromatograph. *NASA STI/Recon Technical Report N* **81** (1981).
- [3] Lançon, P., Batrouni, G., Lobry, L. & Ostrowsky, N. Drift without flux: Brownian walker with a space-dependent diffusion coefficient. *EPL (Europhysics Letters)* **54**, 28 (2001).
- [4] Van Milligen, B. P., Bons, P., Carreras, B. A. & Sánchez, R. On the applicability of fick's law to diffusion in inhomogeneous systems. *European journal of physics* **26**, 913 (2005).
- [5] Volpe, G. & Wehr, J. Effective drifts in dynamical systems with multiplicative noise: a review of recent progress. *Reports on Progress in Physics* **79**, 053901 (2016).
- [6] Reuss, F. F. Sur un nouvel effet de l'électricité galvanique. *Mem. Soc. Imp. Natur. Moscou* **2**, 327–337 (1809).
- [7] Wall, S. The history of electrokinetic phenomena. *Current Opinion in Colloid & Interface Science* **15**, 119–124 (2010).
- [8] Quincke, G. Ueber eine neue art elektrischer ströme. *Ann. Phys. Chem* **107**, 1–47 (1859).
- [9] Saxén, U. Ueber die reciprocität der electrischen endosmose und der strömungsströme. *Annalen der Physik* **283**, 46–68 (1892).
- [10] Onsager, L. Reciprocal relations in irreversible processes. i. *Physical review* **37**, 405 (1931).
- [11] Laylin, J. K. *Nobel laureates in chemistry, 1901-1992* (Chemical Heritage Foundation, 1993).

- [12] Derjaguin, B., Sidorenkov, G., Zubashchenkov, E. & Kiseleva, E. Kinetic phenomena in boundary films of liquids. *Kolloidn. zh* **9**, 335–347 (1947).
- [13] Duhr, S. & Braun, D. Why molecules move along a temperature gradient. *Proceedings of the National Academy of Sciences* **103**, 19678–19682 (2006).
- [14] Berg, J. M., Tymoczko, J. L., Stryer, L. & Clarke, N. D. Biochemistry. 2002. *New York, New York* **10010** (2002).
- [15] Feynmann, R. P. Plenty of room at the bottom. *Vortrag am California Institute of Technology* (1959).
- [16] Tabeling, P. *Introduction to microfluidics* (Oxford University Press on Demand, 2005).
- [17] Whitesides, G. M. The origins and the future of microfluidics. *Nature* **442**, 368 (2006).
- [18] Morrison Jr, F. & Osterle, J. Electrokinetic energy conversion in ultrafine capillaries. *The Journal of Chemical Physics* **43**, 2111–2115 (1965).
- [19] Bocquet, L. & Charlaix, E. Nanofluidics, from bulk to interfaces. *Chemical Society Reviews* **39**, 1073–1095 (2010).
- [20] Feynman, R. P., Leighton, R. B. & Sands, M. *The Feynman lectures on physics, Vol. I: The new millennium edition: mainly mechanics, radiation, and heat*, vol. 1 (Basic books, 2011).
- [21] Nelson, P. *Biological physics* (WH Freeman New York, 2004).
- [22] Chaudesaigues, M. Le mouvement brownien et la formule d'einstein. *Comptes Rendus* **147**, 1044–1046 (1908).
- [23] Perrin, J. Mouvement brownien et réalité moléculaire. In *Annales de Chimie et de Physique*, vol. 18, 5–104 (1909).
- [24] Einstein, A. On the motion of small particles suspended in liquids at rest required by the molecular-kinetic theory of heat. *Annalen der physik* **17**, 549–560 (1905).
- [25] Von Smoluchowski, M. Zur kinetischen theorie der brownschen molekularbewegung und der suspensionen. *Annalen der physik* **326**, 756–780 (1906).

- [26] Jarrow, R., Protter, P. *et al.* A short history of stochastic integration and mathematical finance: The early years, 1880–1970. In *A festschrift for Herman Rubin*, 75–91 (Institute of Mathematical Statistics, 2004).
- [27] Lalley, S. Lecture notes on mathematical finance (2001).
- [28] Chung, K. L. *Elementary probability theory with stochastic processes* (Springer Science & Business Media, 2012).
- [29] Embrechts, P. & Maejima, M. An introduction to the theory of self-similar stochastic processes. *International Journal of Modern Physics B* **14**, 1399–1420 (2000).
- [30] Itô, K. Stochastic integral. *Proceedings of the Imperial Academy* **20**, 519–524 (1944).
- [31] de Haan, H. W., Chubynsky, M. V. & Slater, G. W. Monte carlo approaches for simulating a particle at a diffusivity interface and the” ito–stratonovich dilemma”. *arXiv preprint arXiv:1208.5081* (2012).
- [32] Van Kampen, N. G. & Reinhardt, W. P. Stochastic processes in physics and chemistry (1983).
- [33] Dufresne, E. R., Altman, D. & Grier, D. G. Brownian dynamics of a sphere between parallel walls. *EPL (Europhysics Letters)* **53**, 264 (2001).
- [34] Kätelhön, E., Sokolov, S. V. & Compton, R. G. Near-wall hindered diffusion: Implications for surface-based sensors. *Sensors and Actuators B: Chemical* **234**, 420–425 (2016).
- [35] Happel, J. & Brenner, H. *Low Reynolds number hydrodynamics: with special applications to particulate media*, vol. 1 (Springer Science & Business Media, 2012).
- [36] Volpe, G., Helden, L., Brettschneider, T., Wehr, J. & Bechinger, C. Influence of noise on force measurements. *Physical review letters* **104**, 170602 (2010).
- [37] Bławdziewicz, J. & Bhattacharya, S. Comment on “drift without flux: Brownian walker with a space-dependent diffusion coefficient” by p. lançon et al. *EPL (Europhysics Letters)* **63**, 789 (2003).
- [38] de Haan, H. W. & Slater, G. W. Translocation of a polymer through a nanopore across a viscosity gradient. *Physical Review E* **87**, 042604 (2013).

- [39] Uhlenbeck, G. E. & Ornstein, L. S. On the theory of the brownian motion. *Physical review* **36**, 823 (1930).
- [40] Lau, A. W. & Lubensky, T. C. State-dependent diffusion: Thermodynamic consistency and its path integral formulation. *Physical Review E* **76**, 011123 (2007).
- [41] Hanggi, P. Nonlinear fluctuations: The problem of deterministic limit and reconstruction of stochastic dynamics. *Physical Review A* **25**, 1130 (1982).
- [42] Klimontovich, Y. L. Ito, stratonovich and kinetic forms of stochastic equations. *Physica A: Statistical Mechanics and its Applications* **163**, 515–532 (1990).
- [43] Van Kampen, N. Diffusion in inhomogeneous media. *Journal of physics and chemistry of solids* **49**, 673–677 (1988).
- [44] Kundu, P. & Cohen, L. Fluid mechanics, 638 pp. *Academic, Calif* (1990).
- [45] Wiener, B. Poiseuille flow simulation. <http://www.benwiener.com/physics/poiseuille.html>.
- [46] Behrens, S. H. & Grier, D. G. The charge of glass and silica surfaces. *The Journal of Chemical Physics* **115**, 6716–6721 (2001).
- [47] Stokes, G. G. *On the effect of the internal friction of fluids on the motion of pendulums*, vol. 9 (Pitt Press Cambridge, 1851).
- [48] Hunter, R. J. *Foundations of colloid science* (Oxford university press, 2001).
- [49] Wiener, B. Streaming current simulation. <http://www.benwiener.com/physics/poiseuille.html>.
- [50] Cervera, J., Schiedt, B., Neumann, R., Mafé, S. & Ramírez, P. Ionic conduction, rectification, and selectivity in single conical nanopores. *The Journal of chemical physics* **124**, 104706 (2006).
- [51] Anderson, J. L. Colloid transport by interfacial forces. *Annual review of fluid mechanics* **21**, 61–99 (1989).
- [52] Prieve, D. C. Migration of a colloidal particle in a gradient of electrolyte concentration. *Advances in Colloid and Interface Science* **16**, 321–335 (1982).

- [53] Haynes, W. M. Crc handbook of chemistry and physics (2016).
- [54] Stein, D., Kruithof, M. & Dekker, C. Surface-charge-governed ion transport in nanofluidic channels. *Physical Review Letters* **93**, 035901 (2004).
- [55] Tang, J. X. Measurements of fluid viscosity using a miniature ball drop device. *Review of Scientific Instruments* **87**, 054301 (2016).
- [56] Vignes, A. Diffusion in binary solutions. variation of diffusion coefficient with composition. *Industrial & Engineering Chemistry Fundamentals* **5**, 189–199 (1966).
- [57] Rehfeldt, S. & Stichlmair, J. Measurement and calculation of multicomponent diffusion coefficients in liquids. *Fluid phase equilibria* **256**, 99–104 (2007).
- [58] Lançon, P., Batrouni, G., Lobry, L. & Ostrowsky, N. Brownian walker in a confined geometry leading to a space-dependent diffusion coefficient. *Physica A: Statistical Mechanics and its Applications* **304**, 65–76 (2002).
- [59] Sokolov, I. Ito, stratonovich, hänggi and all the rest: The thermodynamics of interpretation. *Chemical Physics* **375**, 359–363 (2010).
- [60] Seidell, A. *et al. Solubilities of inorganic and organic compounds* (van Nostrand, 1952).
- [61] Burgess, J. *Metal ions in solution* (1978).
- [62] Peskin, C. S., Odell, G. M. & Oster, G. F. Cellular motions and thermal fluctuations: the brownian ratchet. *Biophysical journal* **65**, 316–324 (1993).
- [63] Kuimova, M. K., Yahioglu, G., Levitt, J. A. & Suhling, K. Molecular rotor measures viscosity of live cells via fluorescence lifetime imaging. *Journal of the American Chemical Society* **130**, 6672–6673 (2008).
- [64] Rehfeldt, S. & Stichlmair, J. Measurement and prediction of multicomponent diffusion coefficients in four ternary liquid systems. *Fluid Phase Equilibria* **290**, 1–14 (2010).
- [65] Guasto, J. S., Huang, P. & Breuer, K. S. Statistical particle tracking velocimetry using molecular and quantum dot tracer particles. *Experiments in fluids* **41**, 869–880 (2006).

- [66] Kim, D., Bowman, C., Del Bonis-O'Donnell, J. T., Matzavinos, A. & Stein, D. Giant acceleration of dna diffusion in an array of entropic barriers. *Physical Review Letters* **118**, 048002 (2017).
- [67] Guasto, J. S. *Micro-and nano-scale colloidal dynamics near surfaces*. Ph.D. thesis, Citeseer (2008).
- [68] Ernst, D. & Köhler, J. Measuring a diffusion coefficient by single-particle tracking: statistical analysis of experimental mean squared displacement curves. *Physical Chemistry Chemical Physics* **15**, 845–849 (2013).
- [69] Stobbe, S., Johansen, J., Kristensen, P. T., Hvam, J. M. & Lodahl, P. Frequency dependence of the radiative decay rate of excitons in self-assembled quantum dots: Experiment and theory. *Physical Review B* **80**, 155307 (2009).
- [70] Moore, J. H., Davis, C. C., Coplan, M. A. & Greer, S. C. *Building scientific apparatus* (Cambridge University Press, 2009).
- [71] Shimizu, K. T. *et al.* Blinking statistics in single semiconductor nanocrystal quantum dots. *Physical Review B* **63**, 205316 (2001).
- [72] Bradski, G. The OpenCV Library. *Dr. Dobb's Journal of Software Tools* (2000).
- [73] Allan, D., Caswell, T., Keim, N. & van der Wel, C. trackpy: Trackpy v0.3.2 (2016).